Table of contents

Supplementary Note 1: Introduction: performance of synthetic fuels regarding the four key challenges.2
Supplementary Note 2: Introduction: recent assessments of Fischer-Tropsch fuels.....3
Supplementary Note 3: Fuel production: model 4
Supplementary Note 4: Fuel production: process flowsheets 9
Supplementary Note 5: Fuel production: fuel composition.....12
Supplementary Note 6: Fuel usage: fuel standards.....13
Supplementary Note 7: Fuel usage: fuel properties.....14
Supplementary Note 8: Fuel usage: material compatibility 16
Supplementary Note 9: Fuel usage: numerical results of fuel properties and material compatibility 18
Supplementary Note 10: Fuel usage: combustion emissions 19
Supplementary Note 11: Fuel usage: numerical results of combustion emissions.....21
Supplementary Note 12: Life cycle assessment (LCA).....23
Supplementary Note 13: LCA: used technologies of supply chain designs 26
Supplementary Note 14: LCA: carbon footprint minimization 27
Supplementary Note 15: LCA: carbon footprint minimization with limited inputs.....28
Supplementary Note 16: LCA: environmental impacts beyond carbon footprint 29
Supplementary Note 17: LCA: biomass consumption 30
Supplementary Note 18: LCA: contribution analysis of HyFiT-20%, electricity from wind power.....32
Supplementary Note 19: LCA: contribution analysis of HyFiT-20%, electricity from the grid.....34
Supplementary Note 20: LCA: contribution analysis of HyFiT-40%, electricity from wind power.....36
Supplementary Note 21: LCA: contribution analysis of HyFiT-40%, electricity from the grid.....38
Supplementary Note 22: LCA: sensitivity analysis of battery-electric van.....40
Supplementary Note 23: LCA: sensitivity analysis of land-use change emissions 43
Supplementary Note 24: LCA: sensitivity analysis of the removal of aromatics and oxygenates 44
Supplementary Note 25: Key performance indicator: carbon efficiency.....49
Supplementary Note 26: Key performance indicator: conversion, selectivity, and yield.....50
Supplementary references.....51

Supplementary Note 1: Introduction: performance of synthetic fuels regarding the four key challenges

In literature, technological maturity is commonly expressed in terms of technology readiness level (TRL) ranging from one to nine, with nine representing the most mature technology.[1]

While the technological maturity of dimethyl ether (DME) production via methanol is high with a TRL of nine,[2,3] DME's TRL is estimated as four in case of direct synthesis via H_2 and carbon dioxide (CO_2).[4] Polyoxymethylene ethers (OMEs) of chain length one (OME_1) and three to five (OME_{3-5}) have estimated TRLs of four to five[2,3,5] and three to five,[2,3,6] respectively. Both DME and OMEs have shown to burn almost without particulate matter (PM) formation which can be leveraged to also reduce nitrogen oxides (NO_x) emissions.[7–11] Well-to-wheel greenhouse gas (GHG) emissions can be close to net zero if DME and OMEs are produced from CO_2[12–18] or biomass.[19–23] However, DME and OMEs have much lower heating values than diesel, resulting in increased fuel consumption.[24,25] Moreover, these fuels require minor adaptions to today's diesel engine systems. Importantly, all three would need new sealing materials if used as pure substitutes for diesel.[25–27] DME and OME_1 would also require pressurized tanks[9,26] and DME additionally an adapted fuel-injection system.[26]

The common biofuels hydrogenated vegetable oil (HVO) and fatty acid methyl ester (FAME), known as biodiesel, are commercially established technologies with TRLs of nine,[2,28–30] and both are compatible with the existing fuel infrastructure.[29,31] However, FAME application has shown degradation of elastomer materials,[32] and using it as pure fuel requires slight engine modifications to prevent deterioration of engine efficiency.[33] PM and NO_x emissions are reduced with HVO,[31,34–36] whereas measurements are inconclusive for FAME: Some studies report reductions in PM and increases in NO_x emissions,[37–40] but others highlight increases for both pollutants.[41,42] Nonetheless, HVO and FAME have shown to reduce well-to-wheel GHG emissions compared to fossil diesel.[29,43] They can be produced from vegetable oil, e.g., rapeseed, soybean, and palm oil, as well as used cooking oil that stems from vegetable oil or animal fat.[29] However, first-generation biofuels produced from vegetable oil are in the "food versus fuel" conflict,[44] and palm oil is additionally associated with indirect land-use change and deforestation.[45] Both issues render used cooking oil the only suitable feedstock for large-scale production of HVO and FAME, making their production inflexible regarding feedstock choice. Additionally, the sustainability of used cooking oil as a feedstock remains controversial: In the future, the global demand for used cooking oil is expected to exceed its supply by far, which may trigger the displacement of used cooking oil by virgin oil in exporting countries, e.g., palm oil in Southeast Asia.[46]

Supplementary Note 2: Introduction: recent assessments of Fischer-Tropsch fuels

In Supplementary Table 1, we present an overview on recent life cycle assessments (LCAs), techno-economic assessments (TEAs), and reviews for Fischer-Tropsch (FT) fuels for further reading. While most assessments consider either biomass or CO_2 as feedstock, only five studies include both. About twice as many studies focus on road as on aviation applications. Approximately 80% of the studies conduct TEAs and less than 50% perform LCAs.

Supplementary Table 1: Recent literature on life cycle assessments (LCAs), techno-economic assessments (TEAs), and reviews for Fischer-Tropsch fuels. Related to the Introduction.

Author	Year	Feedstock			Application		Assessment		
		Biomass	CO_2	Fossil	Road	Aviation	LCA	TEA	Review
Colelli et al.[47]	2023		X			X		X	
Delgado et al.[48]	2023		X		unspecified		X	X	
Hong et al.[49]	2023		X		unspecified			X	
Jacobsen et al.[50]	2023		X			X		X	
Katiyo et al.[51]	2023	X			X			X	
Okolie et al.[52]	2023	X				X			X
Van den Oever et al.[53]	2023	X			X		X		
Weyand et al.[54]	2023	X	X		unspecified		X	X	
Gao et al.[55]	2022		X		unspecified			X	
Medrano-García et al.[56]	2022		X		X		X	X	
Peters et al.[57]	2022		X		X	X		X	
Gao et al.[58]	2021		X		unspecified			X	
Herz et al.[59]	2021		X		unspecified			X	
Marchese et al.[60]	2021		X		unspecified			X	
Ordóñez et al.[61]	2021		X		X		X	X	
Zang et al.[62]	2021		X		X	X	X		
Zang et al.[63]	2021		X		X	X		X	
Zang et al.[64]	2021		X		X		X	X	
Borugadda et al.[65]	2020	X			X		X	X	
Dieterich et al.[66]	2020	X	X	X	X			X	X
Drünert et al.[67]	2020		X			X		X	
Liu et al.[68]	2020		X		X		X		
Lundberg et al.[69]	2020	X				X	X		
Okeke et al.[70]	2020	X			X		X		
Alhyari et al.[71]	2019		X		X		X		
Cuéllar-Franca et al.[72]	2019		X		X		X	X	
Decker et al.[73]	2019		X		X			X	
Hombach et al.[74]	2019		X		X		X	X	
Navas-Anguita et al.[75]	2019	X			X		X		
Schemme et al.[3]	2019		X		X	X		X	
Tsongidis et al.[76]	2019		X		unspecified			X	
Blanco et al.[77]	2018	X			X	X		X	
Brynolf et al.[78]	2018		X		X			X	X
Dietrich et al.[79]	2018	X	X			X		X	
Dimitriou et al.[80]	2018	X			X	X		X	
Hernandez et al.[81]	2018	X			X			X	
Herz et al.[82]	2018		X		unspecified			X	
Neuling et al.[83]	2018	X				X	X	X	
Samavati et al.[84]	2018	X	X		X		X	X	
Vázquez et al.[85]	2018		X		unspecified				
Zhang et al.[86]	2018	X		X	X	X	X	X	
Albrecht et al.[87]	2017	X	X		X	X		X	
de Jong et al.[88]	2017	X				X	X		
Herz et al.[89]	2017	X			unspecified			X	
Liu et al.[90]	2017	X		X	X		X	X	
Okeke et al.[91]	2017	X			X			X	
Rafati et al.[92]	2017	X			unspecified			X	
Snehesh et al.[93]	2017	X			unspecified			X	
Tsalidis et al.[94]	2017	X			X		X		
Zhou et al.[95]	2017	X		X	X		X	X	
Ail et al.[96]	2016	X			X		X	X	X
König et al.[97]	2015		X		X	X		X	
König et al.[98]	2015		X		unspecified			X	

Supplementary Note 3: Fuel production: model

In the following, we describe our model for HyFiT-fuel production in detail. For the HyFiT-fuel concept, we combine the well-established technologies Fischer-Tropsch (FT) synthesis and hydroformylation and assume a green-field approach, i.e., a facility with at dedicated production site.

Processes simulated in AspenPlus use the non-random two-liquid (NRTL) or Peng-Robinson property model for pressures below or greater 10 bar, respectively. In mass and energy balances, alkanes, olefins, aromatics, and oxygenates (i.e., 1-alkanols) are modeled according to the chemical formulas $C_nH_{2(n+1)}$, C_nH_{2n}, C_nH_n, and $C_nH_{2n+1}OH$. If property data is missing in AspenPlus for a component of certain chain length, we rely on property data of the next shorter chain length for which complete property data is available. If no aromatic compound exists in AspenPlus with the modeled C:H ratio, an aromatic compound with the closest number of hydrogen atoms is considered for the corresponding number of carbon atoms. For all process steps, we assume 20 °C and 1 bar as ambient conditions. Hydrogen and syngas enter the process at ambient temperature and 30 bar, corresponding to their pressure level of supply; both are heated up and compressed or expanded if required for the following process steps. For compressors, we assume isentropic and mechanical efficiencies of 80% and 90%. Pumps are modeled with an efficiency of 80%.

Fischer-Tropsch synthesis. In the FT reactor, CO and hydrogen (syngas) are converted in the presence of a metal catalyst to hydrocarbons of various chain lengths, i.e., alkanes, olefins, with small amounts of aromatics and oxygenates as side products. The product of FT synthesis is commonly referred to as so-called syncrude in analogy to the similar composition of crude oil in petrochemical refineries. In literature, FT synthesis is usually divided into low-temperature (LT) and high-temperature (HT) FT synthesis, depending on the reaction temperature. LT-FT synthesis uses cobalt-based catalysts which yield a syncrude of mostly long-chain alkanes, only few oxygenates, and almost no aromatics. Iron-based catalysts are usually used for HT-FT synthesis and are less hydrogenation-active compared to cobalt-based catalysts. Thus, the syncrude of HT-FT synthesis contains much more short-chain olefins in addition to alkanes. We model the inputs (syngas), outputs (syncrude, unconverted syngas, CO_2, water), and heat releases of a HT-FT and LT-FT synthesis. Syncrude compositions are modelled with the commonly used Anderson-Schulz-Flory (ASF) distribution.[99] According to the ASF distribution, the mole fraction x_n of syncrude compounds containing n carbon atoms is a function of the chain growth probability α:

$$x_n = (1-\alpha)\cdot\alpha^{n-1}. \quad (S1)$$

The chain growth probability α can be determined experimentally for a given reactor setup and is influenced by several factors such as reactor operation conditions, catalyst, and H_2:CO ratio of the syngas. Typical α-values are in the range of $0.70 < \alpha < 0.75$ for HT-FT synthesis and $0.85 < \alpha < 0.95$ for LT-FT synthesis,[100] with single-pass CO conversions of 80-90% and 40-60%, respectively.[101] In our model, we select an α-value of 0.74 and a CO conversion of 88% for the HT-FT synthesis, as reported by Tu et al. for an iron-based catalyst.[102] Tu et al. mention a selectivity towards undesired CO_2 of 35%, reaction conditions of 280 °C and 20 bar, and an H_2:CO ratio of 1:1. For the LT-FT synthesis, we choose the cobalt-based catalyst with an α-value of 0.88 and CO conversion of 57% by Tsubaki et al.[103] The authors report a selectivity towards undesired CO_2 of 2%, reaction conditions of 240 °C and 10 bar, and an H_2:CO ratio of 2:1.

Next, we subdivide the modeled syncrude distribution of the LT-FT and HT-FT synthesis into the compound classes alkanes, olefins, aromatics, and oxygenates. For this purpose, we apply the typical generic syncrude compositions of cobalt-based LT-FT and iron-based HT-FT synthesis reported by de Klerk (Supplementary Table 2 and Supplementary Figure 1).[99] Note that we only consider hydrocarbons up to a chain length of 40 carbon atoms. We further model all oxygenates as 1-alkanols since 1-alkanols represent the largest fraction of oxygenated compounds in the syncrude.[104] Consequently, we do not consider other oxygenated compounds such as aldehydes, ketones, and carboxylic acids. The resulting syncrude compositions are presented in Supplementary Figure 1. Note that discontinuities in the shown syncrude compositions, e.g., between chain length four and five, result from the generic syncrude compositions of de Klerk that cluster product fractions into discrete carbon ranges (Supplementary Table 2). In reality, syncrude compositions can be expected to be more continuous. Subsequently, we calculate the amount of water-gas shift compounds, i.e., CO, H_2, CO_2, and H_2O, which are present in both reactor outlet streams besides the syncrude. For the calculation, we use the modeled syncrude compositions and reported CO conversions and CO_2 selectivities.

The FT synthesis is highly exothermic, releasing large amounts of excess heat.[100] This excess heat can be used for heat integration or has to be cooled if heat integration is not possible. We calculate the heat release of both FT syntheses as enthalpy difference over the reactor at 280 °C and 20 bar for HT-FT synthesis as well as 240 °C and 10 bar for LT-FT synthesis with isothermal RYield reactor models in AspenPlus v11.

Supplementary Table 2: Generic syncrude compositions of iron-based high-temperature FT (Fe HT-FT) and cobalt-based low-temperature FT (Co LT-FT) syntheses, adopted from de Klerk.[99]

Product fraction	Carbon range	Compound class	Syncrude composition [a] wt%	
			Fe HT-FT	Co LT-FT
Tail gas	C_1	Alkane	12.7	5.6
	C_2	Olefin	5.6	0.1
		Alkane	4.5	1.0
LPG	C_3-C_4	Olefin	21.2	3.4
		Alkane	3.0	1.8
Naphtha	C_5-C_{10}	Olefin	25.8	7.8
		Alkane	4.3	12.0
		Aromatic	1.7	0.0
		Oxygenate	1.6	0.2
Distillate	C_{11}-C_{22}	Olefin	4.8	1.1
		Alkane	0.9	20.8
		Aromatic	0.8	0.0
		Oxygenate	0.5	0.0
Residue/wax	C_{22+}	Olefin	1.6	0.0
		Alkane	0.4	44.6
		Aromatic	0.7	0.0
		Oxygenate	0.2	0.0
Aqueous product	C_1-C_5	Alcohol	4.5	1.4
		Carbonyl	3.9	0.0
		Carboxylic acid	1.3	0.2

[a] Excluding inert gases (nitrogen, argon) and water-gas shift products (water, carbon monoxide, carbon dioxide, hydrogen).

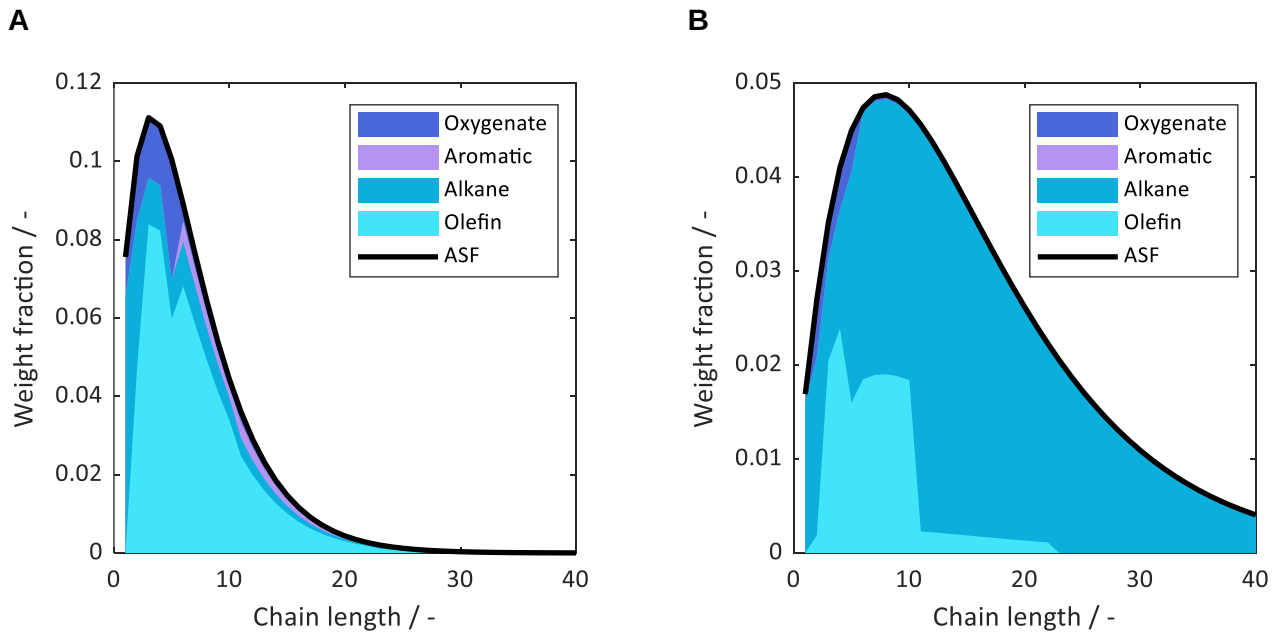

Supplementary Figure 1: Weight fractions of the modeled syncrude composition for (A) HT-FT with a chain growth probability α of 0.74 and (B) LT-FT synthesis with an α-value of 0.88 without water-gas shift compounds (CO, H_2, CO_2, and H_2O). The distribution of the compound classes oxygenates, aromatics, alkanes, and olefins is adopted from de Klerk[99] (Supplementary Table 3) and represents typical syncrude compositions for HT-FT and LT-FT syntheses. The black bold curve represents the Anderson-Schulz-Flory (ASF) distribution.

Syncrude recovery. To recover the syncrude from the water-gas shift compounds, industrial FT plants use stepwise cooling and phase separation during the so-called syncrude recovery. Syncrude recovery is followed by refining steps of targeted products.[16,105] The recovered syncrude is thereby pre-fractionated into a tail gas (C_1-C_4), naphtha (C_5-C_{10}), and distillate (C_{11+}) cut. The tail gas cut is further treated in the so-called gas loop, whereas the naphtha and distillate cut are fractionated in the atmospheric distillation unit. In the tail gas cut, water-gas shift compounds are

also present in addition to hydrocarbons, with substantial amounts of unconverted CO in the case of LT-FT synthesis due to its low CO conversion. We model this process sequence based on the work of Rodríguez Vallejo et al.[16] For simplicity, we assume sharp splits for mass balances of separation units. We estimate the separation units' energy consumptions with AspenPlus models.

The product of LT-FT synthesis has a liquid and gaseous phase that are separated with a Flash2 block at reactor conditions. In contrast, the HT-FT product is solely gaseous. The gaseous phases of LT-FT and HT-FT syntheses are separated into an organic gaseous, organic liquid, and aqueous liquid stream in two three-phase separators. The organic gaseous stream, called tail gas, contains C_1-C_4 hydrocarbons and water-gas shift compounds and is led to the gas loop. The organic liquid stream contains the naphtha cut of C_5-C_{10} and the distillate cut of C_{11+} hydrocarbons and is sent to the atmospheric distillation unit. The aqueous liquid stream contains water and oxygenated compounds and is treated as wastewater. Both three-phase separators are modeled with Flash3 blocks in AspenPlus. The three-phase separators are modeled with a pressure of 10 bar for LT-FT and 20 bar for HT-FT synthesis and temperatures of 150 °C and 40 °C for the first and second separator, respectively.

Gas loop. The overall carbon efficiency of the process concept is strongly affected by the fate of unconverted CO in the gas loop.[99] Gas loop designs among industrial FT facilities differ greatly,[99] and finding the optimal gas loop is a complex design problem that is beyond the scope of this study. However, all gas loop designs are in-between two extremes considered in this study: an open-loop and a closed-loop design.[106] In both gas loop designs, purge gases and by-products can be incinerated for heat recovery followed by optional CO_2 capture or flared (see Supplementary Figure 6). In our open-loop design, no tail gas is recycled, resulting in a simple process concept at the cost of low carbon efficiency. In this case, the entire tail gas stream is purged without any CO recovery.

In contrast, our closed-loop design aims for maximum recovery of CO and H_2 that are recycled to the FT reactor inlet. The closed-loop design improves the carbon efficiency, however, at the cost of a complex process sequence that includes cryogenic separation of C_1-C_2 hydrocarbons, resulting in additional utility consumption.[99] To prevent inert gas build-up,[106] 5% of the tail gas are purged. The remaining tail gas is cooled to 25 °C and fed to a Benfield unit, where CO_2 is separated. The Benfield unit's energy consumption is modeled with 1.56 MJ of heat and 0.05 MJ of electricity per kg of CO_2, based on Bartoo.[107] The temperature of the CO_2-free tail gas stream is assumed to be 101 °C, following Kohl et al.[108] Before separation in a three-phase separator at reactor pressure, the tail gas stream is cooled to 5 °C.

The three-phase separator is modeled as Flash3 block in AspenPlus, and the top gaseous stream is sent to a rectification column modeled with a rigorous RadFrac block with a partial-vapor condenser. Note that separating CO and H_2 from short-chain hydrocarbons requires cryogenic operating temperatures of approximately -170 °C in the condenser. Targeted recovery rates are set to over 99% for CO and H_2 in the top and all other compounds in the bottom stream. For HT-FT synthesis, the optimized rectification column has 8 stages with the feed entering at the 7th stage, a reflux ratio of 2.65, and a top-to-feed ratio of 0.74. In contrast, for the LT-FT synthesis, the optimized rectification column has 6 stages with the feed entering at the 5th stage, a reflux ratio of 1.09, and a top-to-feed ratio of 0.97. Next, the top stream is heated to 20 °C and is assumed to consist of purely CO and H_2 for simplicity.

Atmospheric distillation unit. In the atmospheric distillation unit (ADU), the organic liquid stream is separated into a naphtha and distillate cut at 1 bar. The rectification column is modeled with a rigorous RadFrac block in AspenPlus with a total condenser. Targeted recovery rates are set to 99% for decane in the top and undecane in the bottom stream. For HT-FT synthesis, the optimized ADU has 38 stages with the feed entering at the 18th stage, a reflux ratio of 0.23, and a top-to-feed ratio of 0.80. In contrast, for the LT-FT synthesis, the optimized ADU has 46 stages with the feed entering at the 24th stage, a reflux ratio of 0.35, and a top-to-feed ratio of 0.53.

Removal of aromatics and oxygenates. After the atmospheric distillation unit, the naphtha and distillate cuts still contain aromatics and oxygenates, which are undesirable in the HyFiT-fuel. Their removal is thus necessary to obtain a mixture consisting solely of olefins and alkanes. To the authors' knowledge, industrial applications for the selective removal of aromatics and oxygenates from entire naphtha and distillate cuts are not documented in open-access literature. We, therefore, estimate the utility requirements for this separation sequence with proxy data of the "UOP Sulfolane process," which is industrially used for high-purity recovery of aromatics from hydrocarbon mixtures.[109] The "UOP Sulfolane process" is named after the used solvent and combines liquid-liquid extraction with extractive distillation.

Note that oxygenates in the C_5-C_{10} and C_{11+} cuts contain alcohols that could be also used as components in HyFiT-fuels. However, the C_5-C_{10} and C_{11+} cuts contain much less oxygenates compared to, in particular, olefins that can be hydroformylated and hydrogenated to alcohols in much greater amounts (see Supplementary Table 2). Additionally, these alcohols in the C_5-C_{10} and C_{11+} cuts would have to be separated from other oxygenated compounds such as carboxylic acids, carbonyls, and ketones that are undesirable components in HyFiT-fuels. Such a separation sequence would increase the utility consumption which would have to be weighed against the benefit of a slightly increased carbon efficiency. Consequently, in this study, we decided to remove the small amounts of

oxygenates entirely in this initial process concept in favor of a simpler process design. Still, the potential of using the alcohols of the C_5-C_{10} and C_{11+} cuts should be considered for proceeding process optimization of HyFiT-fuel production.

In this estimation, we assume a sharp split into a product stream consisting of alkanes and olefins and a by-product stream consisting of aromatics and oxygenates. The process operates at 1 bar, and inputs are heated to 116 °C before entering.[110] Utility requirements are determined to 1.39 MJ of heat, 0.03 MJ of electricity, and 5.03 kg of cooling water per kg of process input, according to Meyers.[109] For heat consumption, we assume a temperature level of 300 °C since sulfolane, with a boiling temperature of 287 °C at 1 bar, needs to be vaporized.[110] The temperature of the product stream is estimated to 100 °C, corresponding to the documented extractor top temperature.[110]

Since using proxy data for such an essential separation sequence may induce large uncertainty to the calculated environmental impacts of the HyFiT-fuel, we perform a sensitivity analysis (see Supplementary Note 24). In this sensitivity analysis, we find that the carbon footprint of HyFiT-fuels is only slightly sensitive towards the quantity and temperature level of heat consumption of the proxy process. Future studies on the HyFiT-fuel concept should focus on designing a suitable separation sequence. The separated aromatics and oxygenates can be either incinerated for heat recovery followed by optional CO_2 capture or flared (see Supplementary Figure 6).

Hydroformylation and hydrogenation. After removing aromatics and oxygenates, the naphtha cut consists of C_5-C_{10} olefins and alkanes. The naphtha cut is treated next by a hydroformylation and hydrogenation sequence to increase the amount of alcohols as oxygen carriers in the HyFiT-fuel. During hydroformylation, alkanes remain inert[111] while olefins are converted with equimolar syngas to aldehydes (Equation S2) by adding hydrogen and a formyl group (CHO) to the olefin's carbon-carbon double bond.[112] The aldehydes are subsequently hydrogenated to alcohols. The hydroformylation reactor is modeled as isothermal RStoic block in AspenPlus at reaction conditions of 90 °C and 15 bar, reported by Shaharun et al.[113] These reported reaction conditions are in the range of industrial hydroformylation processes.[114] For all olefins, the hydroformylation is modeled with the reported 1-octene conversion of 97% and *n*-nonanal yield of 95%.[113] The amount of required syngas is calculated by closing elemental balances and assuming complete syngas conversion.[115] As demonstrated by Warmeling et al., olefin isomers are the only by-products of aldehydes during hydroformylation.[116,117] Pressure and temperature of the reactants, olefins and syngas, are adjusted by compression, expansion, and heating to match reaction conditions. To ensure that all olefins are liquid before compression, the naphtha cut is cooled to 60 °C after the removal of aromatics and oxygenates.

$$\mathrm{C}_n\mathrm{H}_{2n} + \mathrm{CO} + \mathrm{H}_2 \rightarrow \mathrm{C}_{n+1}\mathrm{H}_{2(n+1)}\mathrm{O} \tag{S2}$$

During hydrogenation, aldehydes are converted with H_2 to alcohols, whereas unconverted and isomerized olefins are saturated to their corresponding alkanes (Equation S3-S4)).[111] For simplicity, we assume a yield of 100% since Redina et al. report yields greater than 99% for most hydrogenation reactions of C_6-C_{11} aldehydes at ambient conditions of 20 °C and 1 bar.[118] The hydrogenation reactor is modeled as isothermal RStoic block in AspenPlus, and the amount of required H_2 is calculated by closing elemental balances. The reactants are expanded and cooled to reaction conditions before entering the reactor. Heat releases of both reactors are calculated as enthalpy differences over each reactor in AspenPlus. After hydroformylation and hydrogenation, the product mixture consists of the targeted C_6-C_{11} alcohols and C_5-C_{10} alkanes.

$$\mathrm{C}_n\mathrm{H}_{2n}\mathrm{O} + \mathrm{H}_2 \rightarrow \mathrm{C}_n\mathrm{H}_{2n+1}\mathrm{OH} \tag{S3}$$

$$\mathrm{C}_n\mathrm{H}_{2n} + \mathrm{H}_2 \rightarrow \mathrm{C}_n\mathrm{H}_{2(n+1)} \tag{S4}$$

Hydrocracking. After the removal of aromatics and oxygenates, the distillate cut of C_{11+} olefins and alkanes is sent to the hydrocracking process. In our hydrocracker model, olefins are saturated to their corresponding alkanes (Equation S4) and long-chain C_{17+} alkanes are cracked to chain lengths of C_9-C_{17}. We model the cracking by splitting each C_{17+} alkane into two alkanes of equal carbon chain length until all alkanes are in the range of C_9-C_{17} (Equation S5). Consequently, the product mixture of the hydrocracker outlet stream consists solely of C_9-C_{17} alkanes. The amount of required H_2 for hydrocracking is calculated by closing elemental balances.

$$\mathrm{C}_n\mathrm{H}_{2(n+1)} + \mathrm{H}_2 \rightarrow \begin{cases} 2\ \mathrm{C}_{\frac{n}{2}}\mathrm{H}_{n+2} & \text{, for even } n > 17 \\ \mathrm{C}_{\frac{n-1}{2}}\mathrm{H}_{n+1} + \mathrm{C}_{\frac{n+1}{2}}\mathrm{H}_{n+3} & \text{, for odd } n > 17 \end{cases} \tag{S5}$$

For the utility requirements of hydrocracking, we consider 0.89 MJ of heat, 0.10 MJ of medium-pressure steam, 0.27 MJ of electricity, and 12.36 kg of cooling water per kg of process input. The utility requirements are derived from typical energy requirements of the "Chevron Lummus Global Isocracking process" in its two-stage configuration.[109] The "Isocracking" technology can be adapted to produce almost any desired product distribution and has been widely used in industry for decades,[109] e.g., in the wax hydrocracker of the Oryx gas-to-liquids FT facility.[99] We assume medium-pressure steam to be saturated at 184 °C, corresponding to the reported pressure level of 11 bar.[119] For the

reactants, we consider compression and heating of the liquid C_{11+} cut to 3.6 bar and 200 °C and of H_2 to 46 bar and 50°C.[120] H_2 compression is modeled by an isentropic two-stage MCompr block, using the ASME method. H_2 is compressed from 30 to 40 bar in the first stage, subsequently cooled to 50 °C, and compressed from 40 to 46 bar in the second stage.

Membrane separation. The LT-FT synthesis requires syngas with an H_2:CO ratio of 2:1, as the syngas is supplied by the production network of Bachmann et al.[121] In contrast, the HT-FT synthesis and hydroformylation require syngas with an H_2:CO ratio of 1:1. To adjust the syngas ratio from 2:1 to 1:1, we model a membrane separation unit in which excess H_2 is separated by membrane permeation. For ceramic membranes, Prabhu et al. report separation factors of 87,000 for H_2:CO mixtures.[122] No CO permeation through the membrane was observed, which corresponds to a selectivity towards H_2 of 100%. We assume that a pressure difference of 29 bar between the feed (30 bar) and permeate side (1 bar) is sufficiently high as driving force for the proposed membrane separation. The product, i.e., syngas with H_2:CO ratio of 1:1 at the retentate side, is modeled with the same pressure level as the feed (30 bar). In contrast, at the permeate side, the separated H_2 is compressed back to 30 bar, modeling an isentropic three-stage MCompr block with the ASME method. H_2 is compressed from 1 to 10 bar in the first stage, 10 to 20 bar in the second stage, and 20 to 30 bar in the third stage. After each stage, H_2 is cooled back to 20 °C.

By-product treatment. Depending on the supply chain optimization, by-products are either incinerated for energy recovery followed by optional CO_2 capture or flared. For energy recovery, we consider the lower heating values of the incinerated by-products for the heat releases. For optional CO_2 capture from the flue gas, we adapt energy requirements of 2.75 MJ of heat per kg of captured CO_2 at 154 °C, 0.02 MJ of electricity per kg of captured CO_2 and a CO_2 absorption rate of 90% from Dubois et al.[123] Before CO_2 capture, the flue gas is cooled to 40 °C.[123]

Supplementary Note 4: Fuel production: process flowsheets

In the following, we present detailed flowsheets of the HyFiT process concept with HT-FT or LT-FT synthesis and either open-gas-loop or closed-gas-loop design. Additionally, we show a process flowsheet of the by-product treatment.

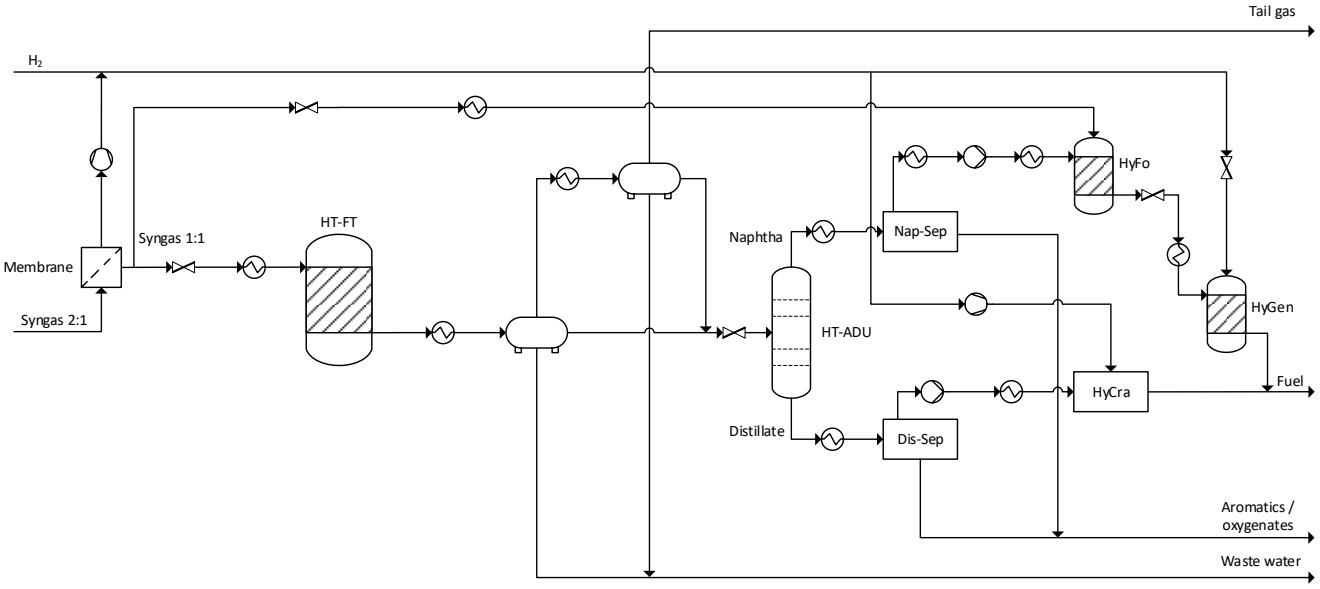

Supplementary Figure 2: Flowsheet of the HyFiT process concept for the HT-FT synthesis and the open-gas-loop design. Related to Figure 2. ADU: atmospheric distillation unit, Nap-Sep: naphtha separation, Dis-Sep: distillate separation, HyFo: hydroformylation, HyGen: hydrogenation, HyCra: hydrocracking.

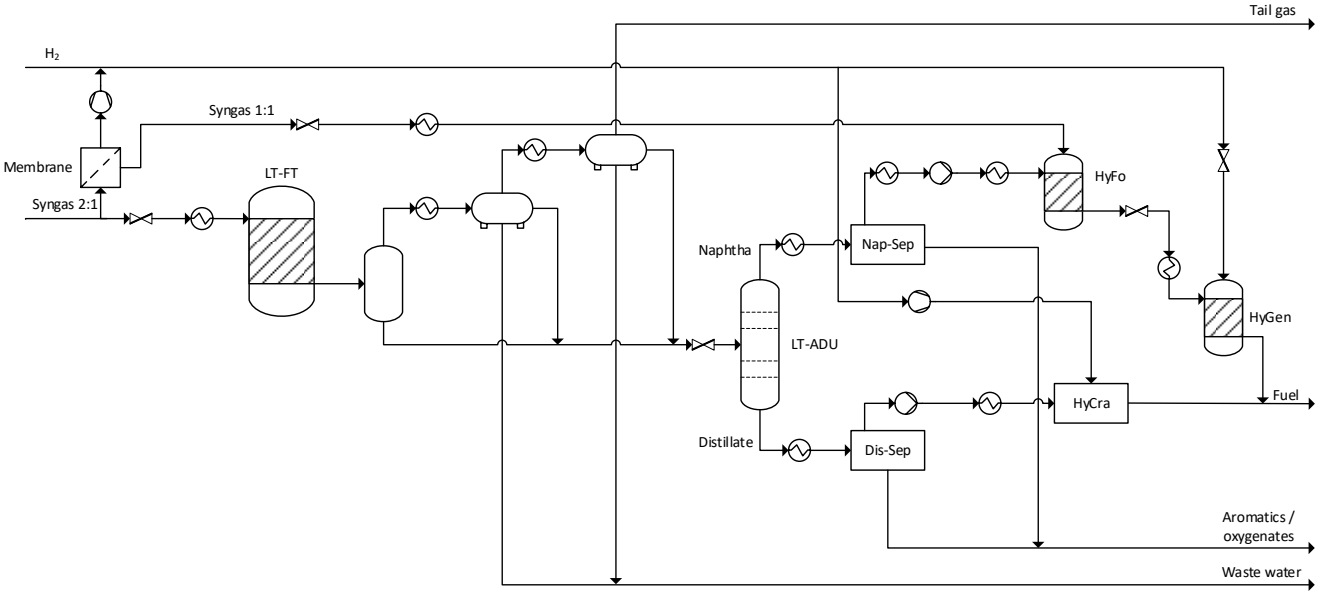

Supplementary Figure 3: Flowsheet of the HyFiT process concept for the LT-FT synthesis and the open-gas-loop design. Related to Figure 2. ADU: atmospheric distillation unit, Nap-Sep: naphtha separation, Dis-Sep: distillate separation, HyFo: hydroformylation, HyGen: hydrogenation, HyCra: hydrocracking.

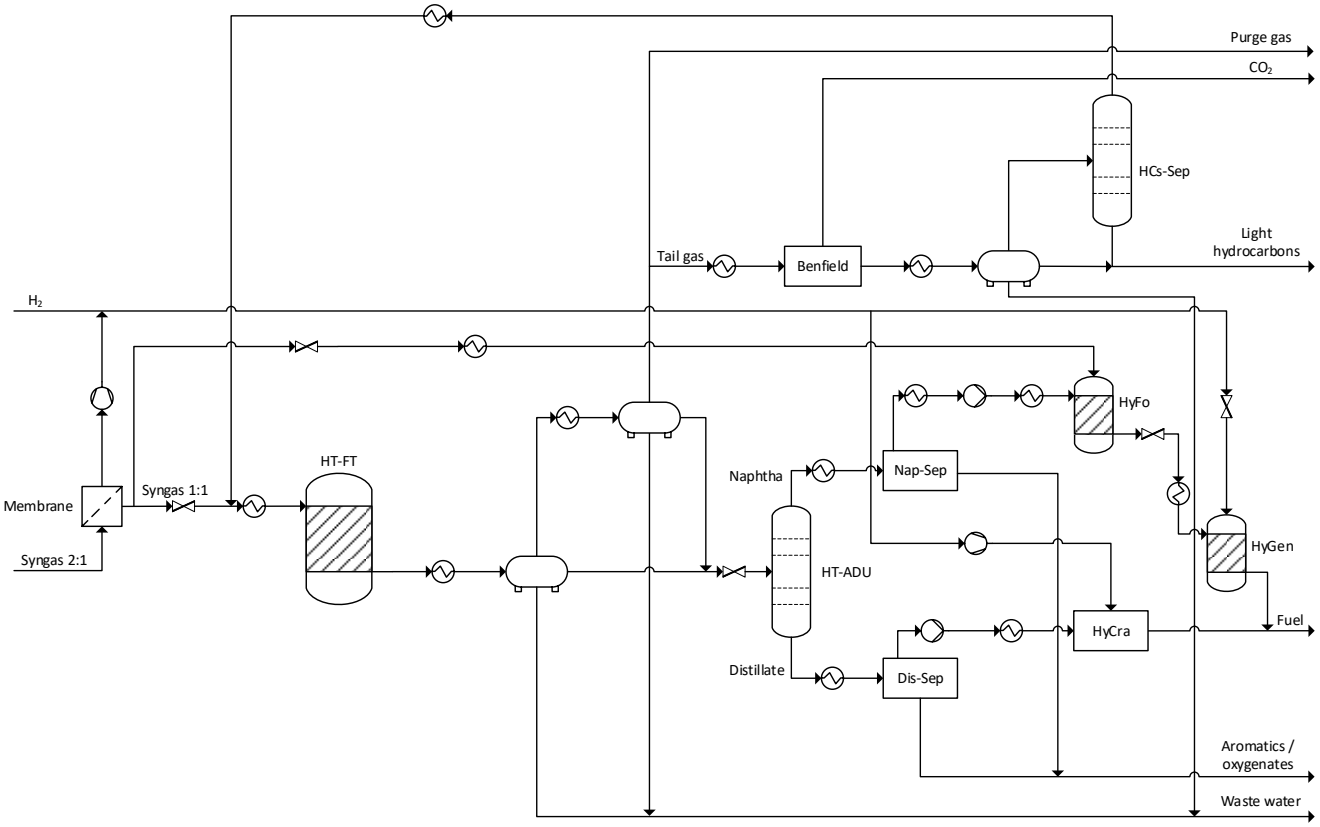

Supplementary Figure 4: Flowsheet of the HyFiT process concept for the HT-FT synthesis and the closed-gas-loop design. Related to Figure 2. ADU: atmospheric distillation unit, Nap-Sep: naphtha separation, Dis-Sep: distillate separation, HyFo: hydroformylation, HyGen: hydrogenation, HyCra: hydrocracking, HCs-Sep: hydrocarbons separation.

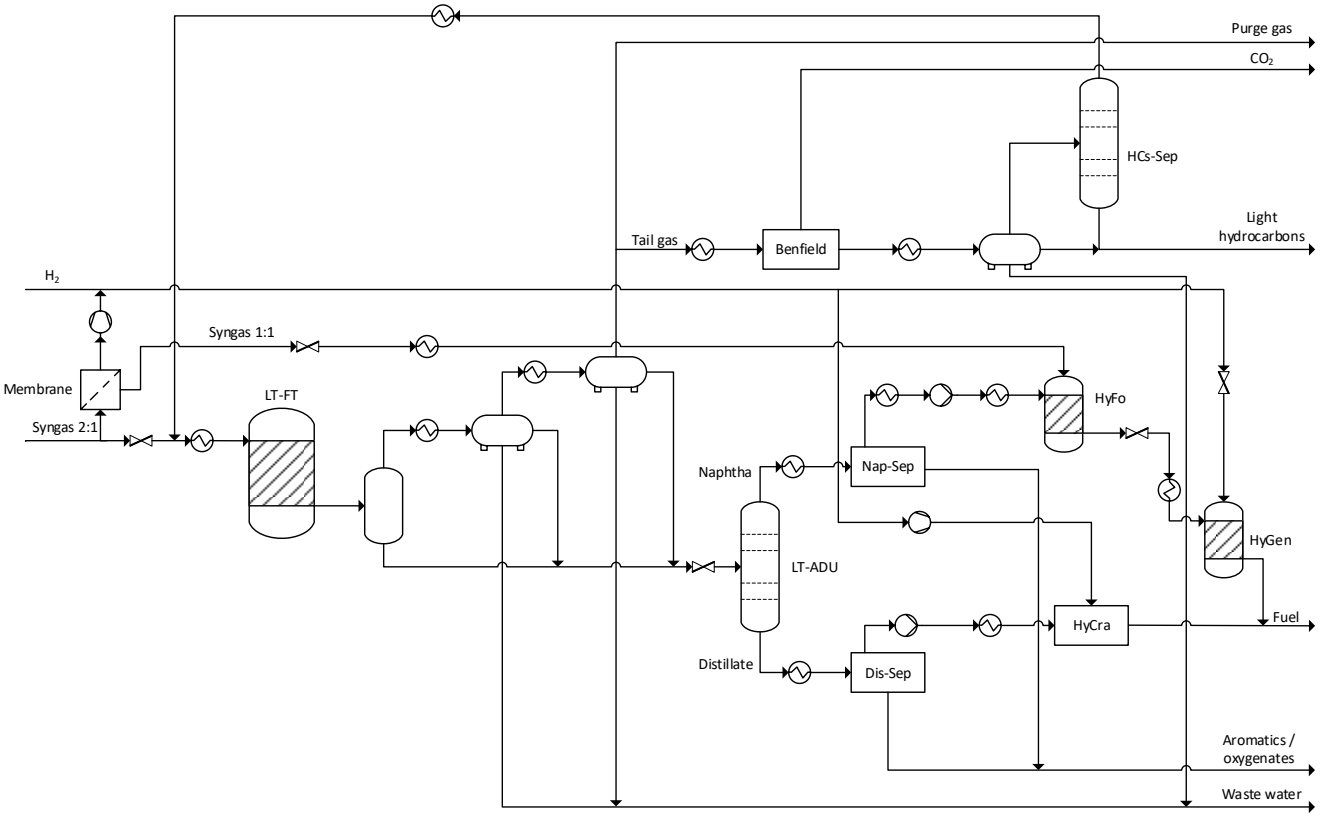

Supplementary Figure 5: Flowsheet of the HyFiT process concept for the LT-FT synthesis and the closed-gas-loop design. Related to Figure 2. ADU: atmospheric distillation unit, Nap-Sep: naphtha separation, Dis-Sep: distillate separation, HyFo: hydroformylation, HyGen: hydrogenation, HyCra: hydrocracking, HCs-Sep: hydrocarbons separation.

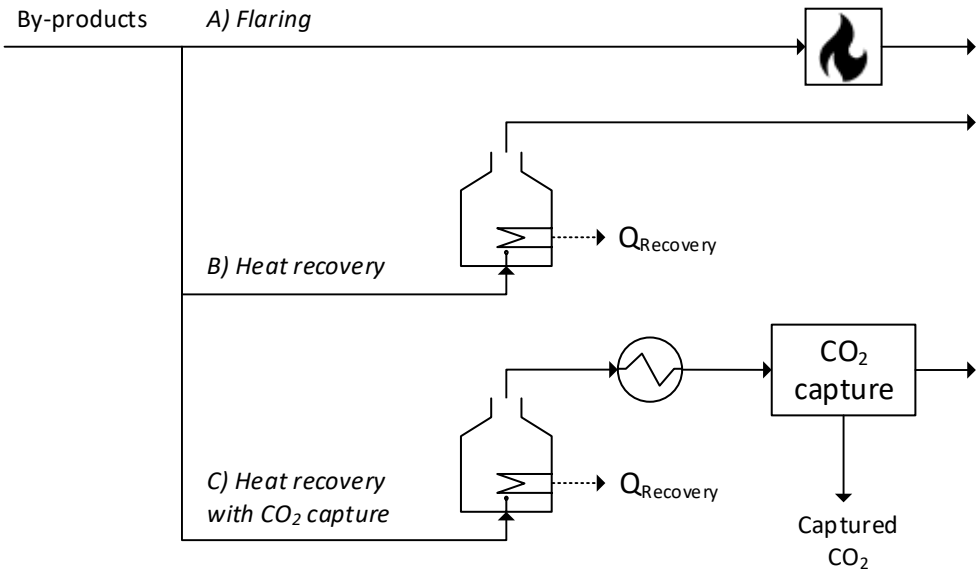

Supplementary Figure 6: Flowsheet of by-product treatment. Related to Figure 2. By-products can either be (A) flared, (B) incinerated for heat recovery, or (C) incinerated for heat recovery followed by CO_2 capture of the off-gas.

Supplementary Note 5: Fuel production: fuel composition

In Supplementary Table 3, we present the modeled fuel compositions of the HyFiT-fuel production concept that consists of several process units including FT synthesis and hydroformylation (see Figure 2). Depending on the FT synthesis used in the HyFiT-fuel production concept, the resulting HyFiT-fuel is either rich in alkanes (LT-FT synthesis, Supplementary Table 3A) or alcohols (HT-FT synthesis, Supplementary Table 3B). By combining both LT-FT and HT-FT synthesis, the desired alcohol-alkane ratio of the HyFiT-fuel can be adjusted (Supplementary Table 3C).

Supplementary Table 3: The modeled composition of HyFiT-fuels. Mass fractions of HyFiT-fuel produced via hydroformylation and (A) LT-FT or (B) HT-FT synthesis (see Figure 2). Summed values differ slightly due to rounding. (C) By combining HyFiT-fuels produced from both hydroformylation and LT-FT as well as HT-FT synthesis, the desired alcohol-alkane ratio of the HyFiT-fuel can be adjusted. The HyFiT-fuels with 20 wt% (HyFiT-20%) and 40 wt% (HyFiT-40%) alcohol are marked with ([a]) and ([b]), respectively.

A

Carbon atoms	Mass fraction wt%	
	Alcohol	Alkane
5	–	3
6	2	3
7	3	3
8	3	3
9	3	10
10	2	10
11	2	10
12	–	9
13	–	8
14	–	7
15	–	7
16	–	6
17	–	5
Σ	**15**	**85**

B

Carbon atoms	Mass fraction wt%	
	Alcohol	Alkane
5	–	2
6	14	2
7	15	2
8	12	2
9	10	3
10	8	2
11	7	6
12	–	4
13	–	3
14	–	3
15	–	2
16	–	2
17	–	1
Σ	**65**	**35**

C

Mixing ratio of HyFiT-fuel from LT-FT to HT-FT synthesis	wt%	100:0	90:10 [a]	80:20	70:30	60:40	50:50 [b]	0:100
Alcohol content	wt%	15	20 [a]	25	30	35	40 [b]	65
Alkane content		85	80 [a]	75	70	65	60 [b]	35

Supplementary Note 6: Fuel usage: fuel standards

Common global fuel standards and their limits are listed in Supplementary Table 4. Numerical values of the investigated fuel properties are presented in Supplementary Table 7.

Supplementary Table 4: Fuel standards for diesel, paraffinic diesel, and biodiesel with their respective limits for the derived cetane number (DCN), viscosity, density, and lubricity. Related to Figure 4.

Standard	Region	Fuel	DCN	Viscosity		Density		Lubricity
			–	$mm^2\ s^{-1}$		$kg\ m^{-3}$		µm
			min	min	max	min	max	max
EN 590 (summer)	EU	Diesel	51	2.0	4.5	820	845	460
EN 590 (winter)	EU	Diesel	49	2.0	4.5	820	860	–
EN 15940	EU	Paraffinic diesel	70	2.0	4.5	765	800	460
EN 14214	EU	Biodiesel	51	3.5	5.0	860	900	–
ASTM D975	USA	Paraffinic diesel	40	1.9	4.1	–	–	520
ASTM D7467	USA	Diesel	40	1.9	4.1	–	–	520
ASTM D6751	USA	Biodiesel	47	1.9	6.0	–	–	–
GOST 305-82 (summer)	Russia	Diesel	45	3.0	6.0	–	860	–
GOST 305-82 (winter)	Russia	Diesel	45	1.8	5.0	–	840	–
CAN/CGSB-3.524	Canada	Biodiesel	–	1.9	6.0	–	–	–
CAN/CGSB-3.522	Canada	Diesel	40	1.7	4.1	–	–	–
CAN/CGSB-3.520	Canada	Diesel	40	1.3	4.1	–	–	–
GB 19147-2016 (China VI)	China	Diesel	51	3.0	8.0	810	850	460
GB 25199-2017	China	Diesel	49	1.9	6.0	820	900	–
GB/T 20828	China	Biodiesel	49	1.9	6.0	820	900	–
JIS K 2204 (No. 2)	Japan	Diesel	50	2.5	–	–	860	–
JIS K 2204 (No. 3, winter)	Japan	Diesel	50	1.7	–	–	860	–
JIS K 2390	Japan	Biodiesel	51	3.5	5.0	860	900	–
IS 15607: 2005	India	Biodiesel	48	2.5	6.0	860	900	–
SANS 1935	South Africa	Biodiesel	51	3.5	5.0	860	900	–

Supplementary Note 7: Fuel usage: fuel properties

Lower heating value. The lower heating value (LHV) of HyFiT-fuels is calculated as the sum of each fuel component's product of LHV and mass fraction y in the HyFiT-fuel:

$$\mathrm{LHV_{HyFiT}} = \sum_{i}^{n} \mathrm{LHV}_{i,\mathrm{HyFiT}} \cdot \mathrm{y}_{i,\mathrm{HyFiT}}. \quad (S6)$$

LHVs of all fuel components are listed in Supplementary Table 5. The mass fractions of alcohols and alkanes in the fuel depend on the targeted alcohol-alkane ratio of the HyFiT-fuel, i.e., on the combination of LT-FT and HT-FT synthesis. The composition of HyFiT-fuels is presented in Supplementary Note 5.

Supplementary Table 5: Lower heating values of all alcohols and alkanes present in HyFiT-fuels. For each alcohol and alkane, the lower heating value is calculated from the enthalpy of reaction of stoichiometric combustion with oxygen. Required standard enthalpies of formation of each reactant and product are taken from NIST.[124]

Carbon atoms	Lower heating value MJ kg^{-1}	
	Alcohol	Alkane
5	–	44.98
6	35.98	44.74
7	36.88	44.56
8	37.61	44.42
9	38.17	44.33
10	38.65	44.24
11	39.03	44.17
12	–	44.11
13	–	44.06
14	–	44.02
15	–	43.99
16	–	43.95
17	–	43.93

Viscosity. An Ubbelohde viscometer, according to DIN 51562,[125] and a thermostat with a temperature constancy of 0.01 K were used to determine the viscosity. Measurements were carried out at a temperature of 40 °C. Before each measurement, the viscometer was filled with the test liquid and placed in the thermostat. After filling the viscometers with the sample liquid, the viscometer was tempered for 30 minutes to ensure a constant temperature level of sample and viscometer. For the evaluation of the results, each measurement was repeated five times and the mean value was calculated.

Density. The density was measured with a tension scale (Tensiometer TD4) in buoyancy tests using the Archimedes principle. The measurement resolution of the scale and the temperature accuracy of the thermostat were 0.01 mg and 0.1 K, respectively, and measurements were carried out at 15 °C. During the measurements, the volume and mass of the displacement body (DB) were known (Supplementary Figure 7). For the calibration of the scale, the displacement body was placed outside of the sample liquid at first. After calibration, the displacement body was immersed into the sample liquid to measure its mass. The liquid density was subsequently calculated by

$$\mathrm{m_{measured}} \cdot \mathrm{g} = \sum_{i} \mathrm{F}_i = \mathrm{m_{DB}} \cdot \mathrm{g} - \mathrm{V_{DB}} \cdot \rho_{\mathrm{L}} \cdot \mathrm{g} \quad (S7)$$

$$\rho_{\mathrm{L}} = \frac{\mathrm{m_{DB}} - \mathrm{m_{measured}}}{\mathrm{V_{DB}}}. \quad (S8)$$

For the evaluation of the results, each measurement was repeated ten times.

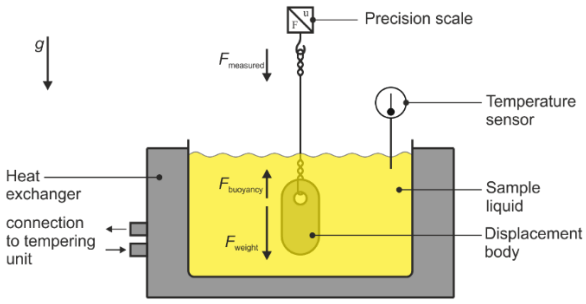

Supplementary Figure 7: Measurement of the liquid density with a precision scale.

Lubricity. For lubricity, the high frequency reciprocating rig (HFRR) value and friction coefficient were measured (Supplementary Figure 8). The HFRR tests were conducted according to ISO 12156-1:2018.[126] For each sample liquid, the test procedure was conducted five times with and without additive. The HFRR value is derived from the wear scar diameter (WSD), whereas the friction coefficient μ is calculated by the ratio of gravitational and tangential force:

$$\mathrm{WSD} = \frac{\mathrm{dx} + \mathrm{dy}}{2} \tag{S9}$$

$$\mu = \frac{\mathrm{F_{grav}}}{\mathrm{F_{tan}}}. \tag{S10}$$

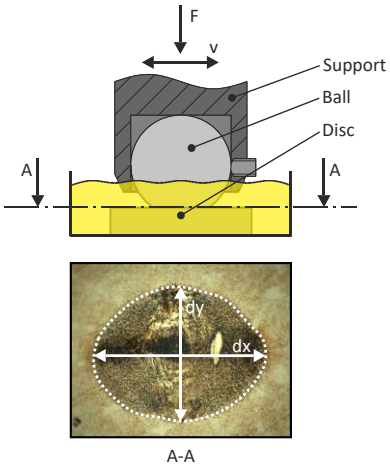

Supplementary Figure 8: Measurement of the high frequency reciprocating rig (HFRR) value and friction coefficient.

Supplementary Note 8: Fuel usage: material compatibility

Material compatibility tests were carried out according to DIN ISO 1817.[127] As sealing materials, the reference elastomers FKM, NBR, and HNBR were considered, following DIN ISO 13226.[128] For each elastomer, three samples were measured. At the beginning of one test series, the reference materials were placed in the sample liquids. Immediately before and at defined time intervals within the experiment (Supplementary Table 6), the material properties mass, volume, and hardness were determined. Since the largest changes in sealing and liquid properties are to be expected at the beginning of a measurement series, the individual measurements initially take place within short time intervals that become longer as the measurement series progresses. The intervals listed are based on empirical values from previous experiments and represent a reasonable compromise between acceptable measurement effort and sufficient data volume. All measurements to determine the material compatibility were carried out in air-conditioned rooms at 23±2 °C, according to the laboratory conditions in DIN ISO 23529.[129] To ensure a constant temperature of liquids and elastomers between two measuring points, the samples were stored in a climate chamber at 23 °C. The local temperature constancy of the chamber is specified by the manufacturer as ± 0.2 °C, while the temporal constancy is ± 0.5 °C. Each test series ended after 672 h.

Supplementary Table 6: Timing of the measurements.

	Sealing	Sealing plus liquid							
Measurement point	1	2	3	4	5	6	7	8	9
Time since start of the test series in h	0	6	16	24	72	168	336	504	672

Change of mass. The mass change was measured with a precision scale (Sartorius Research R 160 P) that has a measurement resolution of 0.01 mg and standard deviation of 0.02 mg.[130] For the measurement process, the scale was calibrated at first. Elastomers were taken from the sample vessel and carefully cleaned with lint-free paper so that the liquid on the elastomer surface is removed. Next, the elastomer was put on the scale and, after the balance had settled in, the mass change was measured. Note that, in case of high vapor pressures, the measurement process may be influenced by evaporation of the sample liquid (Supplementary Figure 9), but the influence of evaporation played only a minor role for all HyFiT-fuels. All HyFiT-fuels showed comparable behavior to diesel. All samples were measured once and each measurement process took less than 10 s.

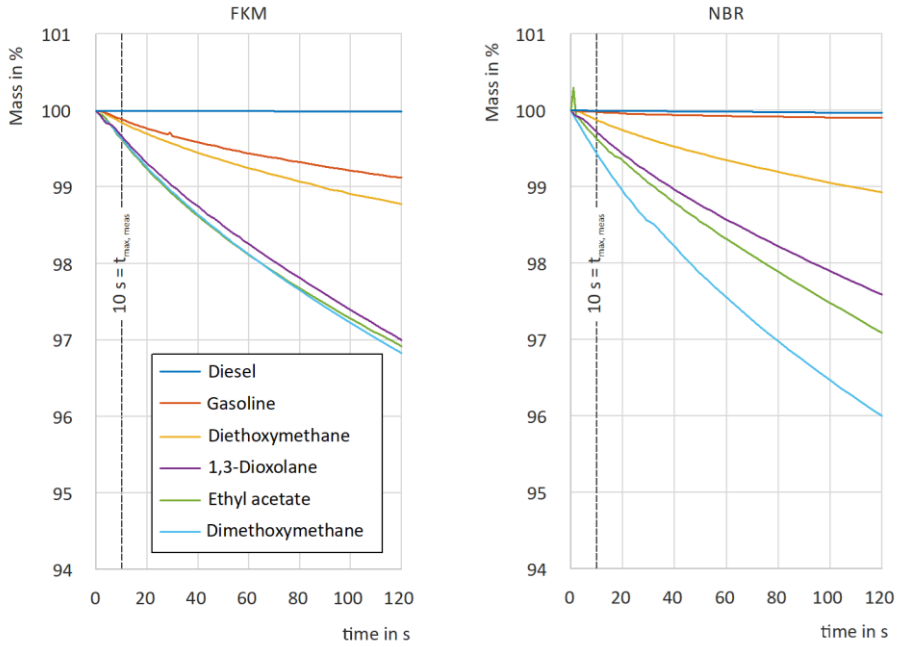

Supplementary Figure 9: Mass change over time due to evaporation during the measurement process of various fuels.

Change of volume. The volume change was measured with a tension scale (Tensiometer TD4, Supplementary Figure 7) that has a measurement resolution of 0.01 mg and temperature accuracy of 0.02 K.[131,132] As prerequisites, the density of the reference liquid and the mass of the displacement body are known. The measurement process

follows the description of the density measurement above. Each measurement was repeated three times with a measurement temperature of 20 °C. The sample volume V_S is calculated as follows:

$$m_{measured} \cdot g = \sum_i F_i = m_{DB} \cdot g - V_S \cdot \rho_L \cdot g \quad (S11)$$

$$V_S = \frac{m_{DB} - m_{measured}}{\rho_L}. \quad (S12)$$

Change of hardness. The hardness change was measured with a hardness test device,[133] according to DIN ISO 48.[134] The measurement process was repeated six times for each elastomer sample.

Supplementary Note 9: Fuel usage: numerical results of fuel properties and material compatibility

Numerical values of material compatibility results and fuel properties are shown in Supplementary Table 7 for HyFiT-fuels with alcohol contents between 15 and 65 wt%.

Supplementary Table 7: The considered fuel properties and the material compatibility results for HyFiT-fuels with alcohol contents between 15 and 65 wt%. The measurements for the change of mass and volume of FKM and 30 wt% alcohol gave inconsistent results. This data point is shown in brackets and not included in the further analysis. Related to Figure 4.

		Limits		Alcohol content of HyFiT-fuel						
		Lower	Upper	15%	20%	25%	30%	35%	40%	65%
Material compatibility [a]										
Change of mass		–	–							
FKM				0.2%	0.2%	0.1%	(-1.6%)	0.1%	0.2%	0.1%
HNBR				6.9%	7.0%	7.6%	7.6%	7.7%	8.5%	8.6%
NBR				9.7%	9.8%	10.8%	10.9%	10.9%	10.9%	10.7%
Change of volume		-5%	10%							
FKM				0.2%	-0.6%	-0.5%	(-3.2%)	-0.4%	0.1%	-0.6%
HNBR				10.4%	9.3%	9.6%	9.9%	9.7%	12.6%	10.9%
NBR				15.4%	13.7%	14.4%	14.9%	15.2%	16.8%	14.8%
Change of hardness		-10%	15%							
FKM				-14.5%	-0.7%	-0.5%	0.0%	-2.0%	-6.6%	-0.6%
HNBR				-13.5%	-11.0%	-5.5%	-7.4%	-10.1%	-12.6%	-12.0%
NBR				-2.6%	-17.4%	-19.2%	-14.6%	-18.4%	-12.6%	-13.4%
Fuel properties [b]										
LHV	MJ kg^{-1}	–	–	43.2	42.9	42.6	42.2	41.9	41.5	39.8
DCN	–	51	–	66	64	63	60	59	56	48
Viscosity	mm^2 s^{-1}	2.0	4.5	1.4	1.5	1.5	1.6	1.7	2.0	2.9
Density	kg m^{-3}	820	845	757	766	769	772	777	782	805
Lubricity										
HFRR [c]	µm	–	460	577 [d]	568 [d]	571 [d]	534 [d]	538 [d]	546 [d]	492 [d]
				417 [e]	430 [e]	384 [e]	432 [e]	411 [e]	430 [e]	429 [e]
Friction	–	–	–	0.55 [d]	0.53 [d]	0.53 [d]	0.50 [d]	0.51 [d]	0.48 [d]	0.42 [d]
coefficient				0.23 [e]	0.22 [e]	0.24 [e]	0.20 [e]	0.21 [e]	0.20 [e]	0.18 [e]

[a] Determined values at the end of each test series, i.e., after 672 h (see Supplementary Note 8). Limits are taken from Richter.[135,136]
[b] Limits are taken from the EN 590 diesel fuel standard.
[c] High frequency reciprocating rig.
[d] Measured without additive.
[e] Measured with additive (2000 ppm of R655).

Supplementary Note 10: Fuel usage: combustion emissions

The diesel engine features two-stage turbocharging and cooled exhaust gas recirculation (EGR). The exhaust gas aftertreatment system of the vehicle consists of a diesel-oxidation catalyst and a diesel-particulate filter with a selective catalytic reduction (SCR) coating followed by an ammonia-slip catalyst. The hybrid strategy is calibrated to minimize tailpipe NO_x emissions.[137] Thereby, the current Euro 6d final emissions standards and the requirements for the upcoming Euro 7 are already met in the investigated cycle, using regular diesel. In the following, we present the powertrain layout of the P0P2 plug-in hybrid vehicle (Supplementary Figure 10) and describe how we corrected the deviation of the battery state of charge (SOC).

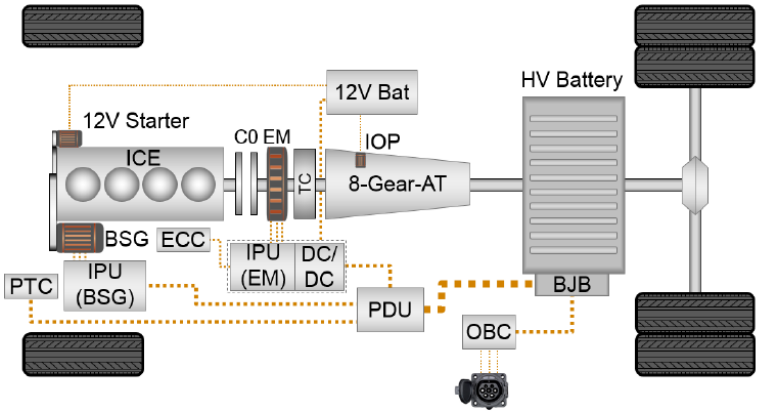

Supplementary Figure 10: Powertrain layout of the P0P2 plug-in hybrid vehicle.

For plug-in hybrid vehicles, the test procedure of the worldwide harmonized light vehicles test procedure (WLTP) provides for a charge sustain mode, which means that the battery must have the same SOC at the end of the cycle as at the beginning, with a tolerance of 1%. No adjustments were made to the vehicle calibration for the tests. In combination with the different lower heating values of the HyFiT-fuels (see Figure 4A), deviations of the SOC of -2.2% for HyFiT-20% and -2.5% for HyFiT-40% occur (Supplementary Figure 11). The diesel base measurement also shows a SOC deviation of -1.2%.

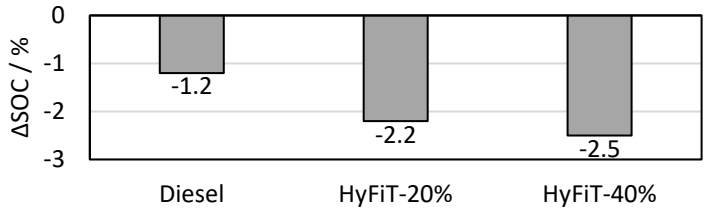

Supplementary Figure 11: Comparison of the deviation in battery state of charge (ΔSOC) of diesel, HyFiT-20%, and HyFit-40%.

To enable a comparison of the tests with different fuels, the fuel consumption as well as CO_2, NO_x, and particulate matter (PM) emissions are corrected according to the SOC deviation. The corrected fuel consumption $\mathrm{FC_{SOC}}$ is calculated by converting the electrical energy required to charge the battery ($\Delta\mathrm{SOC} \cdot \mathrm{cap_{Batt}}$) into the corresponding fuel quantity with the fuel's lower heating value ($\mathrm{H_u}$) and density (ρ), the average efficiency of the combustion engine ($\bar{\eta}_{\mathrm{ICE}} = 35\%$), the conversion efficiencies for battery charging/discharging ($\bar{\eta}_{\mathrm{Ch/Dch}} = 90\%$) determined from experimental investigations, and the driven cycle distance ($\mathrm{s_{cycle}}$):

$$\mathrm{FC_{SOC}} = \mathrm{FC} - \frac{\Delta\mathrm{SOC} \cdot \mathrm{cap_{Batt}}}{\mathrm{H_u} \cdot \rho \cdot \bar{\eta}_{\mathrm{ICE}} \cdot \bar{\eta}_{\mathrm{Ch,Dch}} \cdot \mathrm{s_{cycle}}}. \quad \text{(S13)}$$

The corrected CO_2 emissions $\mathrm{m_{CO2,SOC}}$ are calculated based on the corrected fuel consumption $\mathrm{FC_{SOC}}$, the fuel's carbon mass fraction $\mathrm{Y_{C,Fuel}}$ and density ρ, and the molar masses M of CO_2 and carbon:

$$\mathrm{m_{CO2,SOC}} = \mathrm{FC_{SOC}} \cdot \mathrm{Y_{C,Fuel}} \cdot \rho \cdot \frac{\mathrm{M_{CO2}}}{\mathrm{M_C}}. \quad \text{(S14)}$$

For the example of diesel, this results in

$$FC_{SOC,Diesel} = 9.74\ \frac{L}{100\ km} - \frac{-1.15\% \cdot 13.5\ kW \cdot 3600\ s}{42800\ \frac{kJ}{kg} \cdot 0.833\ \frac{kg}{L} \cdot 0.35 \cdot 0.9 \cdot 23.1\ km} \cdot 100 = 9.96\ \frac{L}{100\ km} \quad (S15)$$

$$m_{CO2,SOC,Diesel} = 9.96\ \frac{L}{100\ km} \cdot 0.86 \cdot 833\ \frac{g}{L} \cdot \frac{44\ \frac{g}{mol}}{12\ \frac{g}{mol}} = 262\ \frac{g}{km}. \quad (S16)$$

The correction of NO_x and PM emissions is carried out analogously via the brake-specific engine-out emissions, taking into account the average conversion efficiency of the exhaust gas aftertreatment system (EATS) for the tailpipe emissions (NO_x: $\bar{\eta}_{EATS,NOx,Diesel} = 93\%$, $\bar{\eta}_{EATS,NOx,HyFiT20\%} = 91\%$, $\bar{\eta}_{EATS,NOx,HyFiT40\%} = 90\%$; PM: $\bar{\eta}_{EATS,PM,Diesel} = 99\%$, $\bar{\eta}_{EATS,PM,HyFiT20\%} = 99\%$, $\bar{\eta}_{EATS,PM,HyFiT40\%} = 98\%$). Due to the lower exhaust gas temperatures, the conversion efficiency of the NO_x exhaust gas aftertreatment system is on average lower for the HyFiT-fuels than for conventional diesel fuel.

As HyFiT-fuels greatly reduce PM emissions (see Figure 5), NO_x emissions may be reduced by increasing the EGR rate. Since the calibration of the test vehicle cannot be changed, we estimate the NO_X reduction potential based on previously measured FT fuels with comparable oxygen contents on a single cylinder research engine (Supplementary Table 8).[138] These measurements provide detailed information on the PM-NO_X trade-off, which we apply to the HyFiT-fuel vehicle measurements for two cases:

In the first case, the EGR rate is increased iteratively until the NO_X tailpipe emissions of the HyFiT operation correspond to those of the diesel operation, i.e., the NO_x reduction potential is not fully utilized in favor of PM and CO_2 emissions. In the second case, the EGR rate is increased until the engine-out PM emissions of the HyFiT operation correspond to those of the diesel operation. Thereby, NO_X is reduced more than in the first case, but CO_2 emissions are also increased, resulting from higher mass flows associated with the increased EGR rate and faster loading of the particulate filter. Single cylinder measurements with conventional diesel show that increasing the EGR rate to reduce NO_X emissions by 0.1 g kWh^{-1} increases CO_2 emissions by 0.083%.[10,139] Since this effect occurs mainly due to losses in the air path, these values can also be applied to HyFiT-fuel operation to estimate the impact of an increased EGR rate on CO_2 emissions. In both cases, we expect no significant impact of the measures on the conversion efficiency of the SCR system.

When HyFiT-fuels are used instead of diesel, exhaust gas temperatures are, on average, lower, whereby the warm-up of the SCR system is slower. As long as the SCR system has not yet reached its operating temperature of approx. 200 °C, the SCR system operates at lower conversion rates, resulting in increased tailpipe NO_x emissions. When the operating temperature is reached, NO_x emissions are almost completely converted. In order to minimize disadvantages with regard to CO_2 emissions resulting from an increased EGR rate, we adjust the EGR rate only if the SCR system has not yet reached the stated operating temperature. In the WLTC tests considered herein, the SCR system reaches operating temperature after 825 seconds.

Supplementary Table 8: Comparison of FT fuel compositions from Neumann et al.[138] (FT low-oxygen, FT high-oxygen) and this study (HyFiT-20%, HyFiT-40%).

Fuel	**Weight fraction** %			
	C	H	O	S
FT low-oxygen [a]	84	15	1	0
HyFiT-20% [b]	82	15	2	0
FT high-oxygen [a]	79	15	6	0
HyFiT-40% [b]	80	15	5	0

[a] Adopted from Neumann et al.[138]
[b] This study.

Supplementary Note 11: Fuel usage: numerical results of combustion emissions

In Supplementary Figure 12, the chemical energy is shown that is required from diesel, HyFiT-20%, and HyFiT-40% over the test cycle. Numerical values of measured combustion-related CO_2, NO_x, and PM emissions are presented in Supplementary Table 9. Supplementary Figure 13 and Supplementary Figure 14 show PM and NO_x engine-out emissions as well as alternative figures for PM and NO_x tailpipe emissions.

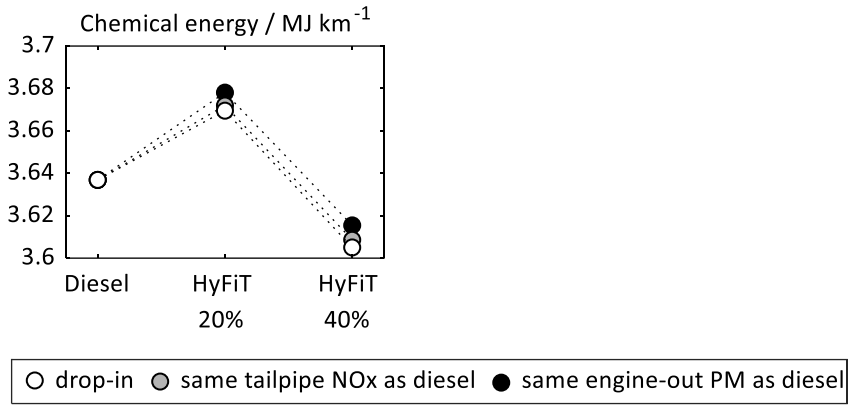

Supplementary Figure 12: Chemical energy required from diesel, HyFiT-20%, and HyFiT-40% over the test cycle. Related to Figure 5. Results are shown for three engine calibration cases: measured emissions from vehicle tests with the manufacturer's engine calibration (white circles) and estimated emissions of the HyFiT-fuels with an engine calibration that targets either the same tailpipe NO_X emissions as diesel (grey circles) or the same engine-out PM emissions as diesel (black circles).

Supplementary Table 9: Numerical values for combustion-related CO_2, NO_x, and particulate matter (PM) engine-out (EO) and tailpipe (TP) emissions of diesel, HyFiT-20%, and HyFiT-40%. Related to Figure 5.

	CO_2 g km^{-1}	**NO_x** mg km^{-1}		**PM** mg km^{-1}	
	TP	EO	TP	EO	TP
Diesel					
drop-in	267	318	24	51	0.34
HyFiT-20%					
drop-in	258	343	29	23	0.16
same tailpipe NO_x as diesel	258	333	22	24	0.17
same engine-out PM as diesel	259	323	16	28	0.20
HyFiT-40%					
drop-in	255	346	35	15	0.33
same tailpipe NO_x as diesel	255	331	23	17	0.38
same engine-out PM as diesel	256	320	15	21	0.47

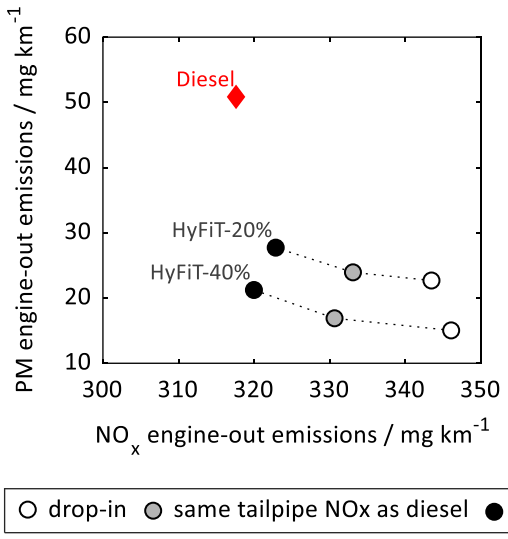

Supplementary Figure 13: Particulate matter (PM) over NO_x engine-out emissions from the combustion of diesel, HyFiT-20%, and HyFiT-40%. Related to Figure 5. Results are shown for three engine calibration cases: measured emissions from vehicle tests with the manufacturer's engine calibration, denoted as "drop-in," (white circles) and estimated emissions of HyFiT-fuels with an engine calibration that targets either the same tailpipe NO_x emissions (grey circles) or engine-out PM emissions as diesel (black circles). Note that, for the estimated emissions of HyFiT-fuels, the exhaust gas recirculation (EGR) rate is solely adjusted to lower NO_x emissions if the SCR system has not yet reached its operating temperature, i.e., for the first 825 seconds of the test cycle (see Supplementary Note 10). In the remaining test cycle time, the SCR system reduces NO_x emissions since it has reached its operating temperature; thus, no adjustment of the EGR rate is required. Consequently, overall PM engine-out emissions of HyFiT-fuels are lower than those of diesel for the "same engine-out PM as diesel" calibration. Numerical values of emissions are presented in Supplementary Table 9.

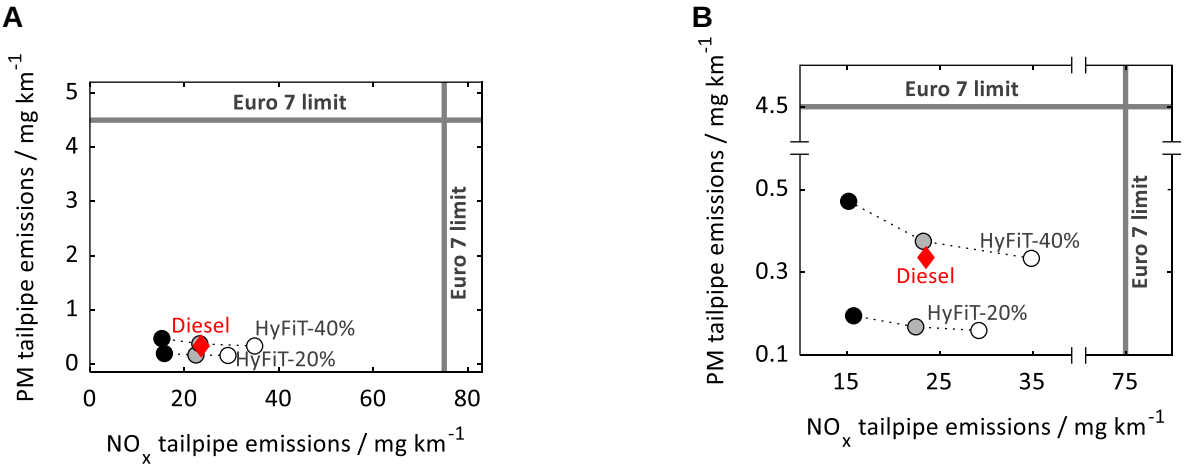

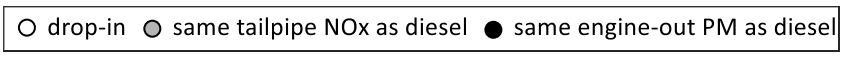

Supplementary Figure 14: (A) Particulate matter (PM) over NO_x tailpipe emissions from the combustion of diesel, HyFiT-20%, and HyFiT-40%. Related to Figure 5. In (B), emissions have a higher resolution due to the axes breaks. Results are shown for three engine calibration cases: measured emissions from vehicle tests with the manufacturer's engine calibration, denoted as "drop-in," (white circles) and estimated emissions of HyFiT-fuels with an engine calibration that targets either the same tailpipe NO_x emissions (grey circles) or engine-out PM emissions as diesel (black circles). Numerical values of emissions are presented in Supplementary Table 9.

Supplementary Note 12: Life cycle assessment (LCA)

In Supplementary Table 10, we show a list of the considered environmental impact categories of the "Environmental Footprint 3.0" framework. Thereafter, the life cycle inventory is described along with the LCA datasets presented in Supplementary Table 11.

Supplementary Table 10: List of considered environmental impact categories of the "Environmental Footprint 3.0" framework.[140]

Abbreviation	Impact category	Unit	Level of recommendation [a]
CF	Carbon footprint	kg CO_2 eq.	I
OD	Ozone depletion	kg CFC-11 eq.	I
PM	Particulate matter	disease incidence	I
A	Acidification	mol H^+ eq.	II
E_{fw}	Eutrophication, freshwater	kg P eq.	II
E_m	Eutrophication, marine	kg N eq.	II
E_t	Eutrophication, terrestrial	mol N eq.	II
IR	Ionizing radiation, human health	kBq U^{235} eq.	II
POF	Photochemical ozone formation	NMVOC eq.	II
ET	Ecotoxicity, freshwater	CTUe	III
HT_c	Human toxicity, carcinogenic	CTUh	III
HT_{nc}	Human toxicity, non-carcinogenic	CTUh	III
LU	Land use	points	III
RU_e	Resource use, energy carriers	MJ	III
RU_m	Resource use, minerals and metals	kg Sb eq.	III
WU	Water use	m^3 world eq.	III

[a] "Level I" is recommended and satisfactory, "Level II" is recommended but needs some improvements, and "Level III" is recommended but has to be applied with caution.[140]

Life cycle inventory. As feedstocks, we consider biomass and CO_2 for syngas production. For the supply of natural gas, process data from the LCA database ecoinvent is used.[141] As biomass feedstock, we use miscanthus as a perennial energy crop and second-generation biomass to avoid the "food versus fuel" conflict of first-generation biomass. Process data for miscanthus supply is taken from ecoinvent.[141] Note that we do not consider land-use change (LUC) emissions but present a sensitivity analysis in Supplementary Note 23. For CO_2 supply, we assume direct air capture (DAC) and include the energy requirements from the predicted energy targets of an industrial temperature swing adsorption DAC system of Deutz et al.[142] We give a credit for CO_2 that is used after removing it from the atmosphere by biomass growth (1.5 kg CO_2 eq. per kg miscanthus-used, according to the carbon content) or DAC (1.0 kg CO_2 eq. per kg CO_2-captured).[143] However, this CO_2 is released again during the combustion of the HyFiT-fuel, by-products, and purge gas streams, and is accounted for in the LCA.

As the FT synthesis and hydroformylation both require syngas as input, we incorporate the syngas production network by Bachmann et al.[121] Here, we give a concise summary of the most important aspects of this network and refer the reader to Bachmann et al. for an in-depth description. The network produces syngas from biomass or CO_2 at 30 bar with an H_2:CO ratio of 2:1, based on engineering-level data. Since the HT-FT synthesis and hydroformylation both require syngas with an H_2:CO ratio of 1:1, we model a ceramic membrane separation unit, removing excess H_2 by membrane permeation to lower the syngas' H_2:CO ratio (see Supplementary Note 3).

For fossil-based syngas, steam reforming and partial oxidation of methane are considered. In the case of steam methane reforming, syngas has an H_2:CO ratio of 3:1. This ratio is adjusted to 2:1 by either separating additional H_2 after the reactor (H_2 skimming) or feeding additional CO_2 to the reactor (CO_2 import). Bio-based syngas is either produced in a pressurized direct oxygen-steam blown circulating fluidized bed (CFB) or in an atmospheric indirect air-blown dual fluidized bed gasifier. The syngas' H_2:CO ratio is adjusted to 2:1 by water-gas shift or addition of H_2. For CO_2-based syngas, three technologies are considered: dry reforming of methane with CO_2 as co-reactant, reverse water-gas shift of CO_2 and H_2, and the Sabatier process for methane production from CO_2 and H_2. Methane from the Sabatier process is subsequently converted to syngas via steam reforming, partial oxidation, or dry reforming of methane.

Note that, in contrast to Bachmann et al., we do not consider high-temperature CO_2-electrolysis and co-electrolysis of CO_2 and water since both are still technologically immature for large-scale syngas production.[144] The co-reactant H_2 can be produced fossil-based or from renewables. While fossil-based H_2 is supplied via steam reforming of natural gas, renewable H_2 can be produced via three pathways: (1) by water electrolysis using low-carbon electricity or via renewable methane from the Sabatier reaction and its subsequent (2) steam reforming or (3) dry reforming (with CO

as a co-product). Process data for water electrolysis is taken from the polymer electrolyte membrane electrolysis by Bareiß et al.[145]

Our analysis considers a large-scale HyFiT-fuel production plant for which we neglect plant construction since environmental impacts of FT plants are mostly dominated by energy and feedstock demands.[61,68,72] Moreover, the scale-up analysis on FT plants by Cuéllar-Franca et al. underscores that environmental impacts due to plant construction decrease substantially with increasing plant capacity until they are even negligible for large-scale production capacities,[72] e.g., the Bintulu gas-to-liquid plant in Malaysia. We thus focus on the influence of energy and feedstock demands and only account for plant construction where it differs from conventional chemical productions (e.g., electrolyzers). Further scaling-effects on environmental impacts that might occur, e.g., through changes in heat integration and energy efficiency, are not considered since our first conceptual analysis focuses on developing and evaluating a suitable process concept. See Supplementary Note 3 for a detailed description of our HyFiT-fuel production model.

For cooling purposes, we distinguish between cooling water above 10 °C and refrigeration below 10 °C. Cooling water is modeled with process data from ecoinvent,[141] a specific heat capacity of 4.18 kJ kg^{-1} K^{-1}, and a maximum temperature increase of 10 K. Refrigeration is modeled by cryogenic coolers based on curve fit functions by Ladner et al.:[146] The electricity consumption to provide refrigeration is calculated as a function of the required refrigeration temperature.

Process heat demand is differentiated between heat below 100 °C, between 100 °C and 250 °C, and above 250 °C. We include fossil-based and power-to-heat technologies whose application depend on the temperature level of the heat demand. As fossil-based technologies, we consider generic natural gas boilers and steam production in the chemical industry, using process data from ecoinvent for both.[141] For power-to-heat, we assume electrode boilers with a power-to-heat efficiency of 95%[147] and heat pumps with a coefficient of performance of 3.28.[148] Note that we perform pinch-based heat integration (ΔT_{min} = 10 K) after supply chain optimization to minimize external heating and cooling demands.

Electricity is supplied either by the grid or wind power which serves as a best-case proxy for a future low-carbon grid. As a consequence, each kilowatt-hour of wind power is assumed to be directly used although, in reality, intermittent wind energy would require energy storage to ensure steady-state operation of CO_2 supply by direct air capture, syngas production from CO_2 and biomass, and fuel production. Note that forecasted electricity mixes can even become carbon-negative if carbon dioxide removal (CDR) technologies such as direct air carbon capture and storage (DACCS) are considered: Consistent with the current decarbonization target of the United States (US), Qiu et al. model the carbon footprint of the US grid mix as carbon-neutral in 2035 and even as low as -19 g CO_2 eq. kWh^{-1} thereafter,[149] using integrated assessment models with DACCS as CDR option. To capture systemic changes in the underlying electricity grid, we follow the approach by Reinert et al.[150] and model the EU grid mix in 2030 based on the "2 °C scenario" of the International Energy Agency.[151] Process data to model the EU grid mix 2030 and electricity from wind power is taken from ecoinvent.[141]

Driving the fully battery-electric van is modeled with the python package "carculator" of version 1.7.0 by Sacchi et al.[152] For this purpose, we evaluate a BEV in 2030 and adjust the parameters cargo and battery mass, such that a minimum driving range of 400 km is maintained. The total driving mass is adjusted to the 3.3 t of the van with internal combustion engine (ICE). The remaining parameters are left at default values. The most important default parameters are 200,000 lifetime kilometers for both the vehicle and the battery, 12,000 driven kilometers per year, an NMC-622 battery with a cell energy density of 0.3 kWh kg^{-1}, and China as the country of battery production. The adjustments lead to a modeled BEV with a battery weighing 680 kg and a capacity of 153 kWh, resulting in a driving range of 430 km. The electricity consumption for battery production and driving the van results in 0.051 MJ km^{-1} and 1.195 MJ km^{-1}, respectively. In Supplementary Note 22, battery lifetime and capacity are varied in sensitivity analyses.

For driving the van with ICE, we consider the LHV of HyFiT-fuel and diesel (see Figure 4A) and the required chemical energy per kilometer (see Supplementary Figure 12). Combustion-related CO_2, PM, and NO_x emissions are presented in Supplementary Note 11 and stem from our vehicle tests with diesel and additivated HyFiT-fuels described above. Note though that the environmental impacts of the fuel additive R655 are not considered since data on its production and composition is proprietary and thus lacking. However, the additive's contribution to the overall well-to-wheel environmental impacts can be expected to be negligible due to its low concentration of 2000 ppm in the fuel blend. For the battery of the hybrid van with ICE, we model a battery with a capacity of 14 kWh in the "carculator," leaving the remaining parameters again at default values. The electricity consumption for battery production results in 0.005 MJ km^{-1}. Note that the battery is recharged by fuel combustion at the end of a hybrid vehicle's test cycle. Therefore, for battery recharging, no electricity is consumed but additional fuel. Process data for the supply of fossil diesel is taken from ecoinvent.[141] For more details on the used LCA datasets, see Supplementary Table 11.

Supplementary Table 11: LCA datasets of the life cycle inventory.

Flow	Unit	Dataset [a]	Reference
Energy			
Electricity	MJ	Grid mix of the European Union in 2030 [b]	Reinert et al.[150]
		RoW: electricity production, wind, 1-3MW turbine, onshore	ecoinvent 3.5, cut-off[141]
Heat, below 100 °C	MJ	RER: steam production, as energy carrier, in chemical industry	ecoinvent 3.5, cut-off[141]
		Heat pump with a coefficient of performance of 3.28 [c]	David et al.[148]
Heat, 100-250 °C	MJ	RER: steam production, as energy carrier, in chemical industry	ecoinvent 3.5, cut-off[141]
		Electrode vessel with a power-to-heat efficiency of 95%	Müller et al.[147]
Heat, above 250 °C	MJ	RoW: heat production, natural gas, at boiler modulating >100kW	ecoinvent 3.5, cut-off[141]
		Electrode vessel with a power-to-heat efficiency of 95%	Müller et al.[147]
		Incineration of excess hydrogen [d]	
		Incineration of by-products and unconverted syngas	
Refrigeration	MJ	Cryogenic cooler	Ladner et al.[146]
Feedstocks			
Carbon dioxide	kg	Direct air capture system based on temperature swing adsorption [e]	Deutz et al.[142]
Miscanthus	kg	GLO: market for miscanthus, chopped	ecoinvent 3.5, cut-off[141]
Natural gas	kg	RoW: market for natural gas, high pressure	ecoinvent 3.5, cut-off[141]
Intermediates			
Carbon monoxide	kg	Dry reforming of methane [d]	Sternberg et al.[153]
		Reverse water-gas shift [d]	Sternberg et al.[153]
Hydrogen	kg	Water electrolysis, polymer electrolyte membrane	Bareiß et al.[145]
		Steam methane reforming [d]	IHS Markit[154]
		Dry reforming of methane, by-product [d]	Sternberg et al.[153]
Methane	kg	Sabatier process [d]	Agora[155]
		RoW: market for natural gas, high pressure	ecoinvent 3.5, cut-off[141]
Synthesis gas, 2:1	kg	Partial oxidation of methane [d]	IHS Markit[154]
		Steam methane reforming with H_2 skimming [d]	IHS Markit[154]
		Steam methane reforming with CO_2 import [d]	IHS Markit[154]
		Circulating fluidized bed gasifier [d]	Bachmann et al.[156]
		Dual fluidized bed gasifier [d]	Bachmann et al.[156]
Driving			
Transportation	km	Battery-electric van (2030, 3.3 t driving mass, 153 kWh battery capacity)	Sacchi et al.[152]
Battery	piece	Battery for battery-electric van (2030, 153 kWh battery capacity)	Sacchi et al.[152]
		Battery for hybrid van (2030, 14 kWh battery capacity)	Sacchi et al.[152]
Other			
Ash	kg	RoW: Treatment of wood ash mixture, pure, sanitary landfill	ecoinvent 3.5, cut-off[141]
Cooling water	kg	GLO: market for water, decarbonised, at user	ecoinvent 3.5, cut-off[141]
Diesel	kg	RoW: diesel production, low-sulfur	ecoinvent 3.5, cut-off[141]
Monoethanolamine	kg	GLO: market for monoethanolamine	ecoinvent 3.5, cut-off[141]
Oxygen	kg	Oxygen vapor via cryogenic air separation	IHS Markit[154]
Process water	kg	GLO: market for water, decarbonised, at user	ecoinvent 3.5, cut-off[141]
Steam	kg	Packaged gas boiler, from 'Heat, above 250 °C' or 'Heat, 90-250 °C' [d]	IHS Markit[154]
Vegetable oil methyl ester	kg	GLO: market for vegetable oil methyl ester	ecoinvent 3.5, cut-off[141]

[a] Abbreviations in ecoinvent dataset names: RER: Europe; GLO: global; RoW: Rest-of-the-World.

[b] Systemic changes in the underlying electricity grid are captured following the approach of Reinert et al.,[150] based on the "2 °C scenario" of the IEA[151] and process data from ecoinvent 3.5, cut-off.[141]

[c] The coefficient of performance is averaged from heat pumps built since 2006 with condenser temperatures of about 90 °C and evaporator temperatures between 9-15 °C, according to David et al.[148]

[d] Adopted from Bachmann et al.[121]

[e] Energy requirements are taken from the predicted energy targets by Deutz et al.[142]

Supplementary Note 13: LCA: used technologies of supply chain designs

Here, we describe the technologies of the feedstock-specific supply chain designs in Figure 7A. For minimal carbon footprints, HyFiT-fuel is produced bio-based via biomass gasification in a CFB gasifier with water-gas shift, CO_2-based via reverse water-gas shift and water electrolysis, and fossil-based via steam methane reforming with H_2 skimming. Carbon footprints are the highest if HyFiT-fuel is produced bio-based via biomass gasification in a CFB gasifier with addition of H_2, CO_2-based via methane from the Sabatier process followed by steam methane reforming with H_2 skimming, and fossil-based via steam methane reforming with CO_2 import.

Supplementary Note 14: LCA: carbon footprint minimization

In the following, we present the carbon footprints of HyFiT-20% with closed-gas-loop design and HyFiT-40% with both open-gas-loop and closed-gas-loop design (Supplementary Figure 15).

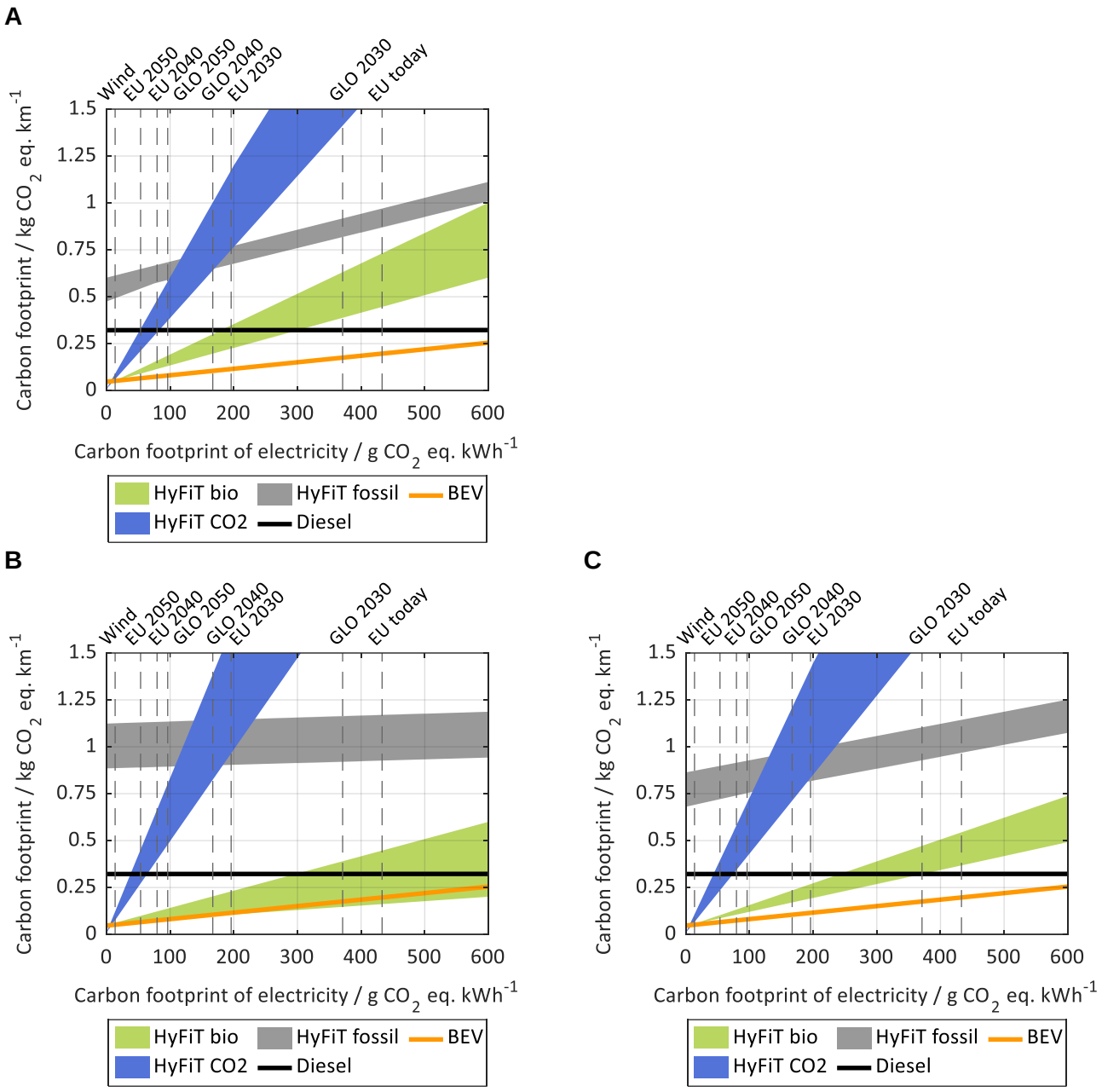

Supplementary Figure 15: The well-to-wheel carbon footprint of the van powered by bio-, CO_2-, or fossil-based HyFiT-fuel as function of the carbon footprint of electricity. Related to Figure 7A. Since there are multiple production routes for each feedstock, we show colored ranges for the feedstock-specific carbon footprints. The lower and upper margin of each range represents the supply chain with the lowest and highest carbon footprint. Benchmark results of diesel and the battery-electric van (BEV) are additionally shown. At the top, exemplary carbon footprints are shown for various electricity supplies. Results are shown for (A) HyFiT-20% with closed-gas-loop design, (B) HyFiT-40% with open-gas-loop design, and (C) HyFiT-40% with closed-gas-loop design. As engine calibration, "same engine-out PM as diesel" is considered (see Figure 5). EU: European Union; GLO: global.

Supplementary Note 15: LCA: carbon footprint minimization with limited inputs

If at least 0.43 kg km^{-1} of biomass is available, the optimal HyFiT-fuel is purely bio-based, regardless of whether electricity stems from the grid or renewables (Figure 7B, vertical line). The carbon footprint of 0.43 kg km^{-1} corresponds to 0.12 kg MJ_{fuel}^{-1}, which is at the lower end of recent studies on bio-based FT fuels (0.10-0.37 kg MJ_{fuel}^{-1}) and bioethanol (0.12-0.22 kg MJ_{fuel}^{-1}) (see Supplementary Note 17). With less than 0.43 kg km^{-1} of biomass but sufficient amounts of renewable electricity available, the optimal HyFiT-fuel is bio-hybrid, using both bio- and CO_2-based production routes (dashed curve). The HyFiT-fuel is purely CO_2-based if at least 17.5 MJ km^{-1} of renewable electricity and no biomass are available (circle). If both resources are unavailable, the HyFiT-fuel is produced purely fossil-based (square).

Electricity consumption of CO_2-based HyFiT-fuel can be reduced by 25% to 13.1 MJ km^{-1} with the closed instead of the open-gas-loop design. With the closed-gas-loop design, electricity for water electrolysis is reduced by 38% to 9.0 MJ km^{-1}, benefitting from H_2 in the recycled unconverted syngas. However, this benefit is partly offset by 1.5 MJ km^{-1} of additional electricity required for cryogenic separation in the closed-gas-loop design. Detailed process optimization might allow to further reduce the energy demand for HyFiT-fuel production.

Supplementary Note 16: LCA: environmental impacts beyond carbon footprint

As shown by Ordóñez et al. and Medrano-García et al.,[56,61] close-to-zero GHG emissions of FT fuels come at the cost of burden-shifting to other impact categories. For HyFiT-fuels, we therefore analyze a potential burden shift from carbon footprint to other environmental impacts in Supplementary Figure 16. Environmental impacts of HyFiT-fuels and diesel are normalized to those of the BEV. Here, we evaluate all carbon-footprint-optimal supply chains with electricity from wind power as a best-case proxy for a future low-carbon grid, and we present the results with electricity from the EU 2030 grid in Supplementary Figure 24. We list abbreviated impact categories in Supplementary Table 10 and present contribution analyses in Supplementary Note 18-21.

The HyFiT-fuels' and BEV's advantage of a close-to-zero carbon footprint comes at the cost of trade-offs in other impact categories. No single technology reduces all impact categories simultaneously. Compared to the BEV (yellow), bio-based HyFiT-fuel (green) is superior in terms of human toxicity (HT_{nc}, HT_c), resource use of minerals (RU_m), acidification (A), and freshwater eutrophication (E_{fw}). In the aforementioned impact categories, battery production is the major contributor for the BEV (see Supplementary Figure 18). Due to biomass cultivation and cooling water consumption, bio-based HyFiT-fuel is inferior for terrestrial and marine eutrophication (E_t, E_m), land use (LU), and water use (WU). The remaining impact categories are in the same range for bio-based HyFiT-fuel and the BEV. Environmental impacts of CO_2-based HyFiT-fuel (blue) are almost exclusively dominated by its large electricity consumption (see Supplementary Figure 18). CO_2-based HyFiT-fuel performs only better than its bio-based counterpart for eutrophication (E_{fw}, E_t, E_m), ecotoxicity (ET), and land use (LU).

In a sensitivity analysis, we decrease the BEV's battery lifetime and increase battery capacity, i.e., driving range, to evaluate the influence of both parameters on all impact categories (see Supplementary Figure 23). As expected, all impacts of the BEV increase. Yet, the largest increase is observed in resource use of minerals (RU_m) for lower battery lifetimes since more batteries are required and thus constructed per vehicle lifetime. Moreover, we find that the higher the required driving range, i.e., battery capacity of the BEV, the more superior are bio-based HyFiT-fuels: For driving ranges of at least 550 km, bio-based HyFiT-fuels have lower environmental impacts in 10-12 out of 16 impact categories (see Supplementary Figure 23B).

If electricity is supplied from the power grid instead of wind power, bio-based HyFiT-fuel performs even better than the BEV in five additional impact categories. However, with electricity from the power grid, CO_2-based HyFiT-fuel performs worst in all impact categories, except for the BEV in the impact category resource use of minerals (RU_m) (see Supplementary Figure 24).

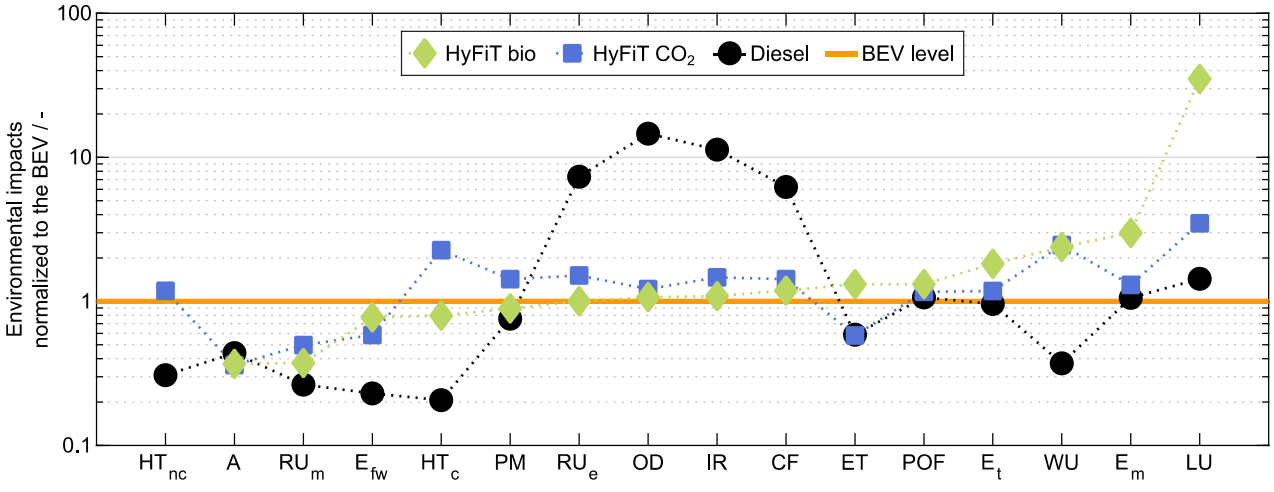

Supplementary Figure 16: The well-to-wheel environmental impacts of bio-based (green) and CO_2-based (blue) HyFiT-20% fuel and diesel (black) normalized to the environmental impacts of the battery-electric vehicle (BEV, yellow). Related to Figure 8.The impact categories on the x-axis are sorted by the normalized impacts of the bio-based HyFiT-fuel. Results are shown for the feedstock-specific optimal supply chain with electricity from wind power as a best-case proxy for a future low-carbon grid (see Figure 7A) and open gas loop as well as the engine calibration "same engine-out PM as diesel" (see Figure 5). For contribution analyses and a list of all abbreviated impact categories, see Supplementary Note 18-21 and Supplementary Table 10, respectively. See Supplementary Figure 23 and Supplementary Figure 24 for sensitivity analyses of the BEV's battery lifetime and capacity.

Supplementary Note 17: LCA: biomass consumption

In Supplementary Figure 17, we compare biomass consumption of bio-based HyFiT-fuel with recent studies on bio-based FT fuels and bioethanol. Numerical values of considered studies are listed in Supplementary Table 12.

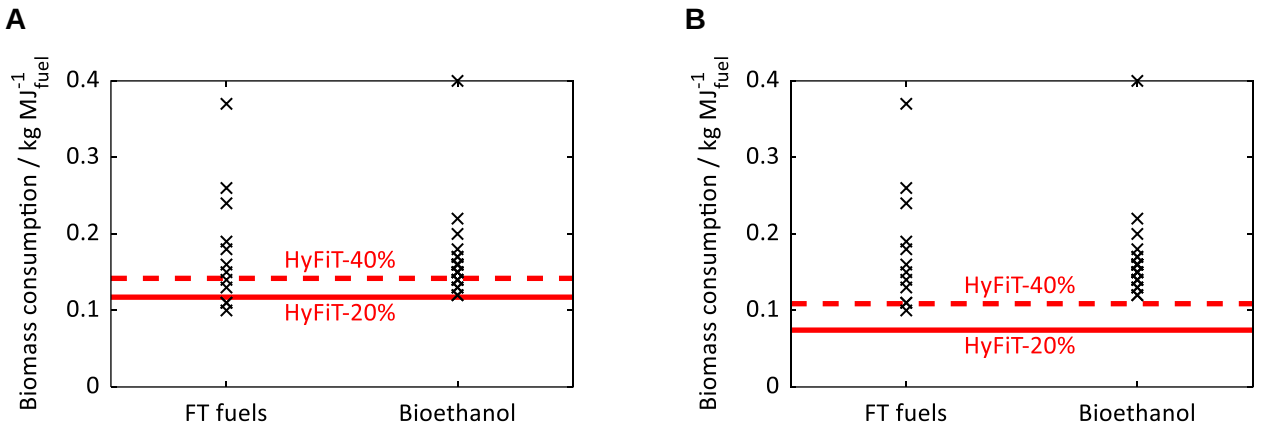

Supplementary Figure 17: Biomass consumption of bio-based HyFiT-20% (solid, red line) and HyFiT-40% (dashed, red line) compared to studies on FT fuels and bioethanol (X). Related to Figure 7B. For numerical values of biomass consumptions of FT fuels and bioethanol, see Supplementary Table 12. HyFiT-fuel is produced with (A) open or (B) closed gas loop.

Supplementary Table 12: Biomass consumption per MJ of fuel of HyFiT-fuels and derived from studies on FT fuels and bioethanol. Related to Supplementary Figure 17.

Fuel	Biomass consumption $kg_{biomass}$ MJ^{-1}_{fuel}	Author
HyFiT-20%		
Open gas loop	0.12	This study
Closed gas loop	0.07	This study
HyFiT-40%		
Open gas loop	0.14	This study
Closed gas loop	0.11	This study
FT fuel	0.37	Lundberg et al.[69]
	0.26	Okeke et al.[70]
	0.11	Dimitriou et al.[80]
	0.24	Neuling et al.[83]
	0.18	Neuling et al.[83]
	0.15	Zhang et al.[86]
	0.16	Albrecht et al.[87]
	0.13	Rafati et al.[92]
	0.14	Rafati et al.[92]
	0.10	Snehesh et al.[93]
	0.19	Snehesh et al.[93]
	0.11	Zhou et al.[95]
Bioethanol	0.17	Wang et al.[157]
	0.15	Wang et al.[157]
	0.16	Wang et al.[157]
	0.18	Wang et al.[157]
	0.16	Daylan et al.[158]
	0.16	González-García et al.[159]
	0.15	González-García et al.[159]
	0.12	González-García et al.[159]
	0.13	González-García et al.[160]
	0.14	Borrion et al.[161]
	0.40	Papong et al.[162]
	0.16	Sims et al.[163]
	0.20	Sassner et al.[164]
	0.22	Sassner et al.[164]
	0.16	Sassner et al.[164]
	0.15	Piccolo et al.[165]
	0.16	da Silva et al.[166]
	0.14	Gnansounou et al.[167]
	0.15	Gnansounou et al.[167]

Supplementary Note 18: LCA: contribution analysis of HyFiT-20%, electricity from wind power

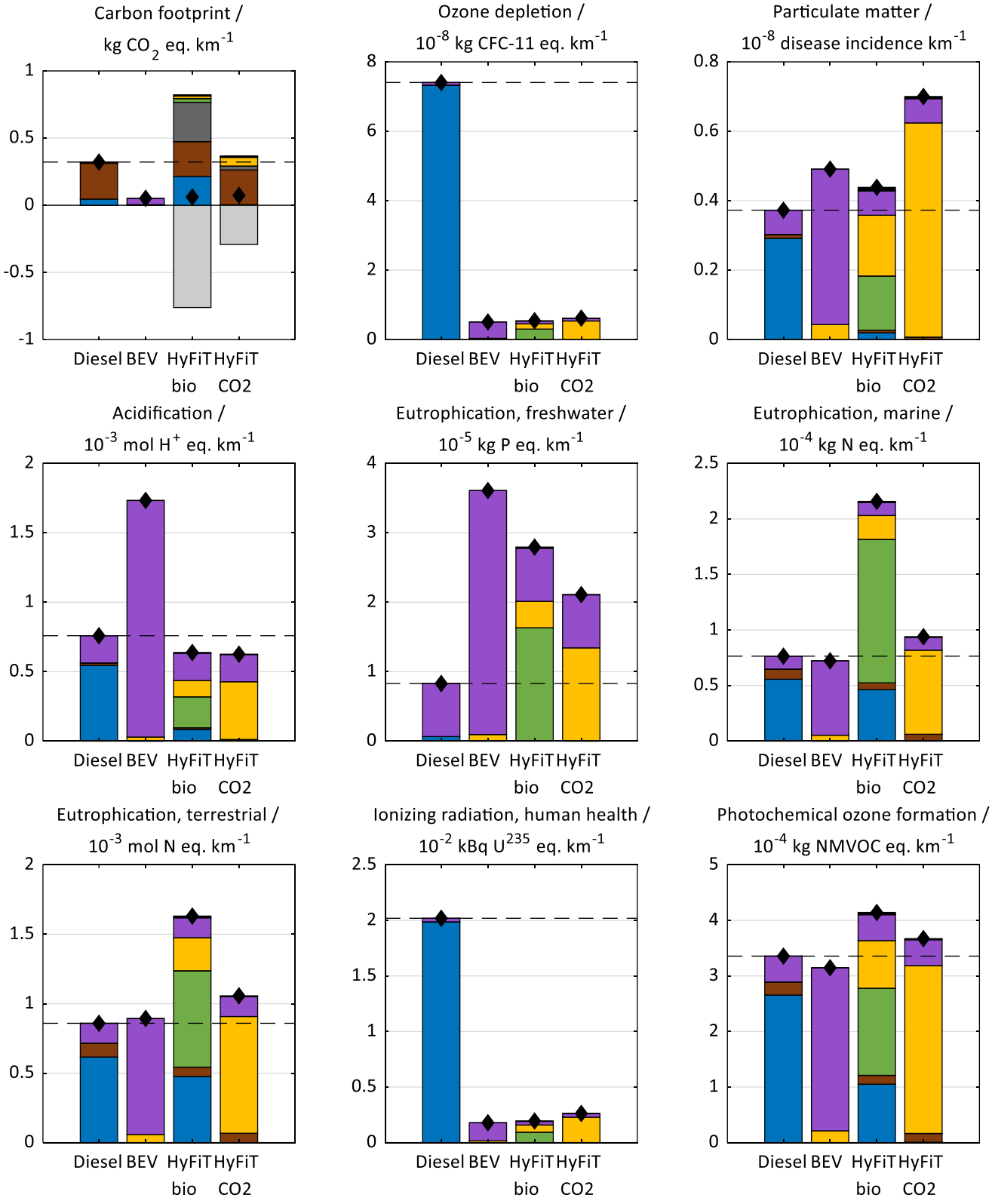

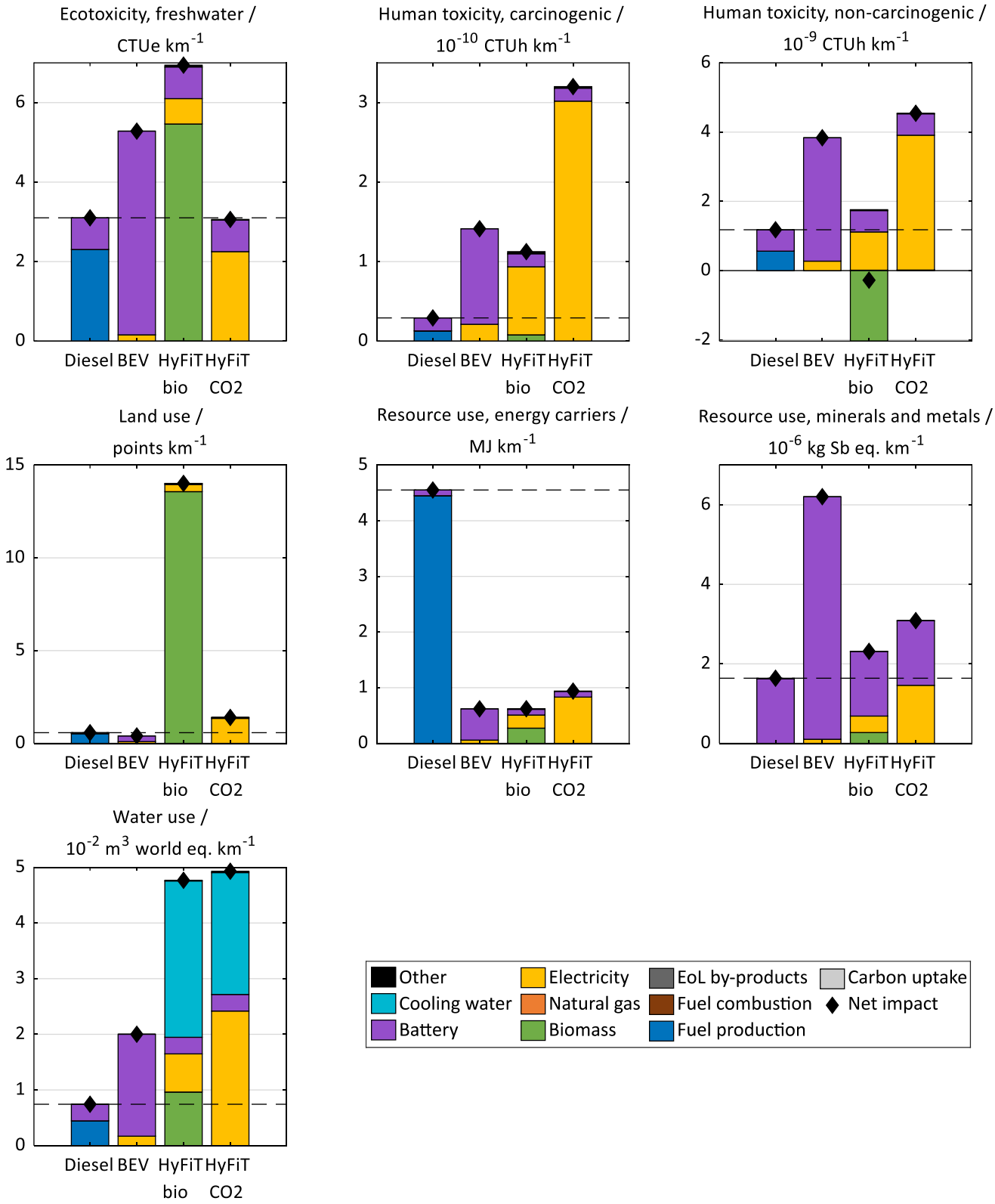

Supplementary Figure 18: Contribution analyses for the well-to-wheel environmental impacts of the benchmarks diesel and battery-electric vehicle (BEV) as well as bio- and CO_2-based HyFiT-20%. Related to Supplementary Figure 16. The results are shown for the feedstock-specific optimal supply chain with electricity from wind power (see Figure 7A), open-gas-loop design, and the engine calibration "same engine-out PM as diesel" (see Figure 5). For the ease of comparison, the dashed, horizontal line indicates the environmental impact of diesel, and the net impact is shown as black diamond.

Supplementary Note 19: LCA: contribution analysis of HyFiT-20%, electricity from the grid

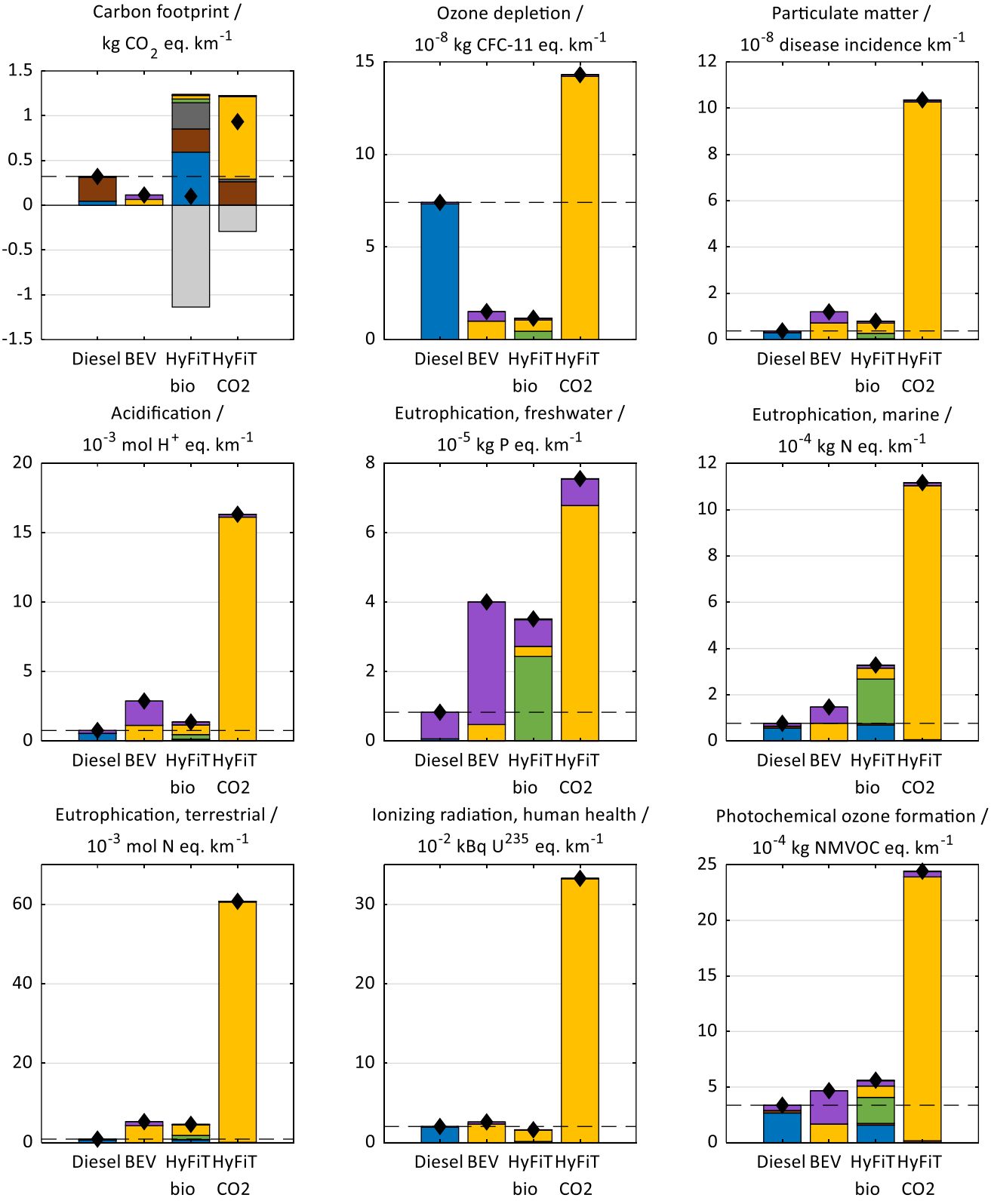

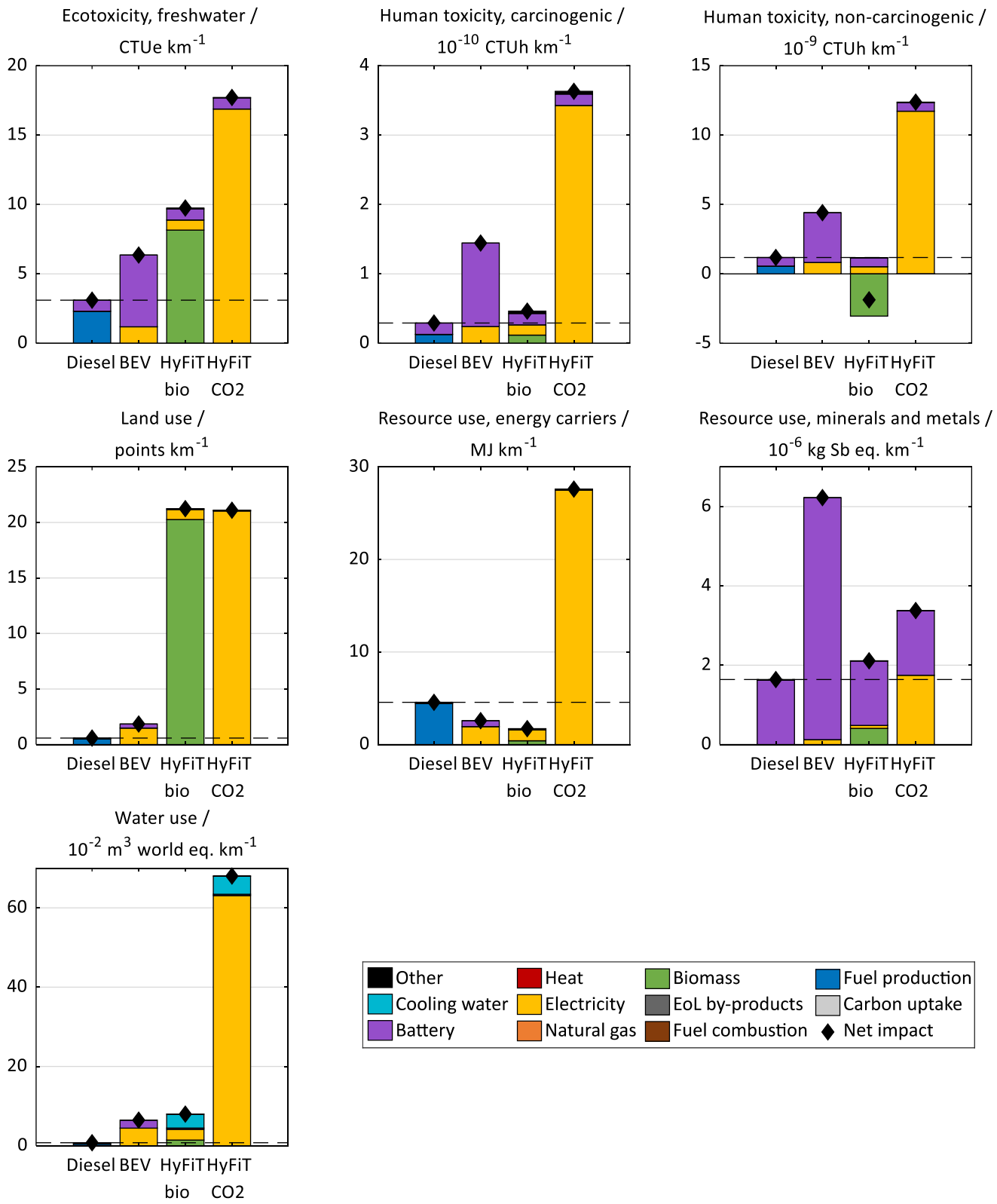

Supplementary Figure 19: Contribution analyses for the well-to-wheel environmental impacts of the benchmarks diesel and battery-electric vehicle (BEV) as well as bio- and CO_2-based HyFiT-20%. Related to Supplementary Figure 24. The results are shown for the feedstock-specific optimal supply chain with electricity from the EU power grid 2030 (see Figure 7A), open-gas-loop design, and the engine calibration "same engine-out PM as diesel" (see Figure 5). For the ease of comparison, the dashed, horizontal line indicates the environmental impact of diesel, and the net impact is shown as black diamond.

Supplementary Note 20: LCA: contribution analysis of HyFiT-40%, electricity from wind power

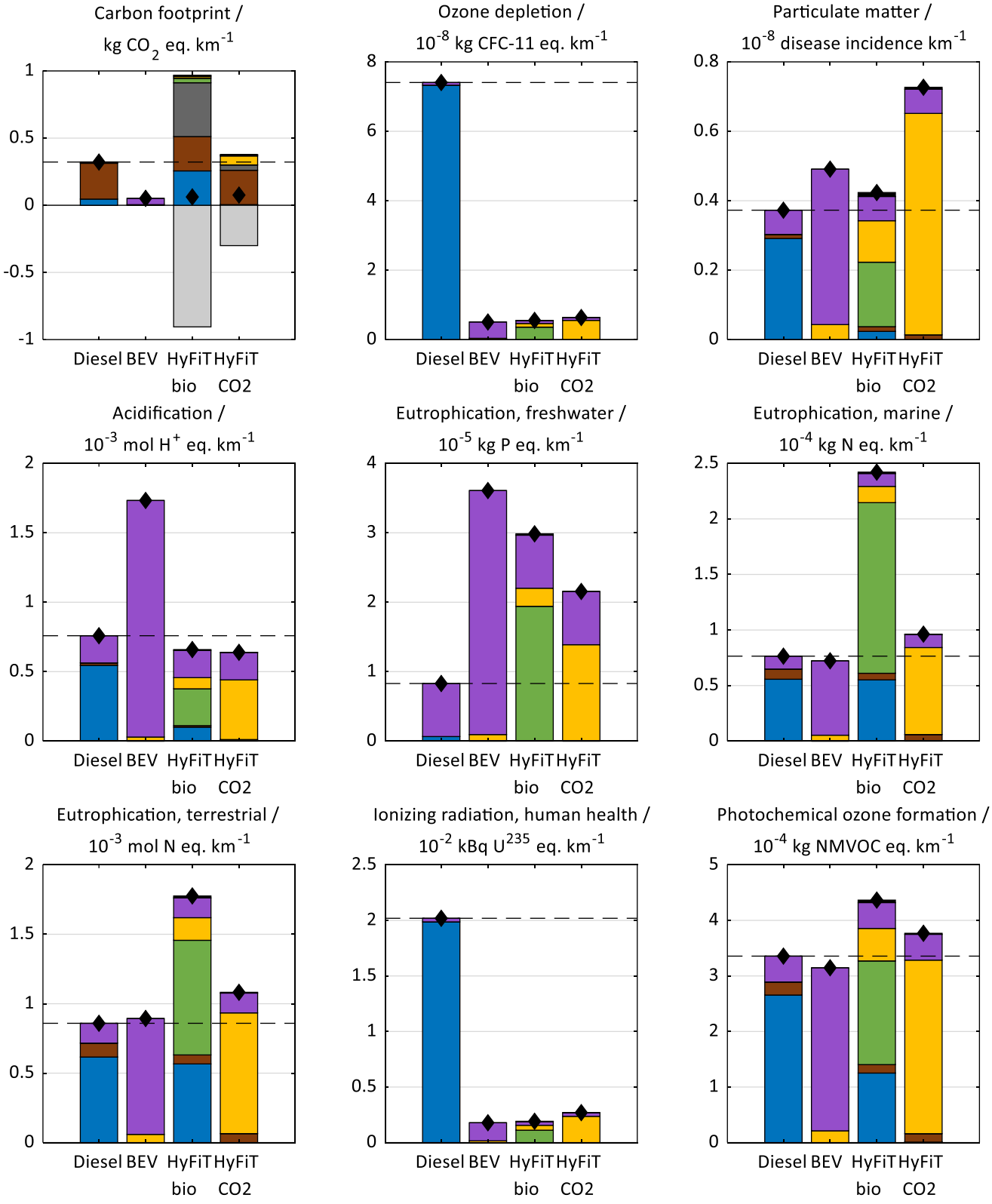

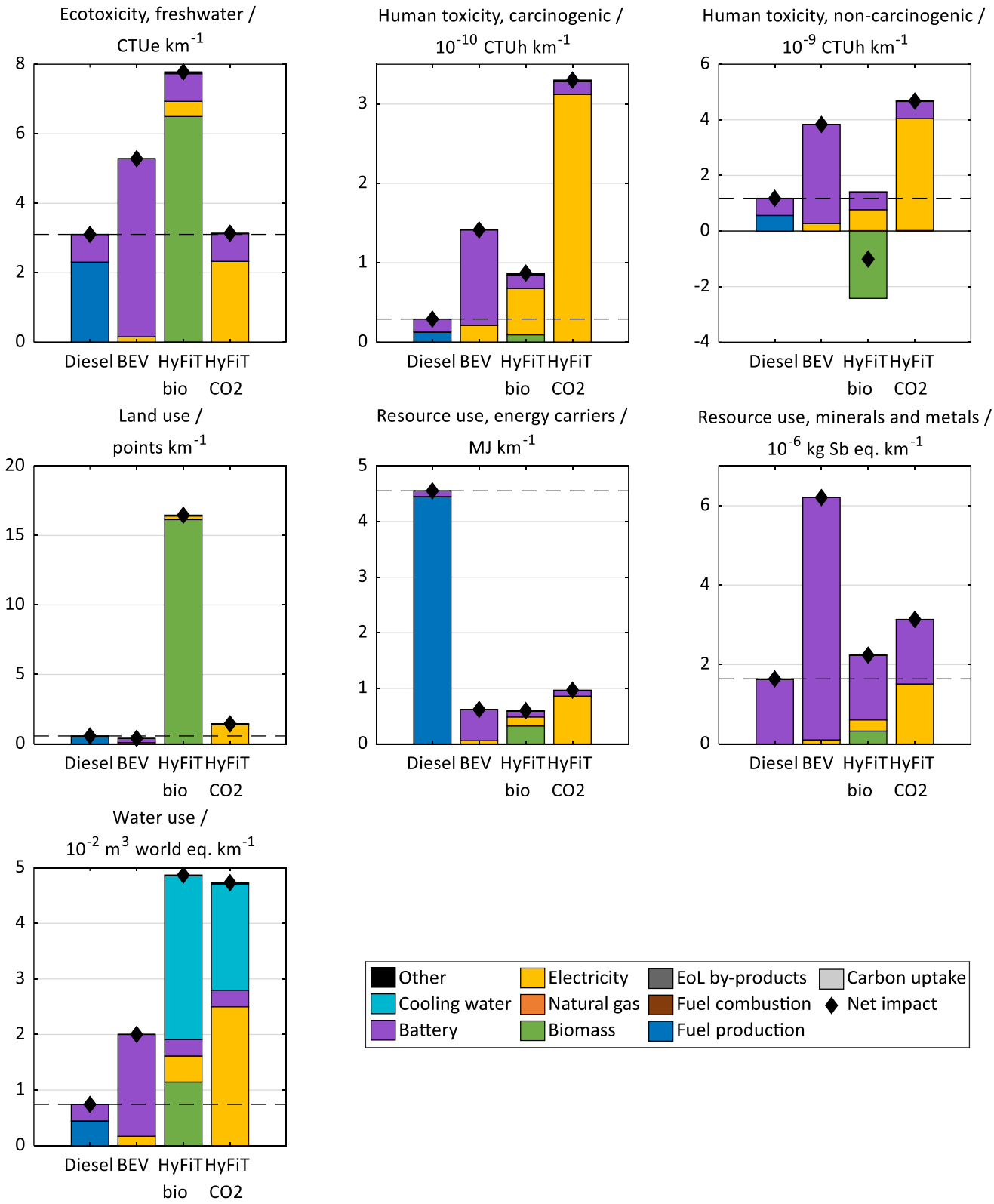

Supplementary Figure 20: Contribution analyses for the well-to-wheel environmental impacts of the benchmarks diesel and battery-electric vehicle (BEV) as well as bio- and CO_2-based HyFiT-40%. Related to Supplementary Figure 16. The results are shown for the feedstock-specific optimal supply chain with electricity from wind power (see Supplementary Figure 15B), open-gas-loop design, and the engine calibration "same engine-out PM as diesel" (see Figure 5). For the ease of comparison, the dashed, horizontal line indicates the environmental impact of diesel, and the net impact is shown as black diamond.

Supplementary Note 21: LCA: contribution analysis of HyFiT-40%, electricity from the grid

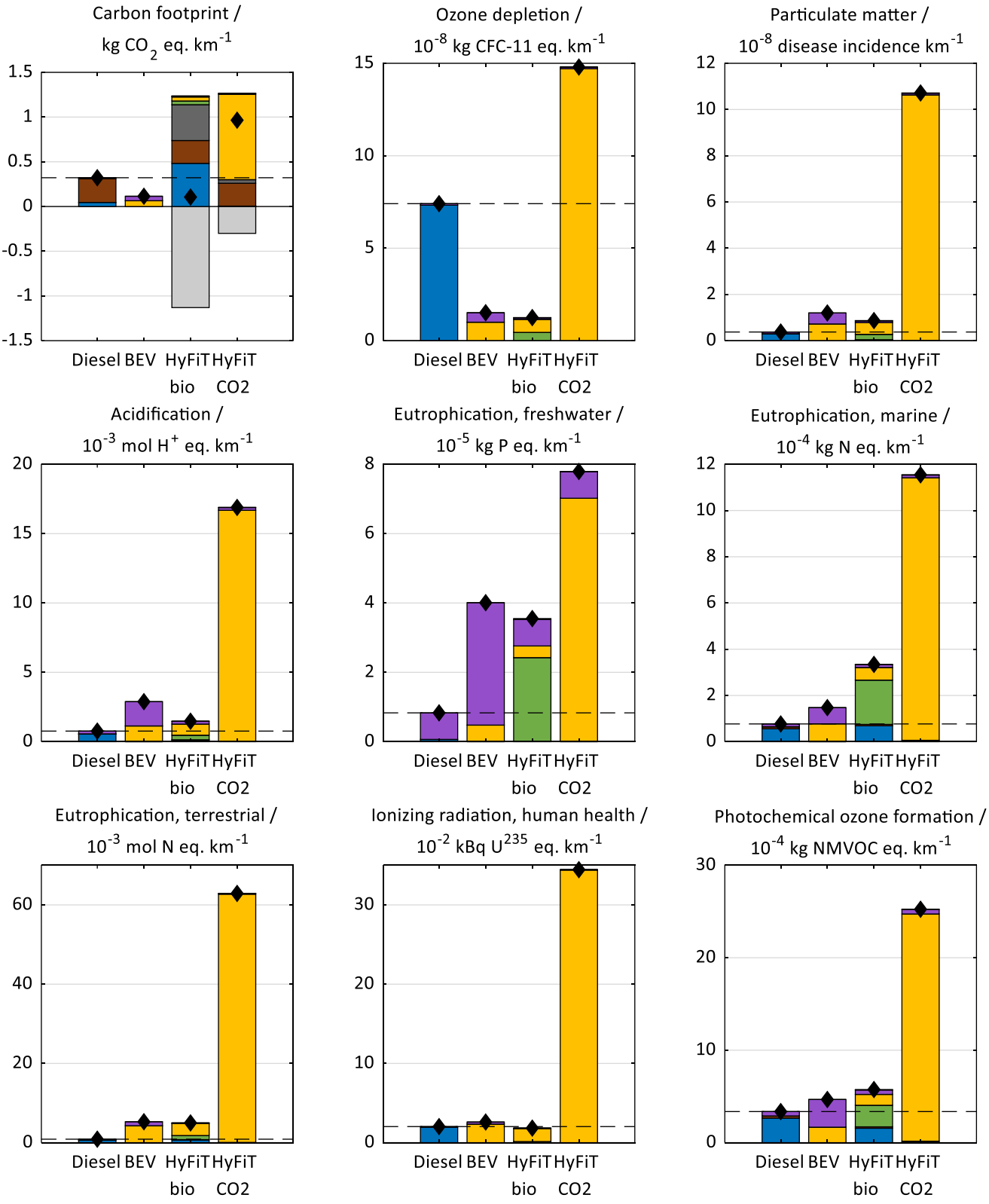

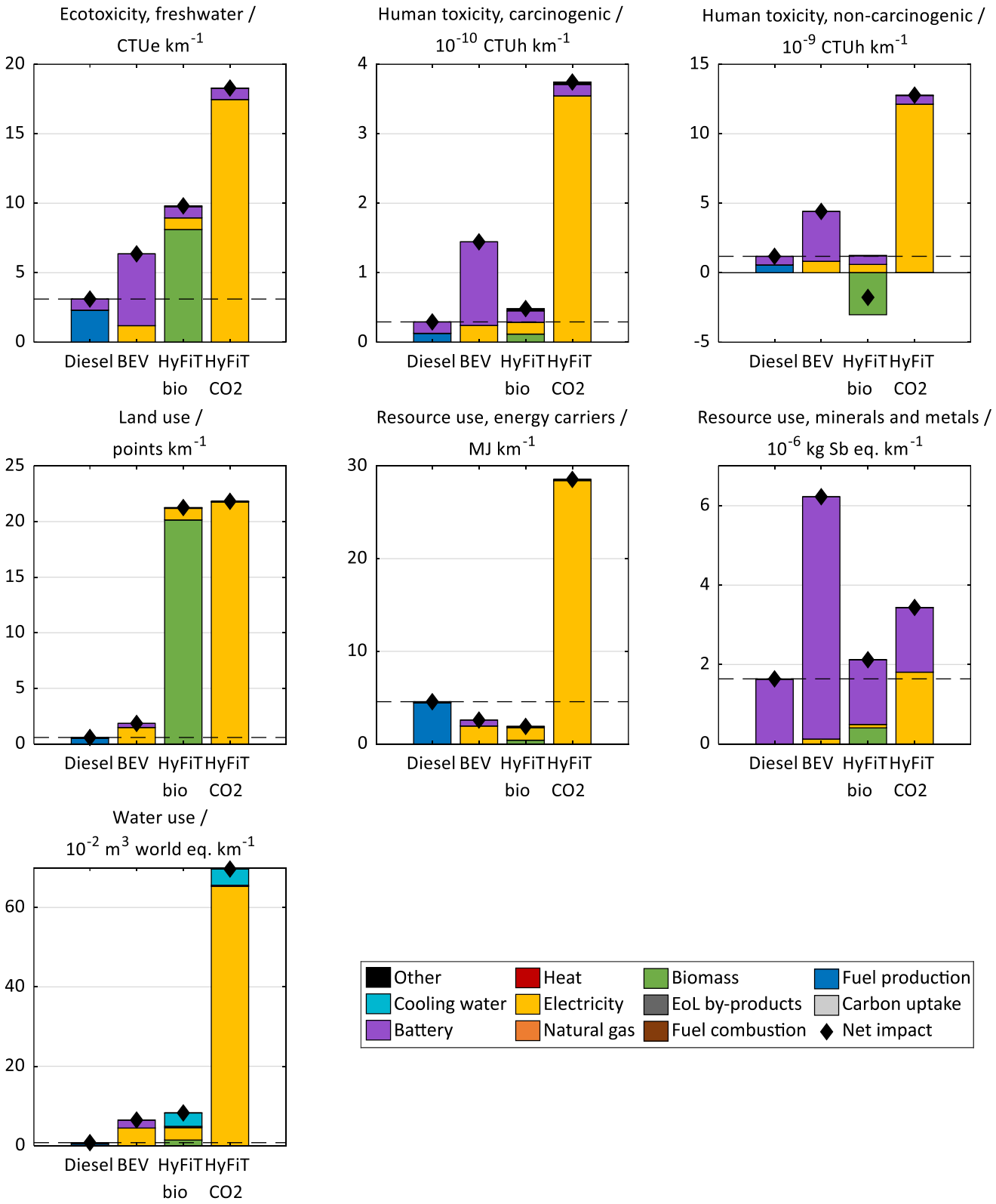

Supplementary Figure 21: Contribution analyses for the well-to-wheel environmental impacts of the benchmarks diesel and battery-electric vehicle (BEV) as well as bio- and CO_2-based HyFiT-40%. Related to Supplementary Figure 24. The results are shown for the feedstock-specific optimal supply chain with electricity from the EU power grid 2030 (see Supplementary Figure 15B), open-gas-loop design, and the engine calibration "same engine-out PM as diesel" (see Figure 5). For the ease of comparison, the dashed, horizontal line indicates the environmental impact of diesel, and the net impact is shown as black diamond.

Supplementary Note 22: LCA: sensitivity analysis of battery-electric van

Here, we present the sensitivity analysis for the BEV's battery lifetime and capacity. We vary the battery lifetime and capacity in Supplementary Figure 22 to assess the sensitivity of the BEV's carbon footprint towards both parameters. In this sensitivity analysis, battery lifetime is reduced from 200,000 km (default) to 100,000 and 50,000 km, requiring two to four batteries instead of one battery per vehicle lifetime of 200,000 km (default). Separately, battery capacity is increased from 153 kWh (default) to 200 and 300 kWh, accounting for higher driving ranges of 562 to 843 km instead of 430 km (default). With increases of 0.04-0.07 kg CO_2 eq. km^{-1}, both parameters have only minor influence on the carbon footprint of the BEV. However, the BEV's carbon footprint increases substantially by 0.14-0.19 kg CO_2 eq. km^{-1} if a battery lifetime of 50,000 km and battery capacity of 300 kWh are considered simultaneously.

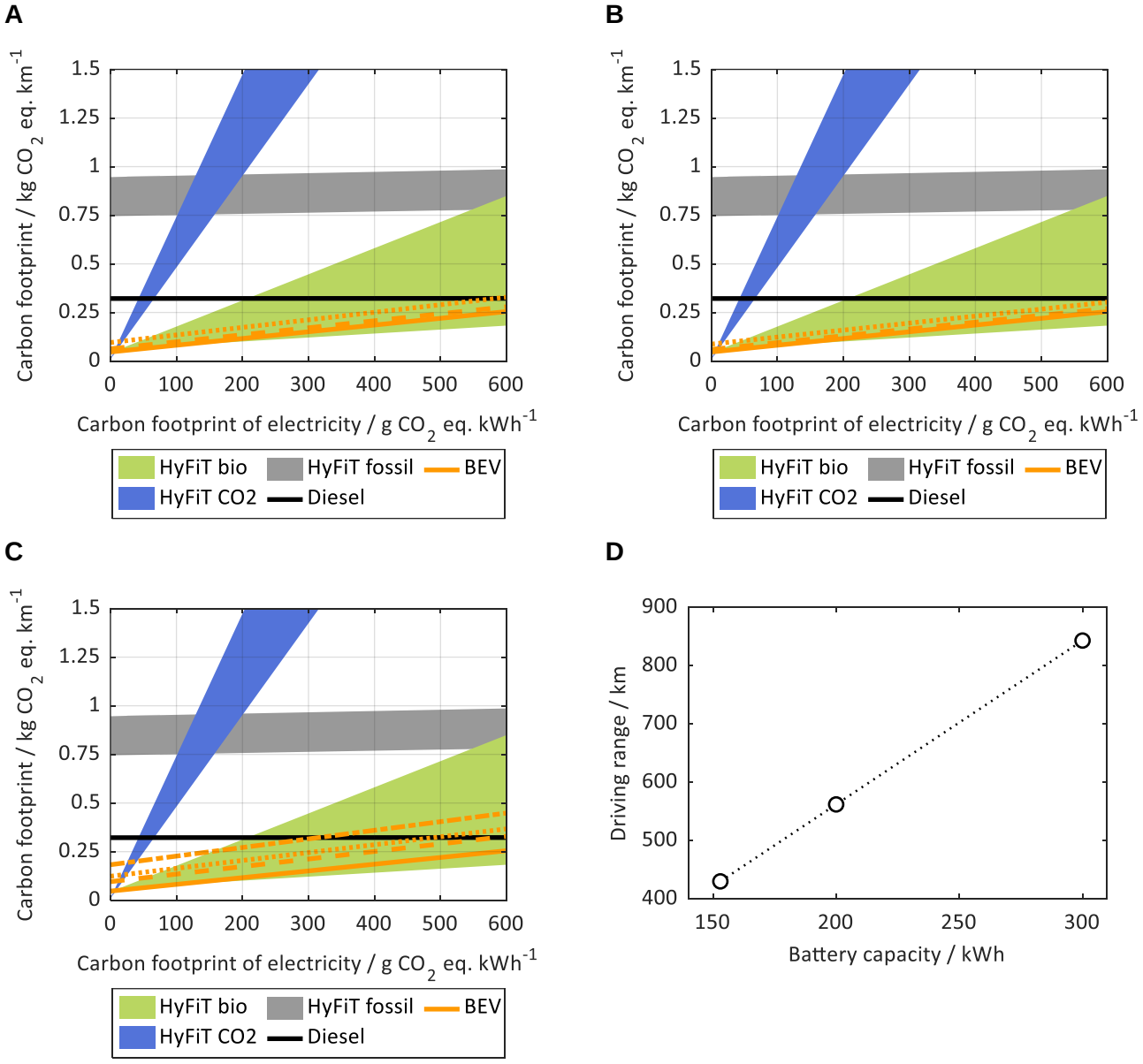

Supplementary Figure 22: Sensitivity analysis of the well-to-wheel carbon footprint of the battery-electric van (BEV) as function of the carbon footprint of electricity. Related to Figure 7A. In all sensitivity analyses, the total BEV driving mass of 3.3 t is maintained for consistency with the testing vehicle (see Supplementary Note 10). The default BEV (battery lifetime of 200,000 km, battery capacity of 153 kWh) is shown as solid yellow line. (A) Battery lifetime is varied to 100,000 km (dashed) and 50,000 km (dotted), with default battery capacity. (B) Battery capacity is varied to 200 kWh (dashed) and 300 kWh (dotted), with default battery lifetime. (C) Battery capacity is varied to 153 kWh (dashed), 200 kWh (dotted), and 300 kWh (dash-dotted), with a battery lifetime of 50,000 km. (D) Driving range of the BEV as function of the battery capacity.

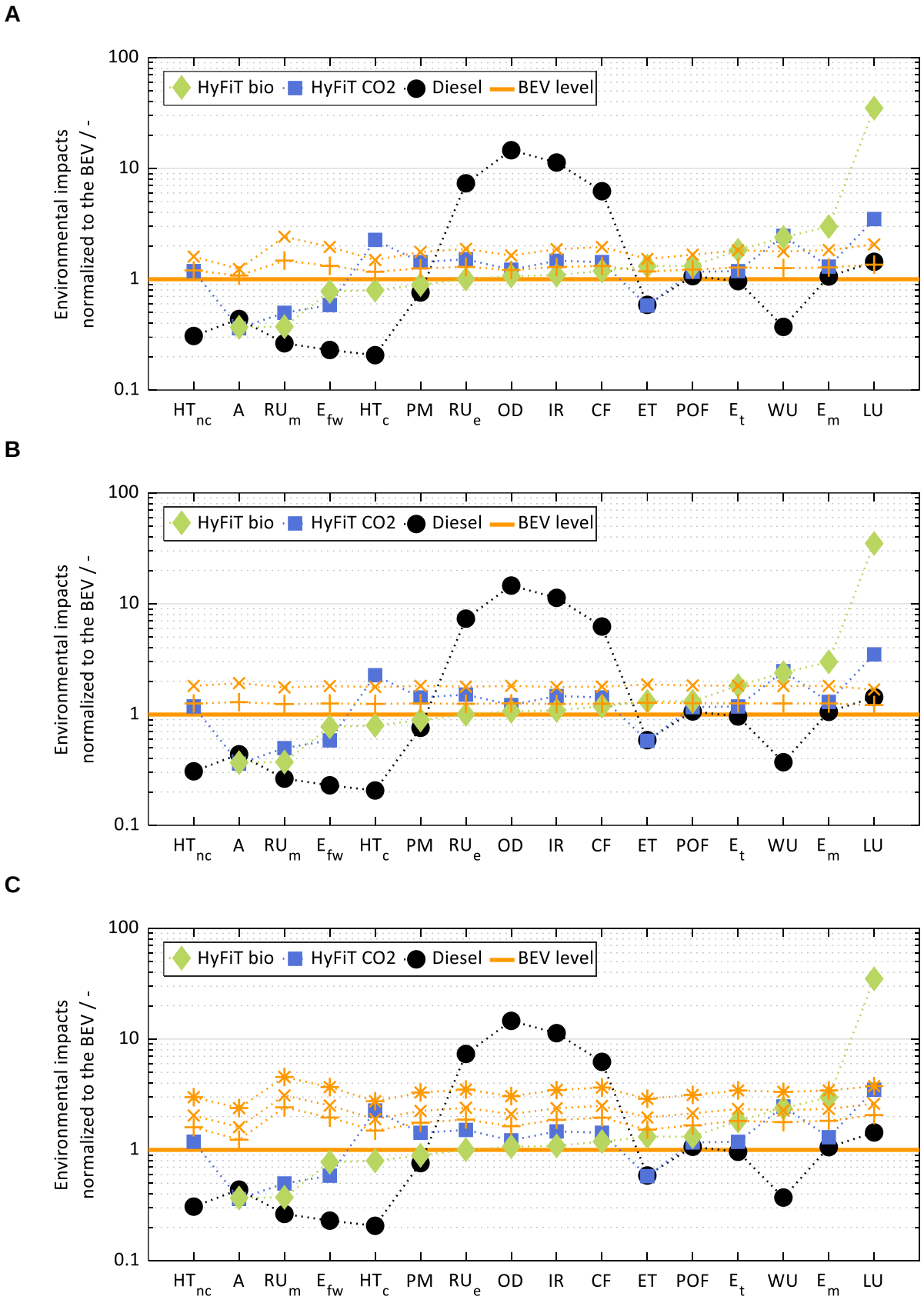

Supplementary Figure 23: Sensitivity analysis of the well-to-wheel environmental impacts of the battery-electric van (BEV) normalized to the environmental impacts of the default BEV. Related to Figure 7A. Results are shown for electricity from wind power. In all sensitivity analyses, the total BEV driving mass of 3.3 t is maintained for consistency with the testing vehicle. The default BEV (battery lifetime of 200,000 km, battery capacity of 153 kWh) is shown as solid yellow line. (A) Battery lifetime is varied to 100,000 km (plus) and 50,000 km (x), with default battery capacity. (B) Battery capacity is varied to 200 kWh (plus) and 300 kWh (x), with default battery lifetime. (C) Battery capacity is varied to 153 kWh (plus), 200 kWh (x), and 300 kWh (asterisk), with a battery lifetime of 50,000 km.

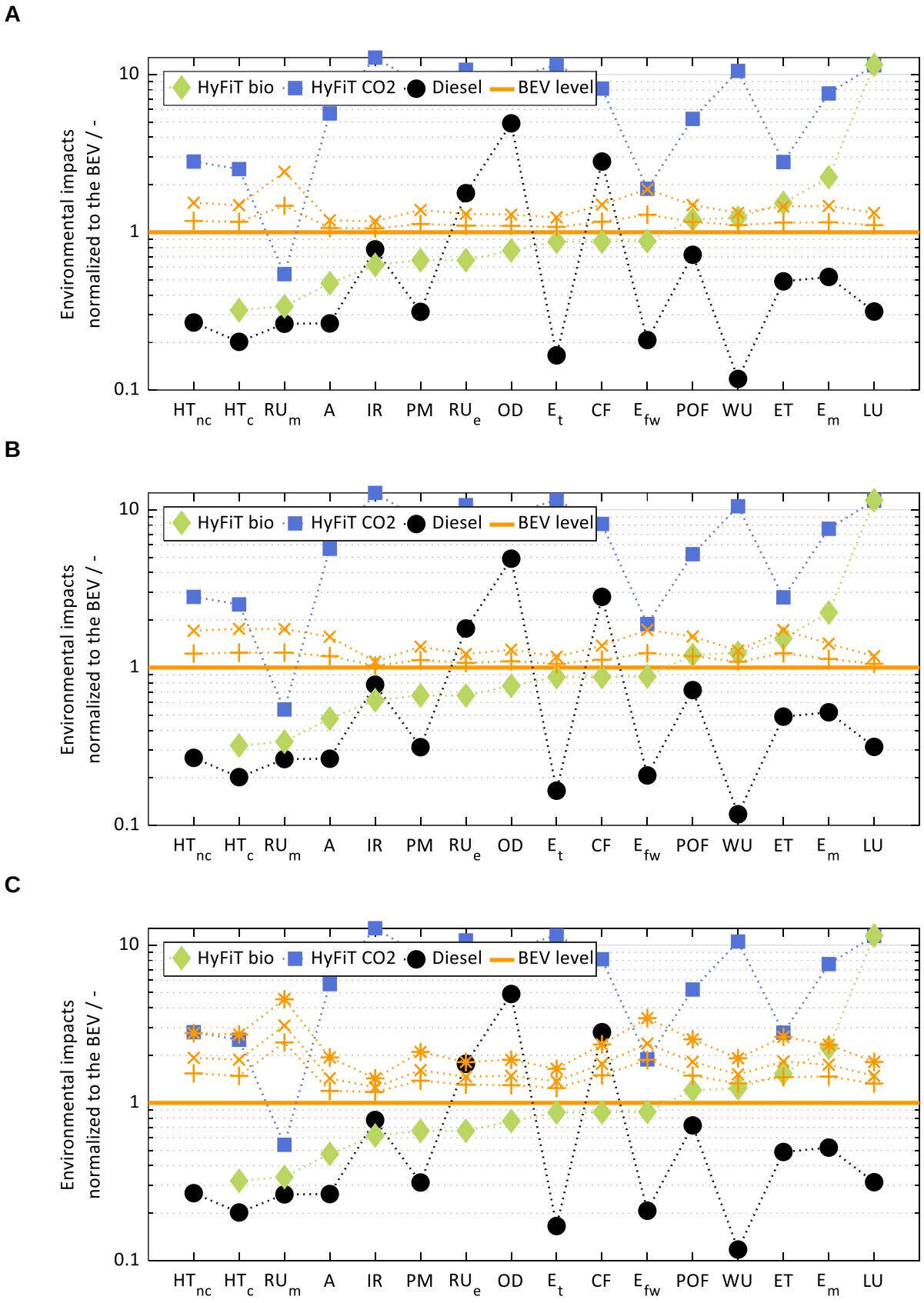

Supplementary Figure 24: Sensitivity analysis of the well-to-wheel environmental impacts of the battery-electric van (BEV) normalized to the environmental impacts of the default BEV. Related to Figure 7A. Results are shown for electricity from the EU 2030 power grid. In all sensitivity analyses, the total BEV driving mass of 3.3 t is maintained for consistency with the testing vehicle. The default BEV (battery lifetime of 200,000 km, battery capacity of 153 kWh) is shown as solid yellow line. (A) Battery lifetime is varied to 100,000 km (plus) and 50,000 km (x), with default battery capacity. (B) Battery capacity is varied to 200 kWh (plus) and 300 kWh (x), with default battery lifetime. (C) Battery capacity is varied to 153 kWh (plus), 200 kWh (x), and 300 kWh (asterisk), with a battery lifetime of 50,000 km.

Supplementary Note 23: LCA: sensitivity analysis of land-use change emissions

In the optimization in Figure 7A, we do not consider land-use change (LUC) emissions for biomass but present a sensitivity analysis for these LUC emissions in the following. In this sensitivity analysis, we vary LUC emissions from -0.15 to 0.10 kg CO_2 eq. per kg of biomass. We derived this range from the carbon calculator for LUC from biofuels production that is part of the GREET model by the Argonne National Laboratory.[168] Overall, LUC emissions have only minor influence on the carbon footprint of bio-based HyFiT-fuel: LUC emissions add GHG emissions in the range of -0.07 to 0.04 kg CO_2 eq. km^{-1} to the overall carbon footprint. Thus, the overall carbon footprint of bio-based HyFiT-fuel is still in the range of the BEV, but can even become negative for clean electricity supplies and negative LUC emissions. Note though that LUC emissions are subject to uncertainty.

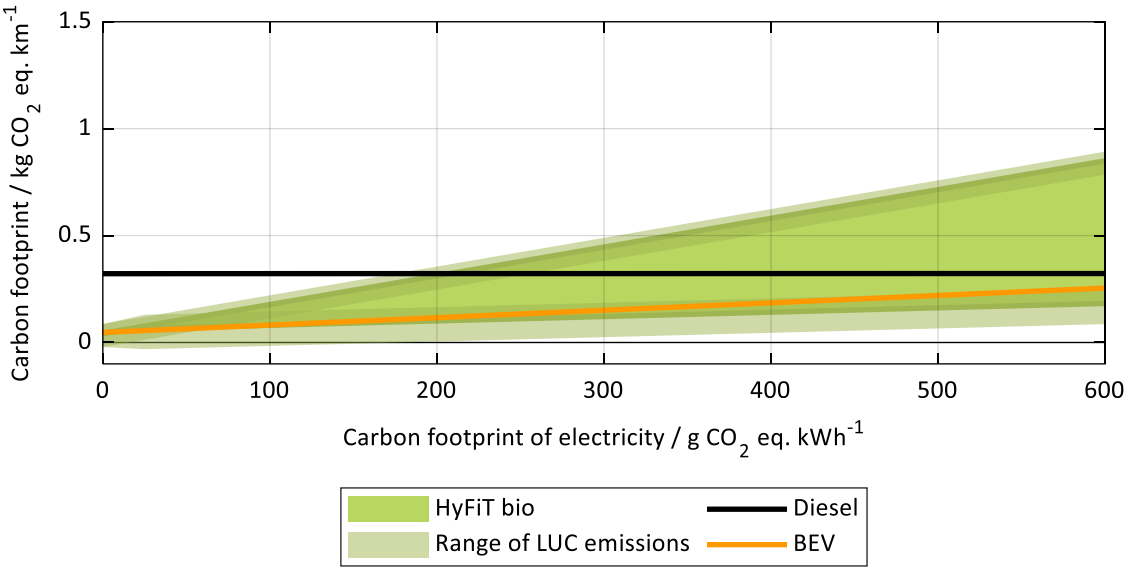

Supplementary Figure 25: The well-to-wheel carbon footprint of the van powered by bio-based HyFiT-fuel as function of the carbon footprint of electricity. Related to Figure 7A. Benchmark results of diesel and the battery-electric van (BEV) are additionally shown. The range of varied land-use change (LUC) emissions of biomass is depicted in light green.

Supplementary Note 24: LCA: sensitivity analysis of the removal of aromatics and oxygenates

As described in Supplementary Note 3, we estimate the removal of aromatics and oxygenates during HyFiT-fuel production with proxy process data. We thus quantify the degree of uncertainty that our estimation implies on the carbon footprint of HyFiT-fuels by varying the quantity and temperature level of heat consumption of the proxy process. For all variations of quantity and temperature level of heat consumption, the feedstock-specific supply chain is again optimized for minimal carbon footprint, followed by pinch-based heat integration. The carbon footprints of the supply chain optimizations with varied parameters are presented as heatmap and relative to the carbon footprint of the base case. For reference, we also present the average and the maximum heat consumption of EU refineries[169] and the boiling temperature range of vacuum gas oil (VGO)[170] as dashed vertical and horizontal lines, respectively.

The sensitivity analysis shows that the carbon footprint of HyFiT-fuels is only slightly sensitive towards the amount and temperature level of heat consumption of the proxy process. The largest increase is observed for the carbon-footprint-optimal supply chain of bio-based HyFiT-fuel with electricity from the EU 2030 power grid (Supplementary Figure 27). In this case, the carbon footprint is increased by 14% to 0.114 kg CO_2 eq. km^{-1}.

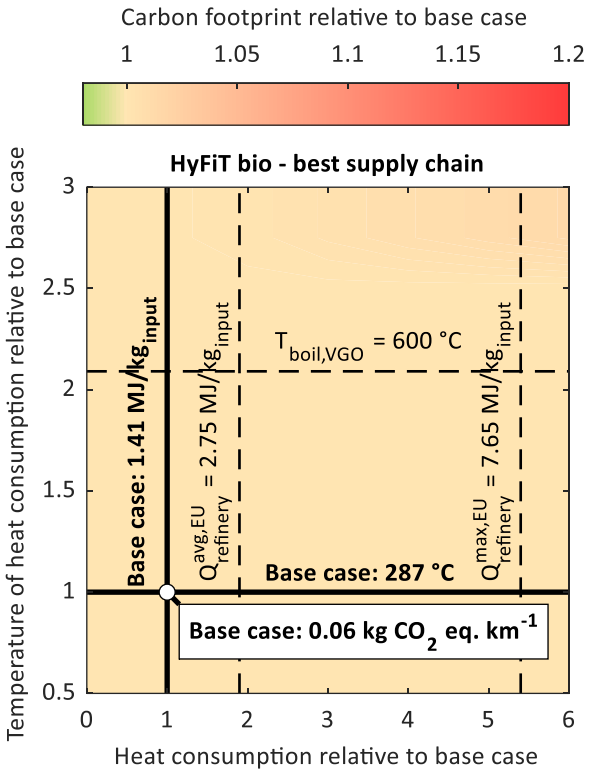
Carbon footprint relative to base case
1
1.05
1.1
1.15
1.2
HyFiT bio - best supply chain
Temperature of heat consumption relative to base case
Heat consumption relative to base case
Base case: 1.41 MJ/kg_input
Q^avg,EU_refinery = 2.75 MJ/kg_input
Q^max,EU_refinery = 7.65 MJ/kg_input
T_boil,VGO = 600 °C
Base case: 287 °C
Base case: 0.06 kg CO2 eq. km-1

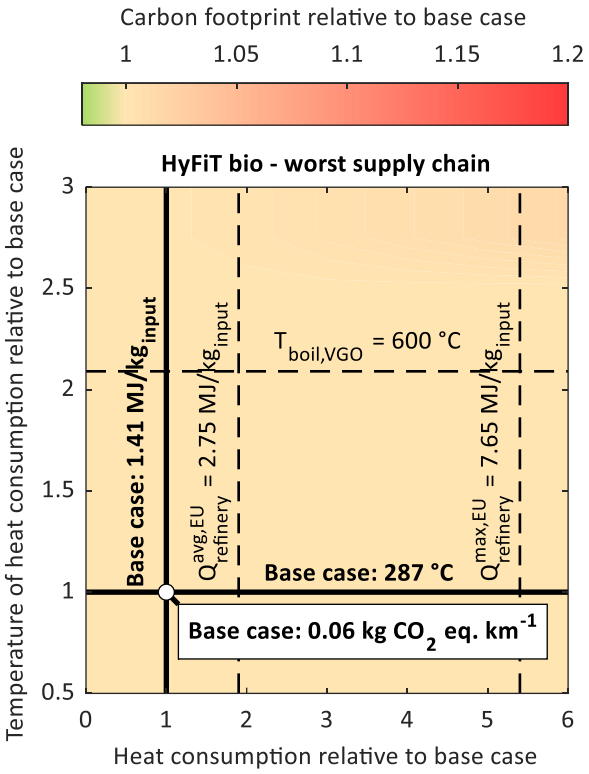
Carbon footprint relative to base case
1
1.05
1.1
1.15
1.2
HyFiT bio - worst supply chain
Temperature of heat consumption relative to base case
Heat consumption relative to base case
Base case: 1.41 MJ/kg_input
Q^avg,EU_refinery = 2.75 MJ/kg_input
Q^max,EU_refinery = 7.65 MJ/kg_input
T_boil,VGO = 600 °C
Base case: 287 °C
Base case: 0.06 kg CO2 eq. km-1

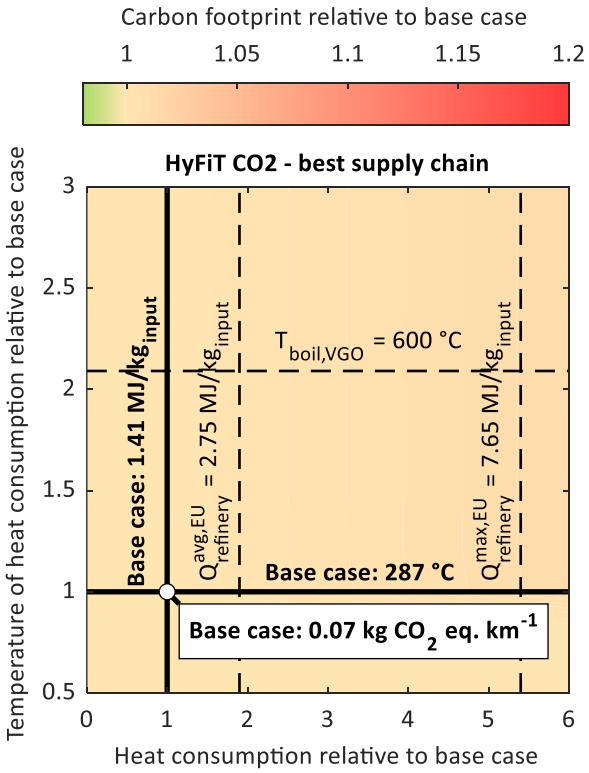
Carbon footprint relative to base case
1
1.05
1.1
1.15
1.2
HyFiT CO2 - best supply chain
Temperature of heat consumption relative to base case
Heat consumption relative to base case
Base case: 1.41 MJ/kg_input
Q^avg,EU_refinery = 2.75 MJ/kg_input
Q^max,EU_refinery = 7.65 MJ/kg_input
T_boil,VGO = 600 °C
Base case: 287 °C
Base case: 0.07 kg CO2 eq. km-1

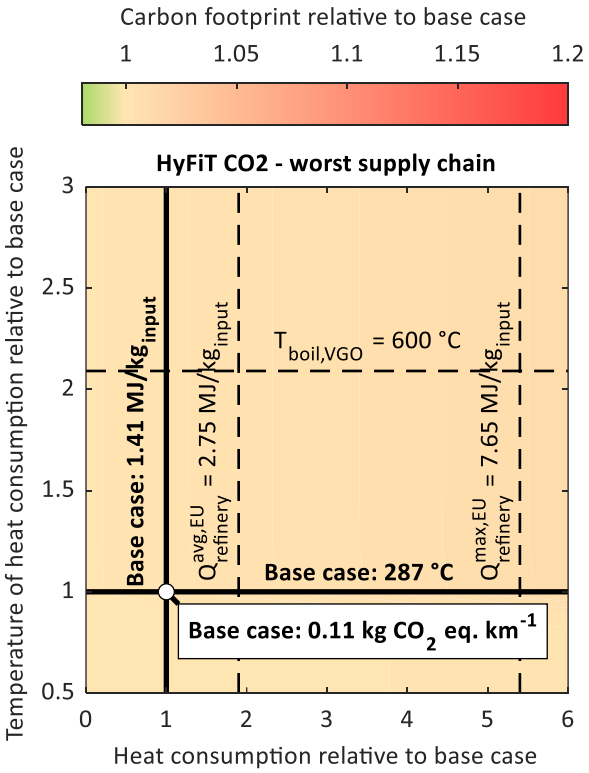
Carbon footprint relative to base case
1
1.05
1.1
1.15
1.2
HyFiT CO2 - worst supply chain
Temperature of heat consumption relative to base case
Heat consumption relative to base case
Base case: 1.41 MJ/kg_input
Q^avg,EU_refinery = 2.75 MJ/kg_input
Q^max,EU_refinery = 7.65 MJ/kg_input
T_boil,VGO = 600 °C
Base case: 287 °C
Base case: 0.11 kg CO2 eq. km-1

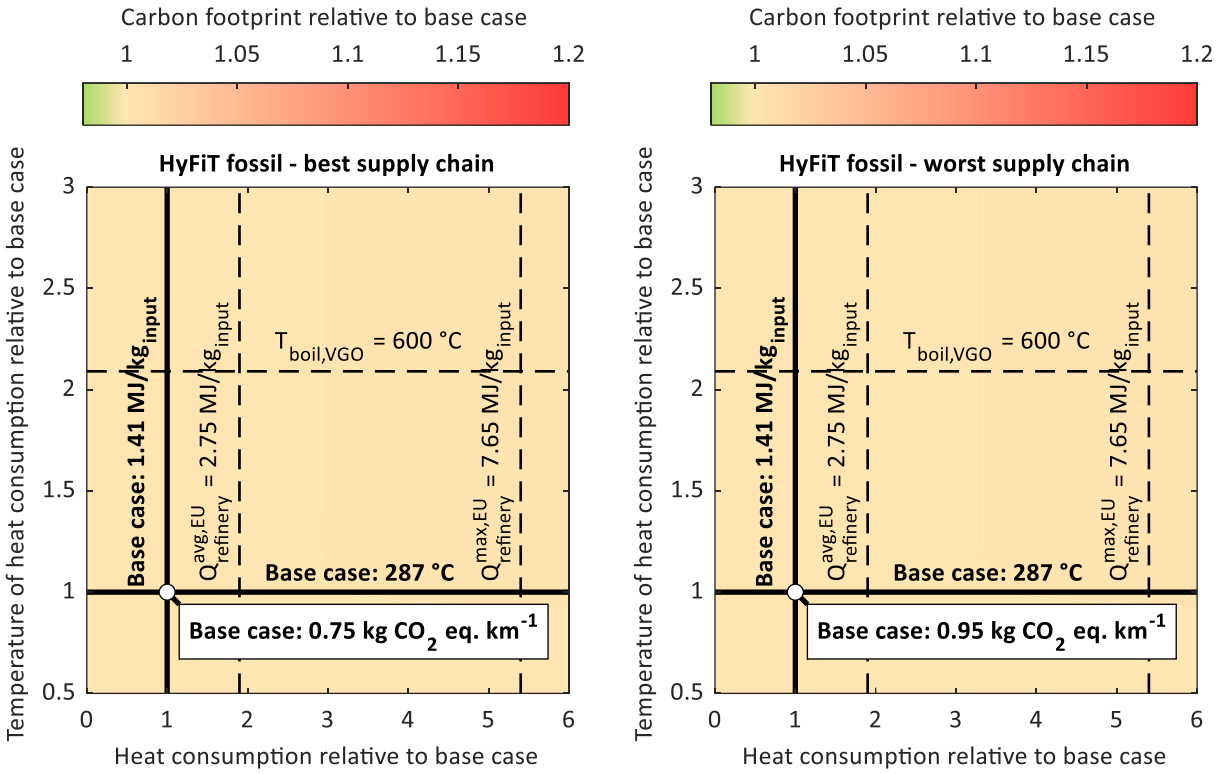

Supplementary Figure 26: Sensitivity analysis of the quantity and temperature level of heat consumption for the removal of aromatics and oxygenates. Results are shown for the supply chain design with electricity from wind power, HyFiT-20%, and the open-gas-loop design (see Figure 7A). For each data point, a supply chain optimization followed by pinch-based heat integration was performed. The used proxy data based on the utility requirements of the "UOP Sulfolane process" are shown as bold horizontal and vertical line (base case). The carbon footprint of this base case is shown in the rectangular box at the intersection of the bold horizontal and vertical line. For reference, we present the average and the maximum heat consumption of EU refineries[169] and the boiling temperature range of vacuum gas oil (VGO)[170] as dashed vertical and horizontal lines, respectively.

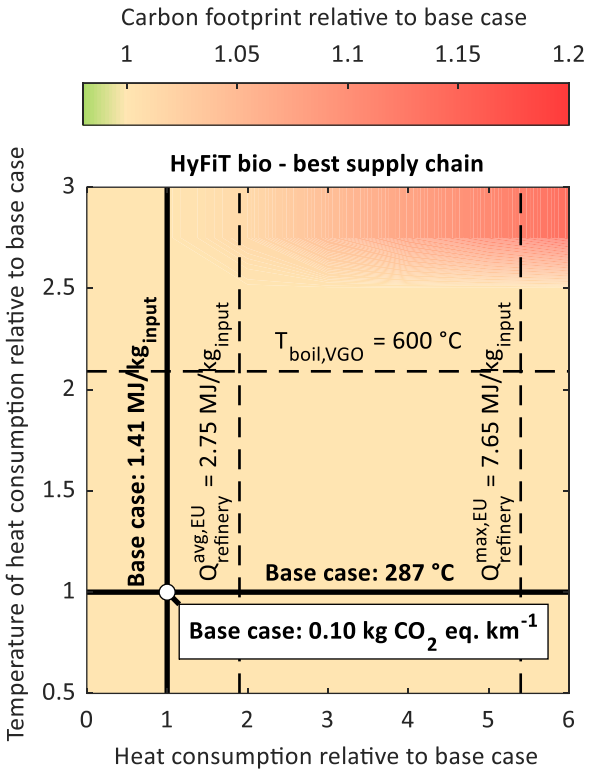
Carbon footprint relative to base case
1
1.05
1.1
1.15
1.2
HyFiT bio - best supply chain
Temperature of heat consumption relative to base case
Heat consumption relative to base case
Base case: 1.41 MJ/kg_input
Q^avg,EU_refinery = 2.75 MJ/kg_input
Q^max,EU_refinery = 7.65 MJ/kg_input
T_boil,VGO = 600 °C
Base case: 287 °C
Base case: 0.10 kg CO2 eq. km-1

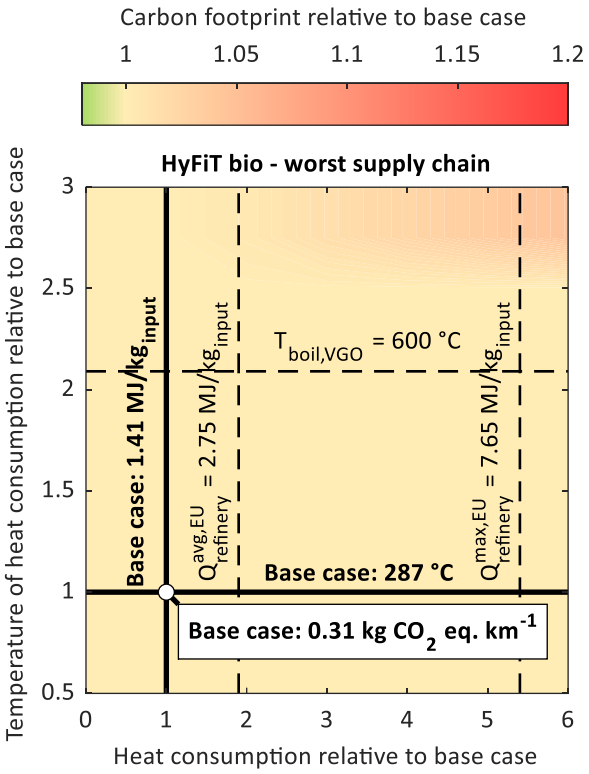
Carbon footprint relative to base case
1
1.05
1.1
1.15
1.2
HyFiT bio - worst supply chain
Temperature of heat consumption relative to base case
Heat consumption relative to base case
Base case: 1.41 MJ/kg_input
Q^avg,EU_refinery = 2.75 MJ/kg_input
Q^max,EU_refinery = 7.65 MJ/kg_input
T_boil,VGO = 600 °C
Base case: 287 °C
Base case: 0.31 kg CO2 eq. km-1

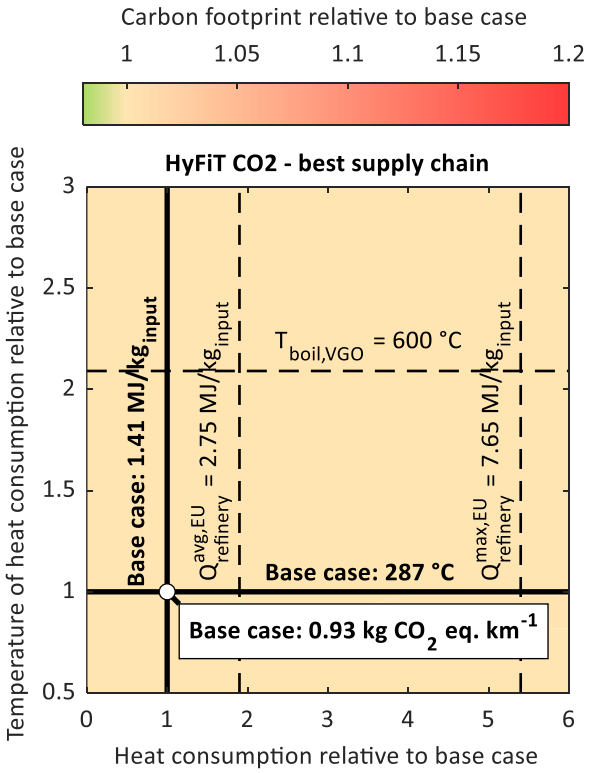
Carbon footprint relative to base case
1
1.05
1.1
1.15
1.2
HyFiT CO2 - best supply chain
Temperature of heat consumption relative to base case
Heat consumption relative to base case
Base case: 1.41 MJ/kg_input
Q^avg,EU_refinery = 2.75 MJ/kg_input
Q^max,EU_refinery = 7.65 MJ/kg_input
T_boil,VGO = 600 °C
Base case: 287 °C
Base case: 0.93 kg CO2 eq. km-1

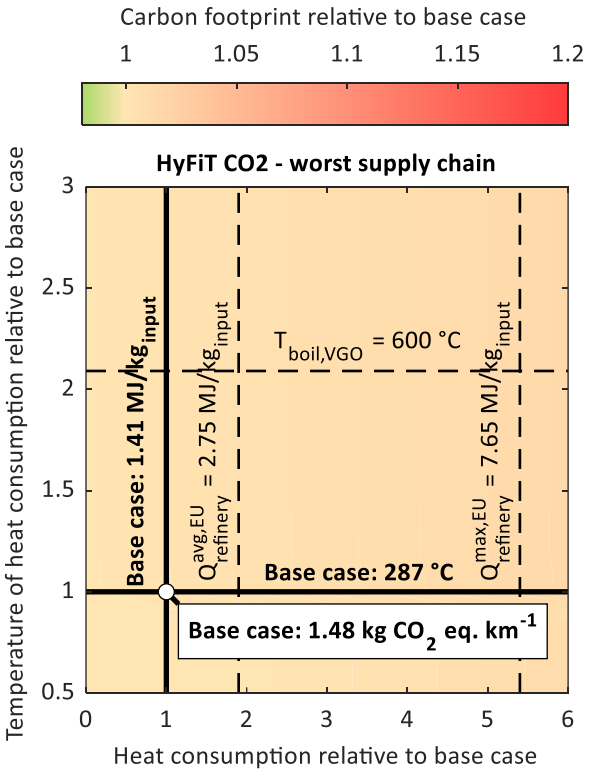
Carbon footprint relative to base case
1
1.05
1.1
1.15
1.2
HyFiT CO2 - worst supply chain
Temperature of heat consumption relative to base case
Heat consumption relative to base case
Base case: 1.41 MJ/kg_input
Q^avg,EU_refinery = 2.75 MJ/kg_input
Q^max,EU_refinery = 7.65 MJ/kg_input
T_boil,VGO = 600 °C
Base case: 287 °C
Base case: 1.48 kg CO2 eq. km-1

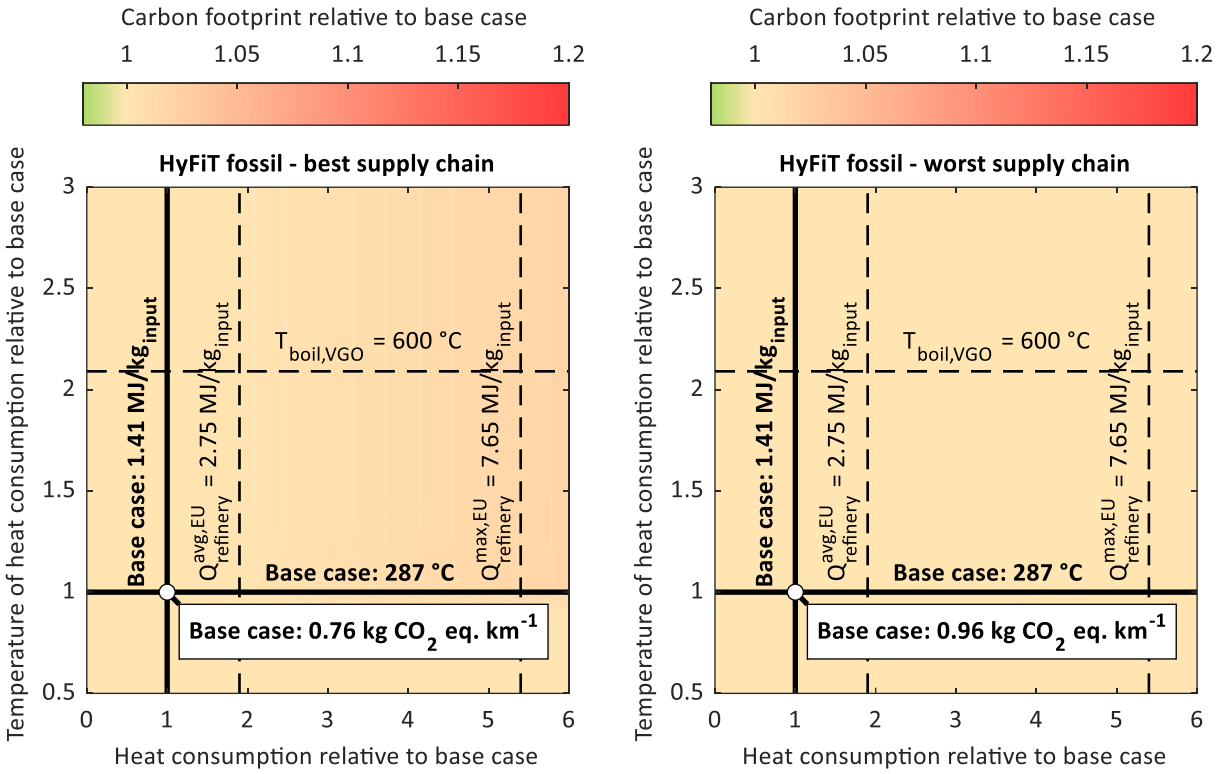

Supplementary Figure 27: Sensitivity analysis of the quantity and temperature level of heat consumption for the removal of aromatics and oxygenates. Results are shown for the supply chain design with electricity from the EU 2030 power grid, HyFiT-20%, and the open-gas-loop design (see Figure 7A). For each data point, a supply chain optimization followed by pinch-based heat integration was performed. The used proxy data based on the utility requirements of the "UOP Sulfolane process" are shown as bold horizontal and vertical line (base case). The carbon footprint of this base case is shown in the rectangular box at the intersection of the bold horizontal and vertical line. For reference, we present the average and the maximum heat consumption of EU refineries[169] and the boiling temperature range of vacuum gas oil (VGO)[170] as dashed vertical and horizontal lines, respectively.

Supplementary Note 25: Key performance indicator: carbon efficiency

Here, we analyze the carbon efficiency as common key performance indicator (Supplementary Figure 28). The carbon efficiency η_{carbon} is calculated as the ratio of carbon in the product $n_{\mathrm{C,product}}$, i.e., the HyFiT-fuel, and carbon in the input $n_{\mathrm{C,input}}$, i.e., the used feedstock:

$$\eta_{\mathrm{carbon}} = \frac{n_{\mathrm{C,product}}}{n_{\mathrm{C,input}}}. \tag{S17}$$

Benchmarking ourselves with recent studies on FT-fuels (Supplementary Figure 28, crosses), we find that carbon efficiency is at least on par or even exceeds previous FT-fuels, in particular for the bio-based route. Due to the unexplored potential for process optimization, we expect that even higher efficiencies can be targeted in proceeding studies.

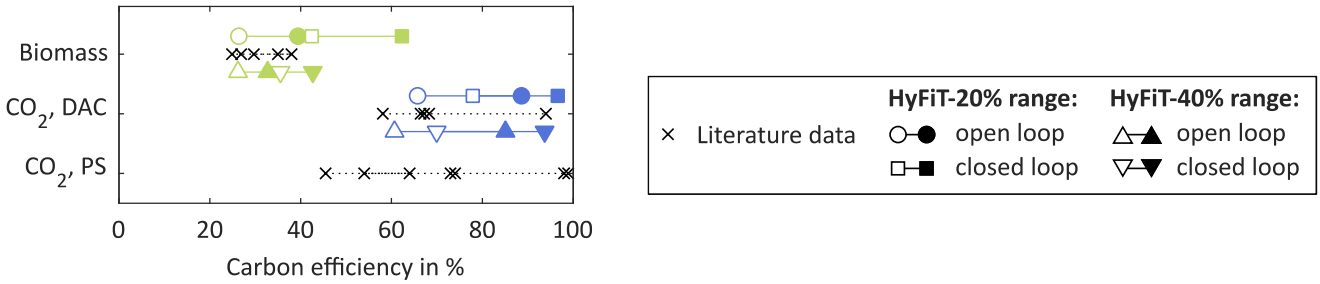

Supplementary Figure 28: Carbon efficiency of HyFiT-fuels based on biomass and CO_2 (via DAC), with alcohol contents of 20 wt% or 40 wt% as well as either open or closed gas loop design. DAC: direct air capture, PS: point source. See Supplementary Table 13 for an overview of the considered literature studies.

Supplementary Table 13: Carbon efficiencies of bio- or CO_2-based FT fuels from literature. Related to Supplementary Figure 28.

Feedstock	Carbon efficiency %	Author
Biomass	30	Zhang et al.[86]
	35	Neuling et al.[83]
	38	Neuling et al.[83]
	25	Albrecht et al.[87]
	27	Dietrich et al.[79]
CO_2, direct air capture	58	Marchese et al.[60]
	68	Marchese et al.[60]
	67	Marchese et al.[60]
	66	Marchese et al.[60]
	94	Vázquez et al.[85]
CO_2, point source	46	Zang et al.[62]
	64	Herz et al.[59]
	54	Herz et al.[59]
	73	König et al.[98]
	74	König et al.[97]
	98	Albrecht et al.[87]
	99	Dietrich et al.[79]

Supplementary Note 26: Key performance indicator: conversion, selectivity, and yield

In this section, we describe the calculation of the CO conversion, selectivity, and yield. The CO conversion (C) is calculated from CO present in the inlet streams ($n_{\mathrm{CO,input}}$) of FT synthesis and hydroformylation as well as CO present in the outlet streams ($n_{\mathrm{CO,output}}$):

$$C = \frac{n_{\mathrm{CO,input}} - n_{\mathrm{CO,output}}}{n_{\mathrm{CO,input}}}. \tag{S18}$$

The carbon-based selectivity (S) is calculated from carbon present in the desired product ($n_{\mathrm{C,product}}$) as well as carbon present in all input ($n_{\mathrm{C,input}}$) and output ($n_{\mathrm{C,output}}$) streams. The selectivity is calculated for the entire HyFiT-fuel and the alcohols and alkanes present in HyFiT-fuels.

$$S = \frac{n_{\mathrm{C,product}}}{n_{\mathrm{C,input}} - n_{\mathrm{C,output}}} \tag{S19}$$

The yield (Y) is calculated by multiplying CO conversion and selectivity:

$$Y = C \cdot S. \tag{S20}$$

Calculated conversions, selectivities, and yields are listed in Supplementary Table 14.

Supplementary Table 14: CO conversion, selectivity, and yield of HyFiT-fuels. Conversion and yield are presented for the open and closed gas loop design. Selectivity and yield are shown for the entire fuel as well as the alcohols and alkanes present in the fuel. LT: low-temperature, HT: high-temperature, FT: Fischer-Tropsch.

HyFiT-fuel	**Conversion** *open / closed*	**Selectivity**			**Yield** *open / closed*		
		Fuel	*Alcohols*	*Alkanes*	*Fuel*	*Alcohols*	*Alkanes*
LT-FT	0.57 / 0.96	0.86	0.12	0.75	0.49 / 0.83	0.07 / 0.12	0.43 / 0.72
HT-FT	0.88 / 0.99	0.36	0.22	0.14	0.32 / 0.36	0.19 / 0.22	0.12 / 0.14
HyFiT-20%	0.61 / 0.97	0.77	0.14	0.63	0.47 / 0.74	0.09 / 0.14	0.38 / 0.61
HyFiT-40%	0.75 / 0.98	0.52	0.19	0.33	0.39 / 0.51	0.14 / 0.19	0.25 / 0.32

Supplementary references

1. European Commission, *Technology readiness level: guidance principles for renewable energy technologies final report*, Publications Office, 2017.
2. J. Breuer, J. Scholten, J. Koj, F. Schorn, M. Fiebrandt, R. Samsun, R. Albus, K. Görner, D. Stolten and R. Peters, *Energies*, 2022, **15** (4), 1443.
3. S. Schemme, J. L. Breuer, M. Köller, S. Meschede, F. Walman, R. C. Samsun, R. Peters and D. Stolten, *International Journal of Hydrogen Energy*, 2019.
4. S. Schemme, J. L. Breuer, R. C. Samsun, R. Peters and D. Stolten, *Journal of CO2 Utilization*, 2018, **27**, 223.
5. K. Roh, A. Bardow, D. Bongartz, J. Burre, W. Chung, S. Deutz, D. Han, M. Heßelmann, Y. Kohlhaas, A. König, J. S. Lee, R. Meys, S. Völker, M. Wessling, J. H. Lee and A. Mitsos, *Green Chem.*, 2020, **22** (12), 3842.
6. F. Mantei, R. E. Ali, C. Baensch, S. Voelker, P. Haltenort, J. Burger, R.-U. Dietrich, N. von der Aßen, A. Schaadt, J. Sauer and O. Salem, *Sustainable Energy Fuels*, 2022, **6** (3), 528.
7. M. Zubel, T. Ottenwälder, B. Heuser, C. Herudek, H. Maas and W. Willems in *Zukünftige Kraftstoffe: Energiewende des Transports Als ein Weltweites Klimaziel*, ed. W. Maus, Springer Berlin/Heidelberg, Berlin/Heidelberg, 2019, p 783.
8. W. Ying, L. Genbao, Z. Wei and Z. Longbao, *Fuel Processing Technology*, 2008, **89** (12), 1272.
9. A. Omari, B. Heuser and S. Pischinger, *Fuel*, 2017, **209**, 232.
10. A. Omari, B. Heuser, S. Pischinger and C. Rüdinger, *Applied Energy*, 2019, **239**, 1242.
11. M. Zubel, T. Ottenwälder, B. Heuser and S. Pischinger, *International Journal of Engine Research*, 2021, **22** (1), 22.
12. D. Bongartz, L. Doré, K. Eichler, T. Grube, B. Heuser, L. E. Hombach, M. Robinius, S. Pischinger, D. Stolten, G. Walther and A. Mitsos, *Applied Energy*, 2018, **231**, 757.
13. S. Michailos, S. McCord, V. Sick, G. Stokes and P. Styring, *Energy Conversion and Management*, 2019, **184**, 262.
14. E. Catizzone, G. Bonura, M. Migliori, F. Frusteri and G. Giordano, *Molecules (Basel, Switzerland)*, 2017, **23** (1).
15. C. Hank, L. Lazar, F. K. Mantei, M. Ouda, R. J. White, T. Smolinka, A. Schaadt, C. Hebling and H.-M. Henning, *Sustainable Energy Fuels*, 2019, **3** (11), 3219.
16. D. F. Rodríguez Vallejo and A. d. Klerk, *Energy Fuels*, 2013, **27** (6), 3137.
17. S. Völker, S. Deutz, J. Burre, D. Bongartz, A. Omari, B. Lehrheuer, A. Mitsos, S. Pischinger, A. Bardow and N. von der Assen, *Sustainable Energy Fuels*, 2022, **6** (8), 1959.
18. S. Deutz, D. Bongartz, B. Heuser, A. Kätelhön, L. Schulze Langenhorst, A. Omari, M. Walters, J. Klankermayer, W. Leitner, A. Mitsos, S. Pischinger and A. Bardow, *Energy Environ. Sci.*, 2018, **11** (2), 331.
19. F. Trippe, M. Fröhling, F. Schultmann, R. Stahl, E. Henrich and A. Dalai, *Fuel Processing Technology*, 2013, **106**, 577.
20. L. R. Clausen, B. Elmegaard and N. Houbak, *Energy*, 2010, **35** (12), 4831.
21. F. Ju, H. Chen, X. Ding, H. Yang, X. Wang, S. Zhang and Z. Dai, *Biotechnology advances*, 2009, **27** (5), 599.
22. P. Bokinge, S. Heyne and S. Harvey, *Energy Sci Eng*, 2020, **8** (7), 2587.

23. N. Mahbub, A. O. Oyedun, A. Kumar, D. Oestreich, U. Arnold and J. Sauer, *Journal of Cleaner Production*, 2017, **165**, 1249.

24. C. Arcoumanis, C. Bae, R. Crookes and E. Kinoshita, *Fuel*, 2008, **87** (7), 1014.

25. D. Pélerin, K. Gaukel, M. Härtl, E. Jacob and G. Wachtmeister, *Fuel*, 2020, **259**, 116231.

26. S. H. Park and C. S. Lee, *Energy Conversion and Management*, 2014, **86**, 848.

27. J. Schröder and K. Görsch, *Energy Fuels*, 2020, **34** (1), 450.

28. F. Müller-Langer, S. Majer and S. O'Keeffe, *Energ Sustain Soc*, 2014, **4** (1).

29. S. Puricelli, G. Cardellini, S. Casadei, D. Faedo, A.E.M. van den Oever and M. Grosso, *Renewable and Sustainable Energy Reviews*, 2021, **137**, 110398.

30. B. Paris, G. Papadakis, R. Janssen and D. Rutz, *Renewable and Sustainable Energy Reviews*, 2021, **144**, 111038.

31. T. Hartikka, M. Kuronen and U. Kiiski in *SAE Technical Paper Series*, SAE International400 Commonwealth Drive, Warrendale, PA, United States, 2012.

32. M. A. Fazal, A.S.M.A. Haseeb and H. H. Masjuki, *Renewable and Sustainable Energy Reviews*, 2011, **15** (2), 1314.

33. P. D. Patel, A. Lakdawala, S. Chourasia and R. N. Patel, *Renewable and Sustainable Energy Reviews*, 2016, **65** (4), 24.

34. M. Lapuerta, M. Villajos, J. R. Agudelo and A. L. Boehman, *Fuel Processing Technology*, 2011, **92** (12), 2406.

35. M. Kuronen, S. Mikkonen, P. Aakko and T. Murtonen in *SAE Technical Paper Series*, SAE International400 Commonwealth Drive, Warrendale, PA, United States, 2007.

36. H. Aatola, M. Larmi, T. Sarjovaara and S. Mikkonen, *SAE Int. J. Engines*, 2009, **1** (1), 1251.

37. S. K. Hoekman and C. Robbins, *Fuel Processing Technology*, 2012, **96** (1), 237.

38. T. Murtonen, P. Aakko-Saksa, M. Kuronen, S. Mikkonen and K. Lehtoranta, *SAE Int. J. Fuels Lubr.*, 2009, **2** (2), 147.

39. V. T. Wyatt, M. A. Hess, R. O. Dunn, T. A. Foglia, M. J. Haas and W. N. Marmer, *J Amer Oil Chem Soc*, 2005, **82** (8), 585.

40. M. Johansson, J. Yang, R. Ochoterena, S. Gjirja and I. Denbratt, *Fuel*, 2013, **106**, 293.

41. Y.-p. G. Wu, Y.-f. Lin and C.-T. Chang, *Fuel*, 2007, **86** (17-18), 2810.

42. G. Karavalakis, Y. Jiang, J. Yang, T. Durbin, J. Nuottimäki and K. Lehto, *SAE Int. J. Fuels Lubr.*, 2016, **9** (1), 177.

43. R. Arvidsson, S. Persson, M. Fröling and M. Svanström, *Journal of Cleaner Production*, 2011, **19** (2-3), 129.

44. A. Mohr and S. Raman, *Energy Policy*, 2013, **63** (100), 114.

45. J. Fargione, J. Hill, D. Tilman, S. Polasky and P. Hawthorne, *Science (New York, N.Y.)*, 2008, **319** (5867), 1235.

46. A. van Grinsven, E. van den Toorn, R. van der Veen, B. Kampman and C. Oil, *CE Delft: Delft, The Netherlands*, 2020, 1.

47. L. Colelli, V. Segneri, C. Bassano and G. Vilardi, *Energy Conversion and Management*, 2023, **288**, 117165.

48. H. E. Delgado, V. Cappello, G. Zang, P. Sun, C. Ng, P. Vyawahare, A. A. Elgowainy, D. S. Wendt, R. D. Boardman and J. Marcinkoski, *Journal of CO2 Utilization*, 2023, **72**, 102481.

49. G. H. Hong, J. Lee, Y. Cho and S. Hwang, *Korean J. Chem. Eng.*, 2023, **40** (4), 740.

50. E. Jacobsen, S. M. Skov, A. Singlitico and H. L. Frandsen, *International Journal of Hydrogen Energy*, 2023, **139**, 1173.

51. M. Katiyo, L. Gudukeya, M. Kanganga and N. Sukdeo in *Manufacturing Driving Circular Economy*, ed. H. Kohl, G. Seliger and F. Dietrich, Springer International Publishing, Cham, 2023, p 729.

52. J. A. Okolie, D. Awotoye, M. E. Tabat, P. U. Okoye, E. I. Epelle, C. C. Ogbaga, F. Güleç and B. Oboirien, *iScience*, 2023, **26** (6), 106944.

53. A.E.M. van den Oever, D. Costa and M. Messagie, *Applied Energy*, 2023, **336**, 120834.

54. J. Weyand, F. Habermeyer and R.-U. Dietrich, *Fuel*, 2023, **342** (4), 127763.

55. R. Gao, L. Wang, L. Zhang, C. Zhang, K.-W. Jun, S. Ki Kim, H.-G. Park, T. Zhao, Y. Gao, Y. Zhu, H. Wan and G. Guan, *Fuel*, 2022, **325** (12), 124855.

56. J. D. Medrano-García, M. A. Charalambous and G. Guillén-Gosálbez, *ACS Sustainable Chem. Eng.*, 2022, 987.

57. R. Peters, N. Wegener, R. C. Samsun, F. Schorn, J. Riese, M. Grünewald and D. Stolten, *Processes*, 2022, **10** (4), 699.

58. R. Gao, C. Zhang, K.-W. Jun, S. K. Kim, H.-G. Park, T. Zhao, L. Wang, H. Wan and G. Guan, *Journal of CO2 Utilization*, 2021, **51** (5), 101619.

59. G. Herz, C. Rix, E. Jacobasch, N. Müller, E. Reichelt, M. Jahn and A. Michaelis, *Applied Energy*, 2021, **292**, 116655.

60. M. Marchese, G. Buffo, M. Santarelli and A. Lanzini, *Journal of CO2 Utilization*, 2021, **46**, 101487.

61. D. Freire Ordóñez, N. Shah and G. Guillén-Gosálbez, *Applied Energy*, 2021, **286**, 116488.

62. G. Zang, P. Sun, A. Elgowainy, A. Bafana and M. Wang, *Environ. Sci. Technol.*, 2021, **55** (6), 3888.

63. G. Zang, P. Sun, A. A. Elgowainy, A. Bafana and M. Wang, *Journal of CO2 Utilization*, 2021, **46**, 101459.

64. G. Zang, P. Sun, E. Yoo, A. Elgowainy, A. Bafana, U. Lee, M. Wang and S. Supekar, *Environmental science & technology*, 2021, **55** (11), 7595.

65. V. B. Borugadda, G. Kamath and A. K. Dalai, *Energy*, 2020, **195**, 116985.

66. V. Dieterich, A. Buttler, A. Hanel, H. Spliethoff and S. Fendt, *Energy Environ. Sci.*, 2020.

67. S. Drünert, U. Neuling, T. Zitscher and M. Kaltschmitt, *Applied Energy*, 2020, **277**, 115578.

68. C. M. Liu, N. K. Sandhu, S. T. McCoy and J. A. Bergerson, *Sustainable Energy Fuels*, 2020, **4** (6), 3129.

69. S. Lundberg, A. Fagerström and K. Johansson, *Life Cycle Assessment of Gasification-based Fischer-Tropsch Bio Jet Fuel production: Retrieved from IVL Svenska Miljöinstitutet website*, http://urn.kb.se/resolve?urn=urn:nbn:se:ivl:diva-2792, IVL Svenska Miljöinstitutet, 2020.

70. I. J. Okeke, K. Sahoo, N. Kaliyan and S. Mani, *Journal of Cleaner Production*, 2020, **249**, 119358.

71. M. Alhyari, A. Al-Salaymeh, M. Irshidat, M. Kaltschmitt and U. Neuling, *J. Ecol. Eng.*, 2019, **20** (4), 239.

72. R. Cuéllar-Franca, P. García-Gutiérrez, I. Dimitriou, R. H. Elder, R. W.K. Allen and A. Azapagic, *Applied Energy*, 2019, **253**, 113560.

73. M. Decker, F. Schorn, R. C. Samsun, R. Peters and D. Stolten, *Applied Energy*, 2019, **250**, 1099.

74. L. E. Hombach, L. Doré, K. Heidgen, H. Maas, T. J. Wallington and G. Walther, *Journal of Cleaner Production*, 2019, **207**, 153.

75. Z. Navas-Anguita, P. L. Cruz, M. Martín-Gamboa, D. Iribarren and J. Dufour, *Fuel*, 2019, **235**, 1492.

76. N. I. Tsongidis, A. G. Asimakopoulou, G. Pantoleontos and A. G. Konstandopoulos, *Journal of CO2 Utilization*, 2019, **30**, 142.

77. H. Blanco, W. Nijs, J. Ruf and A. Faaij, *Applied Energy*, 2018, **232**, 617.

78. S. Brynolf, M. Taljegard, M. Grahn and J. Hansson, *Renewable and Sustainable Energy Reviews*, 2018, **81**, 1887.

79. R.-U. Dietrich, F. G. Albrecht, S. Maier, D. H. König, S. Estelmann, S. Adelung, Z. Bealu and A. Seitz, *Biomass and Bioenergy*, 2018, **111**, 165.

80. I. Dimitriou, H. Goldingay and A. V. Bridgwater, *Renewable and Sustainable Energy Reviews*, 2018, **88**, 160.

81. B. Hernandez and M. Martin, *Energy Conversion and Management*, 2018, **174**, 998.

82. G. Herz, E. Reichelt and M. Jahn, *Applied Energy*, 2018, **215**, 309.

83. U. Neuling and M. Kaltschmitt, *Fuel Processing Technology*, 2018, **171**, 54.

84. M. Samavati, A. Martin, M. Santarelli and V. Nemanova, *Energies*, 2018, **11** (5), 1223.

85. F. V. Vázquez, J. Koponen, V. Ruuskanen, C. Bajamundi, A. Kosonen, P. Simell, J. Ahola, C. Frilund, J. Elfving, M. Reinikainen, N. Heikkinen, J. Kauppinen and P. Piermartini, *Journal of CO2 Utilization*, 2018, **28**, 235.

86. Y. Zhang, A. H. Sahir, E. C. D. Tan, M. S. Talmadge, R. Davis, M. J. Biddy and L. Tao, *Green Chem.*, 2018, **20** (23), 5358.

87. F. G. Albrecht, D. H. König, N. Baucks and R.-U. Dietrich, *Fuel*, 2017, **194**, 511.

88. S. de Jong, K. Antonissen, R. Hoefnagels, L. Lonza, M. Wang, A. Faaij and M. Junginger, *Biotechnology for biofuels*, 2017, **10**, 64.

89. G. Herz, E. Reichelt and M. Jahn, *Energy*, 2017, **132**, 370.

90. W. Liu, J. Wang, D. Bhattacharyya, Y. Jiang and D. DeVallance, *Energy*, 2017, **141**, 76.

91. I. J. Okeke and S. Mani, *Biofuels, Bioprod. Bioref.*, 2017, **11** (3), 472.

92. M. Rafati, L. Wang, D. C. Dayton, K. Schimmel, V. Kabadi and A. Shahbazi, *Energy Conversion and Management*, 2017, **133**, 153.

93. A. S. Snehesh, H. S. Mukunda, S. Mahapatra and S. Dasappa, *Energy*, 2017, **130**, 182.

94. G. A. Tsalidis, F. E. Discha, G. Korevaar, W. Haije, W. de Jong and J. Kiel, *Int J Energy Environ Eng*, 2017, **8** (3), 175.

95. H. Zhou, Y. Qian, A. Kraslawski, Q. Yang and S. Yang, *Energy*, 2017, **139**, 507.

96. A. Zimmerman, J. Wunderlich, G. Buchner, L. Müller, K. Armstrong, S. Michailos, A. Marxen, H. Naims, F. Mason, G. Stokes and E. Williams, *Techno-Economic Assessment & Life Cycle Assessment Guidelines for CO2 Utilization*, 2018.

97. D. H. König, N. Baucks, R.-U. Dietrich and A. Wörner, *Energy*, 2015, **91**, 833.

98. D. H. König, M. Freiberg, R.-U. Dietrich and A. Wörner, *Fuel*, 2015, **159**, 289.

99. A. d. Klerk, *Fischer-Tropsch refining*, Wiley-VCH, Weinheim, 2011.

100. J. van de Loosdrecht, F. G. Botes, I. M. Ciobica, A. Ferreira, P. Gibson, D. J. Moodley, A. M. Saib, J. L. Visagie, C. J. Weststrate and J. W. Niemantsverdriet in *Comprehensive inorganic chemistry II: From elements to applications*, ed. J. Reedijk, Elsevier, Amsterdam, 2013, p 525.

101. A. d. Klerk in *Encyclopedia of chemical technology*, ed. R. E. Kirk and D. F. Othmer, Wiley, New York, NY, 2003.

102. J.-l. Tu, M.-y. Ding, Q. Zhang, Y.-l. Zhang, C.-g. Wang, T.-j. Wang, L.-l. Ma and X.-j. Li, *ChemCatChem*, 2015, **7** (15), 2323.

103. N. Tsubaki, S. Sun and K. Fujimoto, *Journal of Catalysis*, 2001, **199** (2), 236.

104. P. M. Maitlis and A. d. Klerk, eds., *Greener Fischer-Tropsch processes for fuels and feedstocks*, Wiley-VCH, Weinheim, 2013.

105. A. d. Klerk and E. Furimsky, *Catalysis in the Refining of Fischer-Tropsch Syncrude*, Royal Society of Chemistry, Cambridge, 2010.

106. M. E. Dry and A. P. Steynberg in *Fischer-Tropsch technology*, ed. A. Steynberg and M. Dry, Elsevier, Amsterdam, 2006, p 406.

107. R. K. Bartoo, *Chemical Engineering Progress*, 1984, 35.

108. A. L. Kohl and R. B. Nielsen in *Gas purification*, ed. A. L. Kohl and R. Nielsen, Gulf Publishing Company An Imprint of Elsevier, Houston, Texas, 1997, p 330.

109. R. A. Meyers, ed., *Handbook of petroleum refining processes*, McGraw-Hill, New York, 2004.

110. Ullmann, ed., *Ullmann's Encyclopedia of Industrial Chemistry*, Wiley-VCH Verlag GmbH & Co. KGaA, Weinheim, Germany, 2000.

111. S. Püschel, S. Störtte, J. Topphoff, A. J. Vorholt and W. Leitner, *ChemSusChem*, 2021, **14**, 5226.

112. B. Cornils, A. Börner, R. Franke, B. Zhang, E. Wiebus and K. Schmid in *Applied homogeneous catalysis with organometallic compounds: A comprehensive handbook in four volumes*, ed. B. Cornils, W. A. Herrmann, M. Beller and R. Paciello, Wiley-VCH Verlag GmbH & Co. KGaA, Weinheim, 2018, p 23.

113. M. S. Shaharun, B. K. Dutta, H. Mukhtar and S. Maitra, *Chemical Engineering Science*, 2010, **65** (1), 273.

114. B. Cornils, W. A. Herrmann, H.-W. Zanthoff and C.-H. Wong, *Catalysis from A to Z*, Wiley-VCH Verlag GmbH & Co. KGaA, Weinheim, Germany, 2013.

115. A. Börner and R. Franke, *Hydroformylation*, Wiley-VCH Verlag GmbH & Co. KGaA, Weinheim, Germany, 2016.

116. H. Warmeling, D. Hafki, T. von Söhnen and A. J. Vorholt, *Chemical Engineering Journal*, 2017, **326**, 298.

117. H. Warmeling, D. Janz, M. Peters and A. J. Vorholt, *Chemical Engineering Journal*, 2017, **330**, 585.

118. E. A. Redina, K. V. Vikanova, G. I. Kapustin, I. V. Mishin, O. P. Tkachenko and L. M. Kustov, *Eur. J. Org. Chem.*, 2019, **2019** (26), 4159.

119. Hydrocarbon Processing, *2008 Refining Processes Handbook*, 2008.

120. M. Rudin, *Isocracking technology review*, 2018.

121. M. Bachmann, S. Völker, J. Kleinekorte and A. Bardow, *ACS Sustainable Chem. Eng.*, 2023, **11** (14), 5356–5366.

122. A. K. Prabhu and S.T. Oyama, *Journal of Membrane Science*, 2000, **176** (2), 233.

123. L. Dubois and D. Thomas, *International Journal of Greenhouse Gas Control*, 2018, **69**, 20.

124. NIST Chemistry WebBook, *NIST Standard Reference Database*, 2023.

125. International Organization for Standardization, *DIN 51562-1: Viscometry - Measurement of kinematic viscosity by means of the Ubbelohde viscometer - Part 1: Viscometer specification and measurement procedure*, 1999.

126. International Organization for Standardization, *DIN EN ISO 12156-1: Diesel fuel – Assessment of lubricity using the high-frequency reciprocating rig (HFRR) - Part 1: Test method*, 2019.

127. International Organization for Standardization, *DIN ISO 1817: Rubber, vulcanized or thermoplastic - Determination of the effect of liquids*, 2015.

128. International Organization for Standardization, *DIN ISO 13226: Rubber - Standard reference elastomers (SREs) for characterizing the effect of liquids on vulcanized rubbers*, 2021.

129. International Organization for Standardization, *DIN ISO 23529: Rubber – General procedures for preparing and conditioning test pieces for physical test methods*, 2020.

130. Sartorius Research, *R 160 P. Electronic Semi-Microbalance: Installation and Operating Instructions*.

131. Lauda scientific, *Tensiometer TD4: Automatische Messung der Oberflächen- und Grenzflächenspannung*.

132. Haake Circulators, *Instruction Manual: F3* • F3/H41 • F3-S • F3-M • F3-C • F3-CH • F3-K • F3-Q*.

133. Bareiss Prüfgerätebau GmbH, *Betriebsanleitung: digi test*, 2007.

134. International Organization for Standardization, *DIN ISO 48-2: Rubber, vulcanized or thermoplastic – Determination of hardness – Part 2: Hardness between 10 IRHD and 100 IRHD*, 2021.

135. B. Richter, *International Polymer Science and Technology*, 2014, **41** (5), 1.

136. B. Richter, Bewertung von Beständigkeitstests von Elastomeren Werkstoffen mit Getriebe- und Motorölen bezüglich des Funktionsverhalten von Radialwellendichtringen. O-Ring Prüflabor Richter, http://www.o-ring-prueflabor.de/files/bewertung-von-bestaendigkeitstest.pdf (last accessed October 2022).

137. J. Schaub, M. Pieper, S. Klopstein, M. Übbing, P. Knappe, P. Muthyala and T. Schmidt in *Internationaler Motorenkongress 2020*, ed. J. Liebl, C. Beidl and W. Maus, Springer Fachmedien Wiesbaden, Wiesbaden, 2020, p 335.

138. D. Neumann, S. Pischinger, M. Zubel, B. Heuser, K. Thenert, W. Leitner, M. Schönen, J. Schaub and C. Jörg in *39. Internationales Wiener Motorensymposium 26.-27. April 2018*, ed. B. Geringer and H.-P. Lenz, VDI Verlag, 2018, p 230.

139. A. Omari, S. Pischinger, O. P. Bhardwaj, B. Holderbaum, J. Nuottimäki and M. Honkanen, *SAE Int. J. Fuels Lubr.*, 2017, **10** (3).

140. European Commission, *Supporting information to the characterisation factors of recommended EF Life Cycle Impact Assessment methods: Version 2, from ILCD to EF 3.0*, 2018.

141. G. Wernet, C. Bauer, B. Steubing, J. Reinhard, E. Moreno-Ruiz and B. Weidema, *Int J Life Cycle Assess*, 2016, **21** (9), 1218.

142. S. Deutz and A. Bardow, *Nat Energy*, 2021, **6**, 203.

143. L. J. Müller, A. Kätelhön, S. Bringezu, S. McCoy, S. Suh, R. Edwards, V. Sick, S. Kaiser, R. Cuéllar-Franca, A. El Khamlichi, J. H. Lee, N. von der Assen and A. Bardow, *Energy & Environmental Science*, 2020, **13** (9), 2979.

144. S. M. Jarvis and S. Samsatli, *Renewable and Sustainable Energy Reviews*, 2018, **85**, 46.

145. K. Bareiß, C. de La Rua, M. Möckl and T. Hamacher, *Applied Energy*, 2019, **237**, 862.

146. D. R. Ladner in *Cryocoolers 16: International Cryocooler Conference 16, Atlanta, GA, ICC 16 ; proceedings of the 16th ICC, Atlanta, GA, May 17 - 20, 2010*, ed. S. D. Miller, ICC Press, Boulder, Colo., 2011.

147. L. J. Müller, A. Kätelhön, M. Bachmann, A. Zimmermann, A. Sternberg and A. Bardow, *Front. Energy Res.*, 2020, **8**, 1.

148. A. David, B. V. Mathiesen, H. Averfalk, S. Werner and H. Lund, *Energies*, 2017, **10** (4), 578.

149. Y. Qiu, P. Lamers, V. Daioglou, N. McQueen, H.-S. de Boer, M. Harmsen, J. Wilcox, A. Bardow and S. Suh, *Nature communications*, 2022, **13** (1), 3635.

150. C. Reinert, S. Deutz, H. Minten, L. Dörpinghaus, S. von Pfingsten, N. Baumgärtner and A. Bardow in *30th European Symposium on Computer Aided Process Engineering*, ed. S. Pierucci, F. Manenti, G. L. Bozzano and D. Manca, Elsevier, Amsterdam, 2020, p 241.

151. IEA, *Energy Technology Perspectives 2017: Catalysing Energy Technology Transformations*, International Energy Agency, Paris, 2017.

152. R. Sacchi, C. Bauer, B. Cox and C. Mutel, *Renewable and Sustainable Energy Reviews*, 2022, **162**, 112475.

153. A. Sternberg and A. Bardow, *ACS Sustainable Chem. Eng.*, 2016, **4** (8), 4156.

154. IHS Markit, ed., *Process Economics Program (PEP) Yearbook*, 2018.

155. Agora Verkehrswende, *Agora Energiewende and Frontier Economics: The Future Cost of Electricity-Based Synthetic Fuels*, 2018.

156. M. Bachmann, A. Kätelhön, B. Winter, R. Meys, L. J. Müller and A. Bardow, *Faraday discussions*, 2021, **230**, 227.

157. L. Wang, J. Littlewood and R. J. Murphy, *Renewable and Sustainable Energy Reviews*, 2013, **28**, 715.

158. B. Daylan and N. Ciliz, *Renewable Energy*, 2016, **89**, 578.

159. S. González-García, M. T. Moreira and G. Feijoo, *Renewable and Sustainable Energy Reviews*, 2010, **14** (7), 2077.

160. S. González-García, D. Iribarren, A. Susmozas, J. Dufour and R. J. Murphy, *Applied Energy*, 2012, **95**, 111.

161. A. L. Borrion, M. C. McManus and G. P. Hammond, *Biomass and Bioenergy*, 2012, **47**, 9.

162. S. Papong and P. Malakul, *Bioresource technology*, 2010, **101 Suppl 1**, S112-8.

163. R. E. H. Sims, W. Mabee, J. N. Saddler and M. Taylor, *Bioresource technology*, 2010, **101** (6), 1570.

164. P. Sassner, M. Galbe and G. Zacchi, *Biomass and Bioenergy*, 2008, **32** (5), 422.

165. C. Piccolo and F. Bezzo, *Biomass and Bioenergy*, 2009, **33** (3), 478.

166. A. R. G. da Silva, C. E. Torres Ortega and B.-G. Rong, *Bioresource technology*, 2016, **218** (2), 561.

167. E. Gnansounou and A. Dauriat, *Bioresource technology*, 2010, **101** (13), 4980.

168. H. Kwon, X. Liu, J. B. Dunn, S. Mueller, M. M. Wander and M. Wang, Carbon Calculator for Land Use and Land Management Change from Biofuels Production (CCLUB), Users' Manual and Technical Documentation (No. ANL/ESD/12-5 Rev. 7). Argonne National Laboratory (ANL), https://greet.es.anl.gov/publications.

169. European Commission, *Best Available Techniques (BAT) Reference Document for the Refining of Mineral Oil and Gas: Industrial Emissions Directive 2010/75/EU (Integrated Pollution Prevention and Control)*, Publications Office, Luxembourg, 2015.

170. M. R. Riazi, S. Eser, S. S. Agrawal and J. L. Peña Díez, *Petroleum refining and natural gas processing*, ASTM International, West Conshohocken, PA, 2013.